
Electronic Thesis and Dissertation Repository

3-1-2023 1:30 PM

Development of Pulsed Laser Deposited TiO₂, ZnO and AZO Thin UV-Protection Films for Enhanced Perovskite Photostability

Kate Lochhead, *The University of Western Ontario*

Supervisor: Johlin, Eric, *The University of Western Ontario*

A thesis submitted in partial fulfillment of the requirements for the Master of Engineering Science degree in Mechanical and Materials Engineering

© Kate Lochhead 2023

Follow this and additional works at: <https://ir.lib.uwo.ca/etd>



Part of the [Semiconductor and Optical Materials Commons](#)

Recommended Citation

Lochhead, Kate, "Development of Pulsed Laser Deposited TiO₂, ZnO and AZO Thin UV-Protection Films for Enhanced Perovskite Photostability" (2023). *Electronic Thesis and Dissertation Repository*. 9150. <https://ir.lib.uwo.ca/etd/9150>

This Dissertation/Thesis is brought to you for free and open access by Scholarship@Western. It has been accepted for inclusion in Electronic Thesis and Dissertation Repository by an authorized administrator of Scholarship@Western. For more information, please contact wlsadmin@uwo.ca.

Abstract

Perovskite solar cells are an emerging sustainable energy conversion technology with the potential to provide relief from the global energy crisis. However, the UV-induced degradation of perovskites has been a barrier to commercialization. Thin film encapsulation represents a promising solution for extending device lifetimes. Three materials with suitable bandgaps for blocking UV light are identified: TiO₂, ZnO and AZO. Herein, the optical properties of TiO₂, ZnO and AZO thin films grown by room-temperature pulsed laser deposition are optimized by varying the oxygen partial pressure during deposition. UV-Vis spectroscopy reveals facile bandgap tuning via the concentration of O₂ vacancies. Accelerated UV-aging experiments find that the films which screen the most UV light are also most effective in delaying perovskite degradation. A comparison of TiO₂, ZnO and AZO photoprotective coatings concludes that ZnO is most suitable for perovskite solar cell encapsulation since it provides a ~50% reduction in UV-degradation without significantly compromising visible light transmittance.

Keywords

Perovskite solar cells; Degradation; UV light stability; Thin film encapsulation; Pulsed laser deposition; TiO₂; ZnO; AZO; Oxygen vacancies

Summary for Lay Audience

In the face of increasing energy demands and growing concerns over global warming, there is a heightened need for a sustainable source of energy. Among renewable energy sources, solar is one of the most promising due to its inherent abundance. Currently, crystalline silicon solar cells dominate the photovoltaics market. Alternatively, solar cells can be made with low-cost materials called perovskites, which contribute to fewer greenhouse gas emissions due to less energy-intensive manufacturing. Given their competitive power conversion efficiencies and the promise of low-cost manufacturing, perovskite solar cells (PSCs) have the potential to disrupt the incumbent silicon technology. However, issues associated with the stability of perovskites in water, oxygen and UV light persist, preventing widespread adoption. As a result, the success of PSCs relies now on the improvement of their long-term stabilities. Significant efforts to-date have been placed on preventing water- and oxygen-induced perovskite degradation, however, this thesis focuses on the less studied issue of UV light-induced degradation. It looks to extend the lifetime of PSCs by encapsulating devices with transparent thin films of titanium dioxide (TiO_2), zinc oxide (ZnO) and aluminum-doped zinc oxide (AZO), optimized to block UV-light. The suitability of each material for the encapsulation application is assessed by subjecting TiO_2 -, ZnO -, and AZO-protected perovskites to harsh UV radiation and monitoring the degree to which each sample is degraded. While all thin films delayed the onset of UV-induced degradation, ZnO provided the most substantial protection and is therefore considered most promising for extending PSC lifetimes. Overall, this work will help to advance the commercialization of perovskite solar technologies, providing a more reliable source of renewable energy, and relief from the global energy crisis.

Co-Authorship Statement

- Chapter 1: Kate Lochhead – Wrote manuscript
Eric Johlin – Revised manuscript
- Chapter 2: Kate Lochhead – Wrote manuscript
Eric Johlin – Revised Manuscript
Dongfang Yang – Revised Manuscript
- Chapter 3: Kate Lochhead – Wrote manuscript
Eric Johlin – Revised manuscript
Vahid Dehnavi – Performed XRD, FESEM
Jeffrey Henderson – Performed XPS
- Chapter 4: Kate Lochhead – Wrote manuscript
Eric Johlin – Revised manuscript
- Chapter 5: Kate Lochhead – Wrote manuscript
Eric Johlin – Revised manuscript
- Chapter 6: Kate Lochhead – Wrote manuscript
Eric Johlin – Revised Manuscript
Vahid Dehnavi – Performed XRD, FESEM
- Chapter 7: Kate Lochhead – Wrote manuscript
Eric Johlin – Revised manuscript

All equipment used in the presented work resides at the National Research Council of Canada's London site, with the exception of the XPS, XRD and FESEM systems, which reside at Surface Science Western.

Acknowledgments

I would like to thank my supervisor, Dr. Eric Johlin, for his support throughout my M.E.Sc degree and assistance in revising my thesis. I would also like to thank Dr. Dongfang Yang for his guidance and willingness to share his knowledge with me. I would like to acknowledge Dr. Vahid Dehnavi and Dr. Jeffrey Henderson from Surface Science Western, who were tremendously helpful in acquiring XRD, FESEM and XPS data. Finally, I owe a very special thank you to my soon-to-be husband, Tyrus, for the unending encouragement, kindness and love that he so generously gives.

Table of Contents

Abstract.....	ii
Summary for Lay Audience.....	iii
Co-Authorship Statement.....	iv
Acknowledgments.....	v
Table of Contents.....	vi
List of Tables.....	ix
List of Figures.....	x
List of Appendices.....	xiv
List of Abbreviations, Symbols and Nomenclature.....	xv
Chapter 1.....	1
1 Introduction.....	1
1.1 Motivation.....	2
1.2 Objectives.....	3
Chapter 2.....	5
2 Literature Review.....	5
2.1 Perovskite Degradation Mechanisms.....	5
2.2 Encapsulation Strategies.....	8
2.2.1 Glass-to-Glass Encapsulation.....	10
2.2.2 Polymer Encapsulation.....	11
2.2.3 Inorganic Thin Film Encapsulation.....	14
2.2.4 Hybrid Encapsulation.....	17
2.2.5 Conclusions and Future Research Directions.....	20
2.3 Materials for Inorganic Thin Film Encapsulation.....	21
Chapter 3.....	24

3	Pulsed Laser Deposition.....	24
3.1	Experimental.....	24
3.1.1	Experimental Design.....	26
3.2	Coating Appearance.....	27
3.3	Composition of Thin Films.....	28
3.4	Thin Film Morphology	35
3.5	Thin Film Uniformity	39
3.6	Conclusions.....	43
	Chapter 4.....	45
4	Optical Properties.....	45
4.1	Extinction Coefficients and Refractive Indices	46
4.2	Transmittance, Reflectance and Absorptance.....	49
4.2.1	Experimental.....	49
4.2.2	Results and Discussion	51
4.3	Optical Bandgap.....	62
4.4	Conclusions.....	66
	Chapter 5.....	68
5	Coating Durability.....	68
5.1	Adhesion	68
5.2	Abrasion Resistance.....	69
5.3	Chemical Stability.....	71
5.4	Conclusions.....	73
	Chapter 6.....	74
6	Perovskite Degradation Studies	74
6.1	Experimental.....	74
6.1.1	Perovskite Layer Deposition.....	74

6.1.2	UV Degradation Methodology	76
6.2	Experimental Control.....	78
6.3	Predicted Performance of UV-Protection Films	82
6.4	Results & Discussion	83
6.4.1	Appearance	83
6.4.2	Sources of Error	86
6.4.3	Changes in Transmittance.....	87
6.4.4	X-Ray Diffraction	91
6.5	Projected Effectiveness in Solar Cells	93
6.5.1	Addition of a TiO ₂ ETL	94
6.6	Conclusions.....	99
Chapter 7	101
7	Conclusions and Recommendations	101
References	105
Appendices	123
Curriculum Vitae	130

List of Tables

Table 1: Notable glass-to-glass perovskite solar cell encapsulations from the literature. WVTR is reported at ambient conditions in $\text{g}\cdot\text{m}^{-2}\cdot\text{day}^{-1}$	11
Table 2: Notable polymer perovskite solar cell encapsulations from the literature. WVTR is reported at ambient conditions in $\text{g}\cdot\text{m}^{-2}\cdot\text{day}^{-1}$. 'N.R.' indicates that a value was 'not reported.'	13
Table 3: Notable thin film perovskite solar cell encapsulations from the literature. WVTR is reported in $\text{g}\cdot\text{m}^{-2}\cdot\text{day}^{-1}$. 'N.R.' indicates that a value was 'not reported.'	16
Table 4: Notable hybrid perovskite solar cell encapsulations from the literature. WVTR is reported in $\text{g}\cdot\text{m}^{-2}\cdot\text{day}^{-1}$. 'N.R.' indicates that a value was 'not reported.'	18
Table 5: Average grain size of ZnO and AZO crystals grown by room temperature PLD in 5 mTorr O ₂	37
Table 6: Mean thickness, curve-fitting RMSE and scatter index of TiO ₂ , ZnO and AZO thin films deposited by PLD at 2, 5 and 20 mTorr O ₂	41
Table 7: Direct bandgaps (<i>E_g</i>) of TiO ₂ , ZnO and AZO as a function of oxygen partial pressure. Predicted (<i>λ_{predicted}</i>) and experimental (<i>λ_{experimental}</i>) absorption edges are provided to validate the obtained <i>E_g</i>	66
Table 8: Summary of durability test results.....	73
Table 9: Mean height of MAPbI ₃ clusters across three samples deposited using identical spin coating deposition parameters (85 μL, 3000 rpm, 30 s).....	76

List of Figures

Figure 1: Schematic of the large-area pulsed laser deposition system used for experimentation, wherein a series of mirrors and optical lenses focus a KrF excimer laser beam into a vacuum chamber in order to ablate a target and deposit a thin film of target material onto a substrate. 26

Figure 2: Schematic of the thin film deposition experimental design. 27

Figure 3: Photographs of TiO₂, ZnO and AZO thin films deposited on 1 x 1 in. quartz substrates by PLD at oxygen pressures of 2, 5 and 20 mTorr. 28

Figure 4: XPS spectra of the TiO₂ thin film samples deposited by PLD at a) 5 mTorr and b) 20 mTorr O₂. 30

Figure 5: Deconvoluted high-resolution XPS spectra of the a) Ti 2p and b) O 1s peaks of TiO₂ deposited at 5 mTorr O₂ compared to the c) Ti 2p and d) O 1s peaks of TiO₂ deposited at 20 mTorr O₂. 31

Figure 6: XPS spectra of the ZnO thin film samples deposited by PLD at a) 5 mTorr and b) 20 mTorr O₂. 32

Figure 7: Deconvoluted high-resolution XPS spectra of the a) Zn 2p and b) O 1s peaks of ZnO deposited at 5 mTorr O₂ compared to the c) Zn 2p and d) O 1s peaks of ZnO deposited at 20 mTorr O₂. 33

Figure 8: XPS spectra of the AZO thin film samples deposited by PLD at a) 5 mTorr and b) 20 mTorr O₂. 34

Figure 9: Deconvoluted high-resolution XPS spectra of the a) Al 2p and b) O 1s peaks of AZO deposited at 5 mTorr O₂ compared to the c) Zn 2p and d) O 1s peaks of AZO deposited at 20 mTorr O₂. 35

Figure 10: XRD patterns of a) TiO₂, b) ZnO, and c) AZO thin films deposited by room-temperature PLD in 5 mTorr O₂. 36

Figure 11: FESEM images of pulsed laser deposited: TiO ₂ in a) 5, and b) 20 mTorr O ₂ ; ZnO in c) 5 and, d) 20 mTorr O ₂ , and; AZO in e) 5, and f) 20 mTorr O ₂	38
Figure 12: Scaled schematic of a 3 in. silicon wafer, indicating the reflectance spectrophotometry probing locations ('x').....	40
Figure 13: Visualization of the thickness of (a, b, c) TiO ₂ , (d, e, f) ZnO and (g, h, i) AZO thin films deposited by PLD at (a, d, g) 2, (b, e, h) 5 and (c, f, i) 20 mTorr O ₂ across the 3 in. diameter silicon wafer.....	42
Figure 14: Refractive indices at $\lambda = 368$ nm of TiO ₂ , ZnO and AZO thin films deposited by PLD at 2, 5 and 20 mTorr O ₂	47
Figure 15: Extinction coefficients at a) $\lambda = 368$ nm and b) $\lambda = 400$ nm of TiO ₂ , ZnO and AZO thin films deposited by PLD at 2, 5 and 20 mTorr O ₂	48
Figure 16: Scaled schematic of a 1 x 1 in. quartz substrate, indicating the spectroscopy probing locations ('x').	50
Figure 17: UV-Visible light transmittance spectra of a) TiO ₂ , b) ZnO, and c) AZO coatings deposited by PLD at oxygen partial pressures of 0, 2 and 20 mTorr.....	51
Figure 18: NIR light transmittance spectra of a) TiO ₂ , b) ZnO, and c) AZO coatings deposited by PLD at oxygen partial pressures of 0, 2 and 20 mTorr.....	56
Figure 19: UV-Visible-NIR Light Reflectance of a) TiO ₂ , b) ZnO, and c) AZO coatings deposited by PLD at oxygen partial pressures of 0, 2 and 20 mTorr.....	58
Figure 20: Percentage of a) UV-B, b) UV-A, and c) visible light irradiated from the Sun that is absorbed and reflected by the TiO ₂ , ZnO and AZO thin films as a function of the oxygen partial pressure at which they were deposited.	60
Figure 21: Absorptance spectra for the a) direct and b) indirect bandgaps of TiO ₂ deposited by PLD at oxygen pressures of 2, 5 and 20 mTorr. Black dashed lines are used to extrapolate <i>E_g</i> from their intersection with the abscissa.....	63

Figure 22: Absorptance spectra for the direct bandgaps of a) ZnO and b) AZO deposited by PLD at oxygen pressures of 2, 5 and 20 mTorr. Black dashed lines are used to extrapolate <i>E_g</i> from their intersection with the abscissa.....	65
Figure 23: Microscope images (5x magnification) of (a) TiO ₂ , (b) ZnO, and (c) AZO thin films deposited at 5 mTorr O ₂ , (i) before and (ii) after the MIL-C-48497A moderate abrasion test.	70
Figure 24: UV-Vis Transmittance of a) TiO ₂ , b) ZnO and c) AZO thin films before and after the MIL-C-48497A moderate abrasion test. All spectra are taken with air as a reference.	71
Figure 25: Camera images of the TiO ₂ , ZnO and AZO coatings before and after being subject to the MIL-C-48497A chemical solubility test.	72
Figure 26: FESEM images at a) 1.00k and b) 5.00k magnification of the pristine perovskite layer deposited on a quartz substrate.	75
Figure 27: a) Schematic of the testing setup for UV degradation experiments with b) an enlarged view of the irradiated coated quartz sample layer configuration. Note that this schematic is not to-scale.	77
Figure 28: Camera images of perovskite-coated quartz samples degraded for 8 and 96 hours under UV and ambient light, respectively.	79
Figure 29: FESEM images at 50.0 k magnification of MAPbI ₃ a) before and b) after exposure to 8 hours of UV radiation.	80
Figure 30: UV-Vis-NIR transmittance spectra of the perovskite coatings exposed to a) UV light and b) ambient over the course of 8 and 96 hours, respectively.....	80
Figure 31: Percentage of 368 nm wavelength light transmitted by TiO ₂ , ZnO and AZO thin films deposited by PLD at 2, 5 and 20 mTorr O ₂	83
Figure 32: Camera images of thin film-protected perovskite samples exposed to UV light for 8 hours.....	84

Figure 33: UV-Vis-NIR transmittance as a function of UV light exposure time of perovskite samples protected by TiO ₂ thin films deposited at a) 2, b) 5, and c) 20 mTorr O ₂	87
Figure 34: UV-Vis-NIR transmittance as a function of UV light exposure time of perovskite samples protected by ZnO thin films deposited at a) 2, b) 5, and c) 20 mTorr O ₂	88
Figure 35: UV-Vis-NIR transmittance as a function of UV light exposure time of perovskite samples protected by AZO thin films deposited at a) 2, b) 5, and c) 20 mTorr O ₂	89
Figure 36: Normalized average change in NIR (900 nm < λ < 2000 nm) transmittance of thin film protected perovskite exposed to 8 hours of UV radiation.	90
Figure 37: XRD patterns of MAPbI ₃ perovskite b) without and with c) TiO ₂ , d) ZnO, and e) AZO UV protection thin films deposited by PLD at 20 mTorr O ₂ following 8 hours of UV radiation. The XRD pattern of a) pristine uncoated MAPbI ₃ prior to UV radiation is shown for comparison.	92
Figure 38: An enlarged view of the irradiated coated quartz sample layer configuration with addition of a TiO ₂ layer that mimics the electron transport layer in PSCs. Note that this schematic is not to-scale.	95
Figure 39: Camera images of ZnO-protected perovskite samples with a TiO ₂ ETL after 8 hours of UV radiation. For comparison, images of samples degraded without TiO ₂ ETLs and/or thin UV-protection films are also provided.	96
Figure 40: Normalized average change in NIR (900 nm < λ < 2000 nm) transmittance of uncoated and ZnO-protected perovskite with and without a TiO ₂ ETL after 8 hours of UV exposure.	97
Figure 41: UV-Visible light absorptance spectra of a) TiO ₂ , b) ZnO, and c) AZO coatings deposited by PLD at oxygen partial pressures of 0, 2 and 20 mTorr.....	128
Figure 42: Emission spectra of UV lamps a) 1, b) 2, and c) 3 used for perovskite photodegradation.....	129

List of Appendices

Appendix A: Integration Error Sample Calculations.....	123
Appendix B: Supplemental Material	128

List of Abbreviations, Symbols and Nomenclature

Abbreviation/Symbol	Full Form
ALD	Atomic layer deposition
AZO	Aluminum-doped zinc oxide
CVD	Chemical vapour deposition
E_g	Bandgap energy
ETL	Electron transport layer
FESEM	Fuel emission scanning electron microscopy
FF	Fill factor
FWHM	Full width at half maximum
HTL	Hole transport layer
IEC	International Electrotechnical Commission
ISOS	International Summit on Organic Photovoltaic Stability
J_{sc}	Short circuit current density
k	Extinction coefficient
λ	Wavelength
MA	Methylammonium
MBE	Molecular beam epitaxy
n	Refractive index
NIR	Near-infrared
OTR	Oxygen transmission rate
PCE	Power conversion efficiency
PIB	Polyisobutylene
PLD	Pulsed laser deposition
P_{O_2}	Oxygen partial pressure
PSC	Perovskite solar cell
PVD	Physical vapour deposition
R2R	Roll-to-roll
RH	Relative humidity
RMSE	Root mean square error
σ	95% confidence interval around the mean
SQ	Shockley-Queisser
TFE	Thin film encapsulation
TiO ₂	Titanium dioxide
UV	Ultraviolet
Vis	Visible
V_{oc}	Open-circuit voltage
WVTR	Water vapour transmission rate
XPS	X-ray photoelectron spectroscopy
XRD	X-ray diffraction
ZnO	Zinc oxide

Chapter 1

1 Introduction

In the history of all photovoltaic technologies, the swift evolution of perovskite solar cells (PSCs) remains completely unprecedented. With the achievement of efficiencies that have increased from 14% to as high as 25.7% in less than 10 years [1], PSCs are on the verge of disrupting the incumbent crystalline silicon technology. These efficiencies are a result of high optical absorption, long carrier diffusion lengths and ambipolar carrier mobilities, and lead to the generation of exceptional open circuit voltages (V_{oc}) as high as 1.2 V [2]. According to the Shockley-Queisser (SQ) limit, the photo-conversion efficiency (PCE) of perovskite solar cells with absorber band gaps of 1.6 eV can reach 30.14%, corresponding to a short circuit current density (J_{sc}) of 25.47 mA/cm², a V_{oc} of 1.309 V and a fill factor (FF) of 90.5% [3].

Fundamentally, a perovskite is any material which has a crystal structure that can be described by the general chemical formula ABX_3 . Herein, A represents a cation, B represents a metal cation with two valence electrons, and X represents an anion [4]. Since a variety of elements can be chosen to fill the A, B or X locations in the crystal structure, perovskites can easily be tuned for their physical, optical, and electrical properties. The highest efficiencies reported to-date are for the hybrid organic-inorganic lead halide perovskite, $CH_3NH_3PbX_3$ (X = I, Br, Cl), for which the shorthand notation, $MAPbX_3$, is commonly used. Organic-inorganic lead halide perovskites will be the focus of this work, and, unless otherwise stated, the subject of any reference to the term perovskite.

Recent life cycle assessments and techno-economic analyses have indicated that delaying degradation and extending the lifetime of perovskite solar cells is essential for sustainability and commercial viability [5, 6]. Since competitive efficiencies have already been demonstrated, the success of perovskite solar cells relies now on the improvement of their stabilities. To ensure that this technology will be profitable, lifetimes of at least 15 years [6], but ideally 25 years should be realized [7]. The solution, however, is not so straightforward. Perovskites degrade readily upon exposure to oxygen and moisture,

therefore necessitating strategies for degradation mitigation or prevention. Additionally, the perovskite crystals are thermally unstable and have low decomposition temperatures as a result of their ionic nature and the use of organic methylammonium (CH_3NH_3^+ , MA) cations. Photo-induced degradation in the presence of energetic ultraviolet (UV) light constitutes another major issue for the commercialization of perovskite solar cells.

Encapsulation of devices is one of the most promising strategies for extending perovskite solar cell lifetimes. However, much progress remains to be made before the devices can be considered commercially-viable. In particular, limited efforts to-date have sought to elucidate the mechanisms of photodegradation in perovskites or to target encapsulation strategies which can prevent it. Metal oxide semiconductors are ideal candidates for screening UV light because: (1) they have bandgaps which can be tuned to absorb UV wavelengths of light; (2) are themselves intrinsically resistant to degradation due to their inorganic nature, and; (3) are abundantly available and low in cost. Room-temperature pulsed laser deposition has been identified as a facile means of depositing highly uniform metal oxide thin films, particularly because it allows for controlled adjustment of the thin film properties by altering deposition parameters such as the oxygen pressure. This work aims to extend the lifetime of perovskite solar cells by the novel encapsulation of devices with transparent pulsed laser deposited titanium dioxide (TiO_2), zinc oxide (ZnO) and aluminum-doped zinc oxide (AZO) thin film coatings optimized to block UV-light, thereby bridging the gap between lab-scale success and large-scale commercialization.

1.1 Motivation

In the face of increasing energy demands and growing concerns over global warming, there is a heightened need for a sustainable energy conversion technology that can replace the conventional approaches derived from non-renewable resources. Photovoltaics represent a promising alternative due to the abundance of sunlight and their ability to operate with virtually no associated greenhouse gas emissions. However, achieving parity with fossil fuel electricity production costs remains necessary to secure large investments, make solar purchases economically fruitful and promote the widespread adoption of photovoltaic technologies. With efficiencies already comparable to polycrystalline silicon and thin-film solar cells, but having lower associated production costs, perovskite solar cells can be

considered as a disruptive technology that may soon replace the incumbent silicon one and lead to a larger share of electricity produced from renewable solar sources. However, the susceptibility of perovskites to degradation limits their adoption. Therefore, the motivation for seeking to accelerate the commercialization of perovskite solar technologies by advancing encapsulation effectiveness is to provide a more economically-competitive and sustainable alternative to silicon-based solar panels and, ultimately, relief from the global energy crisis.

1.2 Objectives

Based on the aforementioned motivations, this work has the following objectives:

1. Perform an in-depth review of current progress in perovskite solar cell encapsulation in order to establish efficient strategies for future technological enhancement.
2. Successfully deposit highly uniform TiO_2 , ZnO and AZO thin films by room-temperature pulsed laser deposition, and study the influence of oxygen partial pressure during growth on coating appearance, elemental composition, oxidation state and morphology.
3. Investigate the relationship between the PLD oxygen pressure and the optical properties of TiO_2 , ZnO and AZO thin films, with a focus on implications for perovskite solar cell encapsulation. Additionally, identify the most suitable combination of materials and oxygen pressures for perovskite photoprotection, where an ideal thin film encapsulant will:
 - a. block (i.e., reflect or absorb) all degradation-inducing UV wavelengths of light, and simultaneously;
 - b. remain transparent to visible light to minimize sacrifices in the photoconversion efficiency of the PSC.
4. Determine whether TiO_2 , ZnO and AZO thin films deposited on glass substrates are sufficiently durable for use in hybrid thin film/glass encapsulations, in terms of their adhesion, abrasion resistance and chemical resistance.
5. Assess the photoprotective quality of the TiO_2 , ZnO and AZO thin films by subjecting thin film-shielded perovskites to accelerated UV aging.

6. Evaluate the ability of the hybrid TiO_2 , ZnO and AZO thin film/glass encapsulations to delay degradation of perovskites that are in direct contact with a photoactive electron transport layer under accelerated UV aging conditions. Consequently, identify the pulsed laser deposited material and oxygen pressure most suitable for extending the lifetimes of PSCs.
7. Recommend avenues for improvement and directions for future research in the development of inorganic thin films for encapsulating perovskite solar cells.

Chapter 2

2 Literature Review

Long-term stability is a requisite for the widespread adoption and commercialization of perovskite solar cells (PSCs). Encapsulation constitutes one of the most promising ways to extend devices lifetimes without noticeably sacrificing the high power conversion efficiencies (PCEs) that make this solar technology attractive. Among encapsulation strategies, the most investigated methods are: (1) glass-to-glass encapsulation; (2) polymer encapsulation, and; (3) inorganic thin film encapsulation (TFE). In particular, the use of UV-, heat-, water- and/or oxygen- resistant thin films to encapsulate PSCs is a new and promising strategy for extending the lifetime of devices. Thin films can be deposited directly onto the PSC, as in TFE, or can be used in conjunction with glass-to-glass and polymer encapsulation to effectively and efficiently prevent the photo-, thermal-, oxygen- and moisture-induced degradation of the perovskite. This chapter will outline perovskite degradation mechanisms and provide a summary of the progress made to-date in the encapsulation of PSCs, with a particular focus on the most recent and promising advances that employ thin films. It will include an analysis of the influence of deposition techniques, materials, and layer configurations on the quality of the encapsulation. Additionally, the strengths and limitations of TFE approaches will be identified and contrasted against existing encapsulation strategies. Finally, possible directions for future research that can further enhance encapsulation effectiveness and extend PSC lifetimes towards the 25-year target will be proposed.

2.1 Perovskite Degradation Mechanisms

Moisture is one of the most prevalent causes of degradation in perovskite solar cells. Water molecules that are able to permeate through the solar cell stack will react with the A-site organic cation in the perovskite and form hydrogen bonds. This weakens the bonds to the B- and X-site halogenated lead, rendering the perovskite more susceptible to thermal- and UV-induced degradation [8]. Additionally, water will react with X-site iodide ions to decompose the perovskite into hydroiodic acid (HI) and lead iodide (PbI₂) [8]. Therefore, to improve the intrinsic moisture stability of the perovskite, X-site and A-site substitutions

have been suggested. For example, substituting X-site iodine with bromine increases the strength of cation-lead halide bonds, thereby reducing the susceptibility of the perovskite to moisture-induced degradation [9]. Further, since grain boundary defects act as a host for these detrimental reactions with water, passivating perovskite grain boundaries and increasing grain sizes has been found to extend perovskite lifetimes in humid environments [10, 11].

Oxygen is another significant contributor to degradation in perovskite solar cells. Oxidative degradation occurs significantly in both the charge transport and perovskite layers. Gong et al. report a perovskite solar cell with 10.4% efficiency that employs doping the perovskite with selenium (Se) to strengthen the interaction between the MA cation and its inorganic framework, thereby improving stability by 140 times compared to the undoped film, and achieving 70% PCE retention after 700 hours of exposure to air [12]. Moreover, oxidation of organic charge transport layers results in compromised carrier mobility and solar conversion efficiencies [8].

Conversely, metal oxide charge transport layers are not sensitive to oxidation, themselves. However, the most commonly used electron transport layer (ETL), TiO_2 , can absorb oxygen, and when combined with UV light, photo-excitation yields reactive superoxide (O_2^-), which then catalyzes the rapid oxidative degradation of the adjacent perovskite layer [8]. Termed ‘photo-oxidation,’ this is an accelerated form of oxidative degradation, which occurs upon simultaneous exposure to UV light and oxygen.

In general, the mechanisms and harmfulness of photodegradation in PSCs are not well-understood. This is principally due to the large number and complexity of mechanisms that exist interdependently across the PSC architecture. As stated above, the perovskite/ETL interface is a major site for photo-oxidative degradation. However, UV-induced degradation has also been reported to stem from the infiltration of top contact metal ions, the oxidation of organic hole transport layers (HTLs), and the deterioration of the HTL/top contact interface [13]. The perovskite crystal itself is also highly susceptible to photo-oxidation. Photo-excitation of the perovskite increases the density of halide vacancies, which serve as gateways for diffusion of oxygen into the perovskite lattice [14]. Superoxide

species then initiate the degradation by deprotonating the methylammonium cation, resulting in precipitation of the yellow-coloured PbI_2 decomposition product [8]. Perovskite photodegradation in the absence of oxygen has also been reported, however the rate of degradation is much slower and the reaction must be catalyzed by higher photon energy [15].

Principal strategies for preventing photodegradation in PSCs include: (1) replacing TiO_2 with a less photoactive ETL material or modifying the ETL/perovskite interface to inhibit permeation of photo-excited species [16, 17, 18, 19], (2) intrinsically stabilizing the perovskite via A- and X-site substitutions [20, 21], and; (3) adding a new material at the perovskite interface that will prevent transmission of degradation-inducing UV light [22, 23].

Due to the severity of UV-degradation in the presence of a photoactive ETL, replacement/modification of the TiO_2 ETL has been the focus of most efforts to improve PSC photostability. SnO_2 is one of the most promising alternative ETL materials because of its superior band alignment, high electron mobility and improved stability [19]. Namely, Dong et al. observed decreases of 4% and 30% in the PCE of PSCs with SnO_2 and TiO_2 ETLs, respectively, after 100 min of UV illumination [24]. Other strategies such as doping the perovskite with cadmium (Cd) have been used to decrease the density of halide vacancies and increase intrinsic resistance to photo-oxidation [21]. The final proposed strategy – the addition of a UV-absorbing filter – demonstrates great promise due to its simplicity and high theoretical efficacy. For example, Song et al. dispersed perovskite quantum dots in a ZrO_2 matrix, and due to the ability of ZrO_2 to absorb UV light, they observed significant increases in the photoluminescent stability of the perovskite [23]. Furthermore, Chen et al. applied similar principles to not only protect PSCs from photodegradation, but also to harness the energy of UV photons to increase PCE, by introducing a luminescent downshifting scaffold layer in contact with the perovskite [22]. Photostability and PCE were improved via the conversion of incident UV light to harmless visible light: a 92% retention of PCE was obtained for devices with the downshifting scaffold, versus a meager 40% retention for those without it [22].

Heat constitutes a final extrinsic stressor which can accelerate the reactions responsible for degradation in perovskite solar cells [8]. For example, the PbI_2 decomposition product has been observed from prolonged exposure of MAPbI_3 perovskites to temperatures as low as 85°C [25]. This can be detrimental since many manufacturing steps, including the annealing and encapsulating stages, occur at high temperature. Since organic materials are relatively volatile and are most sensitive to thermal degradation, the use of the common MA A-site organic cation can be problematic. Therefore, A-site cation substitution and mixing with more thermally-stable materials such as formamidium (FA), cesium (Cs) and rubidium (Rb), is a popular strategy to improve thermal stability in perovskites [26]. All-inorganic perovskite solar cells represent another promising avenue towards stability, by eliminating issues associated with the thermal degradation of the organic cation. Liu et al. devised a CsPbI_2Br -based perovskite solar cell with an efficiency of 13.3%, which exhibited 80% PCE retention after thermal treatment at 85°C for 360 hours [27]. Another stabilizing strategy was demonstrated by Yun et al., who reduced photo- and thermal degradation by incorporating LiF passivators in organic-inorganic lead halide perovskites with efficiencies up to 20%. Remarkably, they observed 90% PCE retention after 1000 hours of exposure to 1 sun illumination or 85°C temperatures [28].

Significant progress has been made on the intrinsic stabilization of PSCs. While the results are promising, no solution has been reported to-date that has demonstrated the long-term operation of PSCs in outdoor conditions. Therefore, it is clear that a combination of intrinsic stabilization and encapsulation strategies will be necessary to produce a perovskite solar cell that can appropriately withstand the breadth of illumination, heat, moisture and oxygen conditions encountered during manufacturing and operation. Hereafter, this work will focus on reviewing the recent progress in perovskite solar cell encapsulation and on introducing novel directions for further improvement.

2.2 Encapsulation Strategies

To promote commercial viability, a perovskite solar cell encapsulation should: (1) be impermeable to water and oxygen; (2) prevent organic and halide materials volatilized by illumination and/or heat as well as toxic lead-based degradation products from escaping into the environment; (3) have very high visible light transparency so as not to compromise

device efficiencies, (4) be chemically inert, and; (5) have sufficient mechanical durability and abrasion-resistance to tolerate the stress, wear and weathering introduced in normal installation and operation. Important performance metrics for an encapsulant are the water vapour transmission rate (WVTR) and the oxygen transmission rate (OTR). These measurements quantify the amount of water vapour or oxygen that permeate through the encapsulation material per unit time. Since water and oxygen are two of the most pervasive sources of degradation in perovskites, these metrics give a good indication as to the overall quality of the encapsulation. An adequate seal is achieved when the WVTR and OTR are in the range of or less than $10^{-3} - 10^{-6} \text{ g}\cdot\text{m}^{-2}\cdot\text{day}^{-1}$ and $10^{-4} - 10^{-6} \text{ cm}^3\cdot\text{m}^{-2}\cdot\text{day}^{-1}\cdot\text{atm}^{-1}$, respectively [29, 30]. Additionally, though not typically a focus, the ideal encapsulation system should also provide protection against UV irradiation and act as a thermal barrier to prevent UV-induced and thermal degradation.

Generally, encapsulation strategies have involved either the deposition of a transparent thin film encapsulant or the use of an edge sealant material to encapsulate the device between sheets of glass or polymers [31]. This precedent provides a framework for dividing the encapsulation techniques into the following categories: (1) glass-to-glass (Section 2.2.1); (2) polymer (Section 2.2.2), and; (3) inorganic thin film encapsulation (Section 2.2.3). In glass-to-glass encapsulation, a glass cover is used in conjunction with a sealant to form the protective packaging. Conversely, polymer encapsulation encompasses the strategies that employ polymeric barriers – either as cover sheets or thin films. Finally, in the third category, thin inorganic barrier films form the encapsulation. A fourth category – hybrid encapsulations – will also be introduced in Section 2.2.4, and consists of any combination of the aforementioned three encapsulation strategies.

Thin films (organic or inorganic) in particular are uniquely suitable for encapsulation because they can serve as dense, pin-hole-free barriers to oxygen and water, yet remain lightweight and thin enough to not adversely affect the mechanical flexibility of the solar stack and can thus be compatible with roll-to-roll processing. This work will briefly contextualize the progress made to-date in perovskite solar cell encapsulation, with an emphasis on techniques that incorporate thin barrier films. The most noteworthy encapsulation examples from the literature are summarized in Table 1-4. Therein, the PCE

of the encapsulated PSC and a schematic of the encapsulation are provided. Additionally, the WVTR of the encapsulant and outcomes of stability testing (% PCE retained) are given to provide a framework for comparing encapsulation strategies.

2.2.1 Glass-to-Glass Encapsulation

Derived from the standard encapsulation technique of the silicon solar technology, glass-to-glass encapsulation sandwiches the perovskite solar cell between two sheets of glass which are sealed together by means of a sealant. Since the WVTR and OTR of glass are near zero, glass-to-glass encapsulation provides excellent protection from water- and oxygen-induced degradation, while maintaining high light transparency. Furthermore, since glass is easy to clean, has very good mechanical durability and is currently more cost-effective than alternative encapsulating systems, it is considered a highly efficient and industrially attractive encapsulant material [8]. However, moisture and oxygen ingress through the sealant at the edges of glass-to-glass encapsulated devices is significant enough to cause degradation [32]. As a result, recent efforts have been placed on optimizing sealant materials such that the WVTR and OTR are minimized. For example, butyl rubber edge sealants, such as polyisobutylene (PIB), have attracted considerable attention for their low WVTR ($10^{-2} - 10^{-3} \text{ g}\cdot\text{m}^{-2}\cdot\text{day}^{-1}$) [33]. Like PIB, many encapsulant adhesives and edge sealants are thermo-curable. However, curing at high temperature can degrade thermally unstable perovskites and reduce power conversion efficiencies even before ageing tests begin [34]. While UV-curable epoxies are more costly, they are advantageous in that heat need not be applied to form the seal [32]. But, UV light, particularly in the presence of water and/or oxygen can also cause perovskite degradation. Nevertheless, Dong et al. observed a significant improvement in the PCE of devices encapsulated with a UV-curable epoxy (14.8 %) compared to a thermally-curable one (8.9 %) [35]. To eliminate the need for a sealant altogether, hermetic glass frit encapsulation has also been proposed [36]. Table 1 compares PIB and glass frit sealed glass-to-glass encapsulations, demonstrating extremely low WVTR and high corresponding retained PCEs after aging. However, in both cases, the PSC has low initial PCE as a result of degradation caused by the encapsulation process and/or substitutions to internally stabilize the solar stack.

Many researchers believe that the competitiveness of perovskite solar cells lies almost exclusively in their efficiencies. Others are willing to incorporate more inexpensive materials and processes to reduce costs, even if it means sacrificing some efficiency. In order to keep the price per Watt (\$/W) of a perovskite solar module low, these researchers are keen on retaining device flexibility, such that the solar cells can be made at the large-scale by low-cost roll-to-roll (R2R) processing. Recent work on ultra-thin glass encapsulation [37] has produced perovskite solar cells with retained flexibility, but further studies are required to properly assess their long-term stabilities.

Table 1: Notable glass-to-glass perovskite solar cell encapsulations from the literature. WVTR is reported at ambient conditions in $\text{g}\cdot\text{m}^{-2}\cdot\text{day}^{-1}$.

Ref.	PCE	Encapsulation Method	WVTR	Stability Test(s)	% PCE Retained
GLASS-TO-GLASS ENCAPSULATION					
[33]	9%	Glass with PIB seal	Glass: negligible PIB: $10^{-2} - 10^{-3}$	(1) 540 h at 85°C, 85% RH (2) 200 thermal cycles from -40°C to 85°C	(1) ~100% (2) ~100%
[36]	8.2%	Glass frit	Hermetic	(1) 50 h at 85°C, 85% RH (2) 70 thermal cycles from -40°C to 85°C	(1) ~100% (2) 98%

2.2.2 Polymer Encapsulation

Since glass-to-glass encapsulation is not inherently compatible with R2R processing, recent attention has been placed on polymer cover encapsulation. Herein, polymer sheets sealed with thermally-/UV-curable epoxies or pressure sensitive adhesives are used to encapsulate a perovskite solar cell, providing a barrier against extrinsic stressors such as moisture and oxygen. Many low-cost, flexible polymers, such as PET, PMMA and PC, have been used as encapsulating materials, however, much like with glass-to-glass encapsulation, moisture and oxygen ingress through sealants and degradation during curing persists [32]. To overcome this challenge, the deposition of solution-processed polymer layers directly on top of devices has been proposed [38, 39]. McKenna et al. [39] deposited

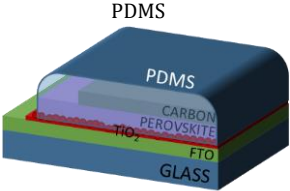
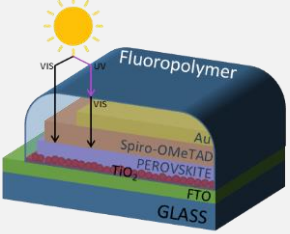
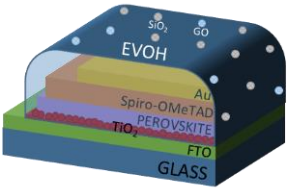
800 nm thin polymer films (i.e., PMMA, PC, EC, and PMP) directly on top of perovskite layers by spin coating and evaluated their ability to inhibit degradation. When exposed to 60°C heat at ambient conditions for 432 hours, the uncoated perovskite film was completely degraded, while the PMMA-encapsulated film remained in pristine condition (no evidence of PbI₂ formation). It is unsurprising that, of the polymers tested, PMMA provided the best device longevity because it has the lowest WVTR (55.2 g·m⁻²·day⁻¹) and OTR (4.8 cm³·m⁻²·day⁻¹·atm⁻¹) [39].

Bella et al. [40] also employed an innovative polymeric coating strategy to simultaneously slow water permeation and prevent UV-induced degradation of perovskite solar cells. By spin-coating devices with luminescent downshifting fluoropolymers that absorb incident UV light and re-emit it to the perovskite active layer as visible light, UV-induced degradation is effectively eliminated without sacrificing any photocurrent (PCE = 19%). Concurrently, the multifunctional polymeric coating is hydrophobic and provides a strong barrier to water-induced degradation. Notably, devices encapsulated on the top and bottom with ~5 μm films of this fluoropolymer demonstrated a 95% retention in PCE after 3 months of exposure to outdoor elements including heavy rain and temperatures ranging from -3 to +27°C.

Despite these promising findings, the relatively high WVTR (10⁰ – 10² g·m⁻²·day⁻¹) and OTR (10¹ – 10² cm³·m⁻²·day⁻¹·atm⁻¹) of standard polymers limit long-term encapsulation effectiveness [32]. To this end, the incorporation of additives in polymer matrices to form polymer composite encapsulants with unique photo-, moisture- and/or oxygen-interactions has demonstrated potential for improved stability [41, 42, 43]. Jang et al. [43] fabricated a 100 μm-thick film of poly(vinyl alcohol-co-ethylene) (EVOH) copolymer with dispersions of SiO₂ and graphene oxide (GO) fillers. The SiO₂ inhibited water permeation by rendering the pathway for penetration through the polymer more tortuous, while the hydrophobicity of the GO repelled water molecules. By including these dispersions, the EVOH/SiO₂/GO composite polymer has a remarkable WVTR of 3.34×10⁻³ g·m⁻²·day⁻¹, compared to 4.72×10⁻² g·m⁻²·day⁻¹ for EVOH only. Perovskite solar cells encapsulated with the EVOH composite by means of a UV-curable adhesive retained 86% of their original PCE after 5 hours of direct exposure to water. Table 2 summarizes the polymer encapsulation strategies

discussed herein, demonstrating higher WVTR, on average, than with glass-to-glass encapsulations. While all stability tests yield high PCE retention, many of the test conditions were not as harsh as those described in Table 1, and constitute less accelerated forms of aging.

Table 2: Notable polymer perovskite solar cell encapsulations from the literature. WVTR is reported at ambient conditions in $\text{g}\cdot\text{m}^{-2}\cdot\text{day}^{-1}$. 'N.R.' indicates that a value was 'not reported.'

Ref.	PCE	Encapsulation Method	WVTR	Stability Test(s)	% PCE Retained
POLYMER ENCAPSULATION					
		PDMS			
[38]	8.6%		$\sim 10^2$	3000 h at 25°C, 20% RH	$\sim 100\%$
		Downshifting fluoropolymer			
[40]	19%		N.R.	(1) 3 months outdoors (rain, -3 to +27°C) (2) 1 month at 25°C, 95% RH	(1) 95% (2) 96%
		EVOH with SiO ₂ and GO additives			
[43]	17.2%		3.34×10^{-3}	5 h of direct contact with water at 25°C	86%

Inorganic materials such as metal oxides form denser films with substantially lower WVTR and OTR than their polymer counterparts. To take advantage of this, some researchers have combined transparent thin metal oxide films with polymer encapsulation to provide superior resistance to water- and oxygen-induced degradation. For example, Chang et al. [44] deposited 50 nm thin films of Al_2O_3 by atomic layer deposition (ALD) onto PET substrates that they then used to encapsulate PSC devices. The Al_2O_3 thin film served as an excellent barrier to moisture and oxygen, having WVTR and OTR of $9.0 \times 10^{-4} \text{ g}\cdot\text{m}^{-2}\cdot\text{day}^{-1}$ and $1.9 \times 10^{-3} \text{ cm}^3\cdot\text{m}^{-2}\cdot\text{day}^{-1}\cdot\text{atm}^{-1}$, respectively. Moderate increases in WVTR and OTR

were observed for Al₂O₃-coated PET substrates subject to bend testing, indicating that while somewhat compatible with flexible devices, further effort may be required to increase the reliability and longevity of the encapsulation and to prevent partial delamination of rigid inorganic coatings from soft polymeric substrates. Nonetheless, encapsulated devices exposed to ambient conditions (30°C, 65% RH) for 42 days demonstrated negligible degradation in PCE.

The sequential combination of organic and inorganic layers to form organic-inorganic hybrid flexible multilayers has also been demonstrated to further reduce water and oxygen permeation through polymer-based encapsulants. The hybrid multilayers are deposited on polymer substrates, such as PET, that serve as the backbone for the encapsulation. Next, a series of organic polymer-based and metal-oxide inorganic thin films are deposited sequentially, wherein the organic layers help to retain flexibility and ductility and passivate interfacial defects, while the inorganic layers provide enhanced fortification against water and oxygen permeation [32]. WVTRs obtained at standard temperature and pressure for organic-inorganic hybrid multilayers are about three orders of magnitude less than that of uncoated PET; at elevated temperature and humidity (38°C, 90% RH), WVTR remains below $10^{-3} \text{ g}\cdot\text{m}^{-2}\cdot\text{day}^{-1}$ [45]. Furthermore, deposition of these complex coating structures in roll-to-roll systems using vacuum-based techniques such as magnetron sputtering has established their compatibility with large-scale production. Kim et al. [46] combined the aforementioned benefits of organic-inorganic hybrid flexible multilayer coatings with the antireflective properties of Nb₂O₅/SiO₂/Nb₂O₅ thin films to create a protective barrier for PSCs that minimizes undesirable light reflection and enhances PCE (17%). Additional experimentation is required to assess the effect of these types of encapsulations on the long-term stability of perovskite solar cells.

2.2.3 Inorganic Thin Film Encapsulation

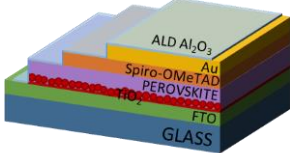
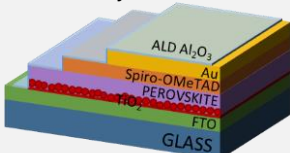
Thin film encapsulation (TFE), wherein a thin barrier film is deposited directly on top of the perovskite solar cell, is considered a next-generation encapsulation strategy since it can overcome many of the issues associated with glass and/or polymer cover encapsulation (e.g., moisture ingress through edge seals). Importantly, TFE is simultaneously compatible with R2R processing and, depending on the deposition technique and material selected,

ultra-low WVTR and OTR can be achieved. In fact, the large variety of materials (e.g., organics, inorganics, organic-inorganic composites, etc.) and deposition techniques (e.g., spin coating, chemical vapour deposition (CVD), physical vapour deposition (PVD), etc.) available in TFE provides a unique opportunity to tailor the properties of the barrier coating to better suit the requirements of the application. Inorganic TFE is distinct from the polymeric thin film encapsulations discussed in Section 2.2.2 in that the thin barrier films are inorganic in nature. As previously detailed, these generally have the advantage of reduced WVTR and OTR compared to their polymeric thin film counterparts. However, a major concern of inorganic TFE is whether the deposition of the thin barrier film can be effectively and efficiently performed at a large-scale; many inorganic TFE strategies involve cost-prohibitive complex vacuum deposition systems with low deposition rates. Adhesion is another concern. Where the thermal expansion coefficient of the thin inorganic encapsulating film is substantially different than that of the solar stack, mechanical stress, stability testing and even normal operation may cause delamination.

Al_2O_3 has gained the most attention in inorganic TFE as a result of its high transparency, electrical insulation and extremely low WVTR ($9.0 \times 10^{-4} \text{ g} \cdot \text{m}^{-2} \cdot \text{day}^{-1}$) and OTR ($1.9 \times 10^{-3} \text{ cm}^3 \cdot \text{m}^{-2} \cdot \text{day}^{-1} \cdot \text{atm}^{-1}$) [47, 48]. ALD is often used to deposit the Al_2O_3 in TFE applications because of the high quality and uniformity of films produced [44]. However, as depicted in Table 3, a trade-off exists in selecting the ALD barrier-film deposition temperature. High temperature depositions yield pinhole/defect-free coatings, but can cause a significant decrease in PCE due to thermal degradation of organic materials during encapsulation. Conversely, low temperature depositions ensure that the thermally sensitive solar-stack retains high PCE after encapsulation, but yield Al_2O_3 films that are more prone to moisture and oxygen ingress. For example, while spiro-OMeTAD-based PSCs fabricated by Choi et al. [47] and encapsulated with 50 nm of ALD-deposited Al_2O_3 demonstrated excellent long-term stability in ambient environments (92% retention in PCE after 7500 hours at 25°C, 50% RH), the PCE of encapsulated devices was moderately compromised compared to that of un-encapsulated devices (16% drop in PCE after encapsulation), due to the elevated ALD deposition temperature of 95°C. Further increases in ALD deposition temperature led to more severely compromised PCEs, particularly when organic HTLs, such as spiro-OMeTAD, were used [47]. To prevent thermal degradation induced by the

encapsulation process, deposition of Al₂O₃ by low-temperature ALD has been proposed. Ramos et al. [48] encapsulated spiro-OMETAD-based PSCs with 16 nm Al₂O₃ thin films deposited by ALD at 60°C. As a result of the reduced operating temperature, encapsulated PSCs had outstanding PCEs as high as 17.4%, representing a 93.6% retention of the original PCE, while the same cells encapsulated at 90°C exhibited a 54% loss in PCE. However, a higher defect density was observed in Al₂O₃ deposited at 60°C, leading to increased water permeation and worse long-term stability outcomes compared to high-temperature Al₂O₃ encapsulations. After 2250 hours of exposure to the same ambient conditions as in the previous study by Choi et al. (25°C, 50% RH), a more significant 25% drop in PCE was reported for PSCs encapsulated with the 60°C ALD-deposited Al₂O₃.

Table 3: Notable thin film perovskite solar cell encapsulations from the literature. WVTR is reported in g·m⁻²·day⁻¹. 'N.R.' indicates that a value was 'not reported.'

Ref.	PCE	Encapsulation Method	WVTR	Stability Test(s)	% PCE Retained
INORGANIC THIN FILM ENCAPSULATION					
		Al ₂ O ₃ by ALD at 95°C			
[47]	15%		1.84×10 ⁻² at 45 °C, 85% RH	7500 h at 25°C, 50% RH	92%
		Al ₂ O ₃ by ALD at 60°C			
[48]	17.4%		N.R.	2250 h at 25°C, 50% RH	75%

New and innovative strategies have been introduced to overcome the challenges associated with the deposition of a pinhole-free, low-temperature inorganic thin film for encapsulation. The inclusion of organic interlayers in the TFE constitutes one such proposition. The purpose of the organic barrier interlayers is to compensate for defects in the inorganic layers by elongating the pathway for water and oxygen permeation, effectively decreasing WVTR and OTR. Additionally, inorganic/organic encapsulations are less prone to delamination than their brittle, all-inorganic counterparts, due to a reduction in residual stresses and an improvement in flexibility [32]. Lee et al. [49] encapsulated PTAA-based PSCs with a 4-dyad multilayer stack of Al₂O₃ (21.5 nm)/pV3D3

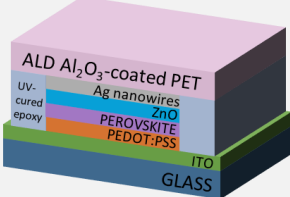
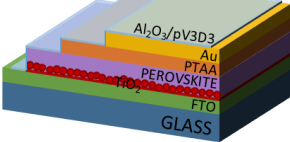
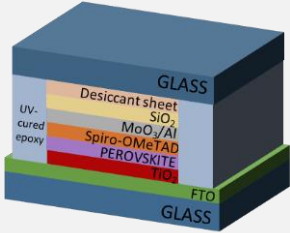
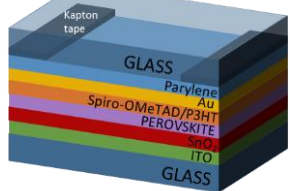
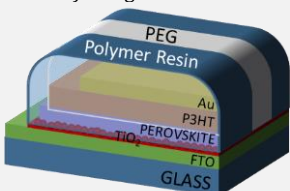
(100 nm) deposited by ALD at 60°C and initiated chemical vapour deposition at 40°C, respectively. Low processing temperatures led to negligible losses in PCE during encapsulation (< 0.3%). Furthermore, the inclusion of pV3D3 organic interlayers produced PSCs with significantly improved stabilities in accelerated ageing conditions: after storage for 300 hours at 50°C and 50% RH, PCEs retained 97% of their initial values. Importantly, this constitutes one of the best stabilities reported for a PSC with an encapsulated PCE higher than 18%.

While much has been done to advance TFE, lifetimes must be extended even further and harsher environmental testing is required to better assess their capacity for degradation prevention. Moreover, further optimization of the TFE deposition process is necessary to overcome limitations associated with the slow deposition rates, scalability and large operating costs of ALD.

2.2.4 Hybrid Encapsulation

Glass-to-glass encapsulation remains one of most commercially-promising due to relatively low processing costs in conjunction with the effective seal produced. However, moisture and oxygen ingress through epoxies and edge sealants remains a concern, preventing the realization of sufficiently long device lifetimes. Similarly, while polymer encapsulations are compatible with R2R processing, high WVTR and OTR limit effectiveness. Finally, while some early success has been demonstrated with TFE, much work remains to reduce operating costs and further improve lifetimes. It is therefore likely that a hybrid packaging which combines inorganic TFE with glass-to-glass or polymer encapsulation, thereby simultaneously taking advantage of the unique optical, mechanical and electronic properties of thin films materials and the strong barrier supplied by bulk polymers or glass, will provide the most effective and efficient means of preventing perovskite degradation.

Table 4: Notable hybrid perovskite solar cell encapsulations from the literature. WVTR is reported in $\text{g}\cdot\text{m}^{-2}\cdot\text{day}^{-1}$. 'N.R.' indicates that a value was 'not reported.'

Ref.	PCE	Encapsulation Method	WVTR	Stability Test(s)	% PCE Retained
HYBRID ENCAPSULATION					
[44]	16.1%	<p style="text-align: center;">Al₂O₃/PET</p> 	Al ₂ O ₃ : 9.0×10^{-4} at 50°C, 50% RH	42 days at 30°C, 65% RH	97%
[49]	18.5%	<p style="text-align: center;">4-dyad Al₂O₃/pV3D3</p> 	5.3×10^{-4} at 38°C, 90% RH	300 h at 50°C, 50% RH	97%
[35]	14.8%	<p style="text-align: center;">SiO₂ with glass cover and desiccant sheet</p> 	N.R.	(1) 48 h AM1.5 illumination at 85°C, 65% RH (2) 432 h outdoors (30- 90% RH)	(1) 80% (2) ~100%
[50]	15.8%	<p style="text-align: center;">Parylene with glass cover</p> 	N.R.	2000 h continuous operation under AM1.5 illumination in N ₂ environment with <5% RH	85%
[51]	10%	<p style="text-align: center;">Polymer resin (embedded with PEG) and glass substrate</p> 	N.R.	830 days at 25°C, 28% RH	79%

Some of the most promising encapsulations that were previously described under other sub-sections actually employed combinations of glass-to-glass, polymer and inorganic thin film encapsulation and, as such, are more appropriately categorized as hybrid encapsulations. For example, the Al₂O₃-coated PET encapsulation reported by Chang et al. [44] that was first introduction in Section 2.2.2 on polymer encapsulation actually involves

a combination of polymer and inorganic TFE strategies. It produced encapsulated devices that demonstrated negligible degradation in PCE after exposure to ambient conditions (30°C, 65% RH) for 42 days. Similarly, the PCE-enhancing organic-inorganic hybrid flexible multilayer coatings (PET/Nb₂O₅/SiO₂/Nb₂O₅/PPFC) by Kim et al. [46] were first introduced in Section 2.2.2 but more aptly constitute a hybrid encapsulation. Finally, Lee et al.'s 4-dyad multilayer stack of Al₂O₃/pV3D3 [49] described in the previous section combines polymer and thin film encapsulations to achieve remarkable PCE retention (97%) after storage for 300 hours at 50°C and 50% RH.

Also in pursuant with this hybrid strategy, Dong et al. [35] employed an encapsulation strategy wherein a 50 nm thin film of SiO₂ was deposited directly onto the device by electron beam deposition, followed by glass-to-glass encapsulation with UV-curable epoxy and a 180 µm piece of desiccant. Encapsulated devices were subject to accelerated ageing tests and remarkably retained 80% of their original PCE after 48 hours under illumination at 85°C and 65% RH. Furthermore, almost full retention of PCE was reported after 432 hours of exposure to humid outdoor conditions where the relative humidity varied between 30 and 90%. Similarly, Liu et al. [50] encapsulated intrinsically stabilized perovskite solar cells with a 2 µm polymeric thin film of parylene by chemical vapour deposition and a cover glass. Impressively, by combining the principles of polymer, thin film and glass-to-glass encapsulation, the stability of the encapsulated devices under AM1.5 illumination was demonstrated for 2,000 hours of continuous operation (PCE > 85% of initial value). Additionally, in one of the longest PSC stability tests published to-date, Fumani et al. [51] obtained 2-year stable PSCs by encapsulating the cathode and anode side of devices with 1.5 mm of polymer resin embedded with poly(ethylene glycol) (PEG) and glass, respectively. The resin provided a thick barrier against the diffusion of oxygen and water, and the PEG additive was used as a phase change material to limit device overheating caused by illumination. Freshly encapsulated devices had PCEs of 10%, which declined only slightly to 7.9% after 830 days (2.3 years) of storage in ambient conditions (25°C, 28% RH).

All of the hybrid encapsulation strategies described throughout this chapter are compared in Table 4. The diversity of all these hybrid encapsulations is reflected in the schematics

and stability test results. Generally, hybrid encapsulations have allowed for high initial PCE and good PCE retention after aging. It should be noted that large differences in the severity of stability tests make direct comparison of different encapsulations difficult. A standardization of testing protocols would therefore provide a means for more efficient optimization of encapsulation techniques.

2.2.5 Conclusions and Future Research Directions

Though stability of PSCs remains a concern, recent improvements to intrinsic stability and hybrid device encapsulation have produced perovskite solar cells with lifetimes up to 2 years [50, 51, 52]. Nonetheless, considerable progress remains to be made before the 15-year lifetimes required for economic feasibility are realized. Furthermore, many of the PSCs that have demonstrated long-term stability on the order of years are limited by relatively poor initial efficiencies due to material substitutions/eliminations for intrinsic stabilization.

As a result of the detrimental nature of water- and oxygen-induced degradation of PSCs, the majority of encapsulations focus on inhibiting moisture and oxygen ingress. However, limited work to-date has focused on using encapsulation strategies to target UV-induced degradation. In fact, UV light constitutes a major factor in perovskite degradation, not only because of illumination-induced reversible phase segregation, but because it catalyzes and accelerates moisture- and oxygen-induced degradation. Therefore, in the absence of UV light, it is conceivable to achieve sufficiently long PSC lifetimes, even for encapsulations with slightly higher-than-ideal WVTR and OTR. This opens the door to obtaining substantially better long-term stabilities with glass-to-glass encapsulation, where moisture and oxygen ingress through the edge sealant is somewhat inevitable, and even for polymer encapsulations, which are limited by inherently poor WVTR and OTR. Thus, the use of a thin film encapsulant material with optical properties tuned to screen or convert UV light into less energetic and harmful irradiation is very compelling. Future research should look to combine the benefits of glass-to-glass or polymer encapsulation with thin film UV-barriers to assess whether this constitutes a step towards PSC longevity. Nonetheless, one thing is for certain: the continued development and evolution of innovative encapsulation

strategies such as this and all those presented in this work is certainly required to bridge the gap between lab-scale PSC success and large-scale commercialization.

Furthermore, this work has elucidated the difficulties associated with direct comparison of PSC encapsulations fabricated by different research groups due to the lack of consistency in aging and stability tests performed. In an effort towards test standardization, some researchers have performed PSC testing according to the International Electrotechnical Commission (IEC) standards (e.g., IEC61646), originally designed to assess the field performance of silicon photovoltaic modules. However, due to the differences in degradation pathways between silicon and perovskite photovoltaics, many researchers are critical that the IEC standards do not comprehensively appreciate or assess for all sources of degradation in PSCs. The testing standards proposed specifically for PSCs at the 2018 International Summit on Organic Photovoltaic Stability (ISOS) constitute a good starting point for discussions of PSC-specific stability tests [45]. However, future effort and consensus from the research community is still required to establish standardized testing protocols better suited to assess the long-term stability of encapsulated PSCs.

2.3 Materials for Inorganic Thin Film Encapsulation

The selection of inorganic thin film encapsulation materials is typically based on which materials can be made into densely packed films with the lowest WVTR and OTR. As a result, this criterion selects for the materials that are the best at preventing water- and oxygen-induced degradation of perovskites. To this end, Al_2O_3 is the most widely used material for inorganic thin film encapsulation. Recently, sequential deposition of Al_2O_3 with very thin (< 30 nm) layers of other inorganic materials such as ZrO_2 [53], ZnO [54], TiO_2 [55], etc., has been employed to further increase the permeation difficulty.

However, an encapsulation strategy targeting the photodegradation of perovskites requires modified material selection criteria. One of the properties that has popularized Al_2O_3 is its ultra-wide bandgap (E_g) of ~ 8.8 eV that delivers nearly uncompromised PSC photoconversion efficiencies, owing to its $\sim 100\%$ transmittance of light of wavelength (λ) > 140 nm [53]. But this same property makes Al_2O_3 unsuitable for photoprotective applications. Instead, materials for preventing UV-induced degradation should have

bandgaps of $E_g \sim 3.1$ eV such that they exhibit strong absorption of UV light ($200 \text{ nm} < \lambda < 400 \text{ nm}$) and no absorption of visible light ($400 \text{ nm} < \lambda < 750 \text{ nm}$). Consequently, the metal oxide semiconductors with which Al_2O_3 has been sequentially layered in recent encapsulation studies, are themselves more appropriate candidates for photoprotection. However, in order to achieve complete absorption of light at energies above the bandgap, their extinction coefficients necessitate deposition of thicker layers than what has previously sufficed in multilayer permeation barriers. These materials can be classified as wide bandgap metal oxide semiconductors, and while their use in PSC encapsulation is limited, they have been applied in a broad range of other fields, including sensors [56, 57], photocatalysis [58, 59], optoelectronics [60, 61], and antireflective coatings [62, 63].

Among wide bandgap metal oxide semiconductors, TiO_2 and ZnO are some of the most commonly employed as a result of their high thermal and chemical stabilities [64, 65], refractive indices and ultraviolet-light extinction coefficients [66, 67]. Furthermore, they are abundantly available, low in cost and easy to deposit by conventional vacuum and solution-based methods. Though TiO_2 and ZnO thin films have been studied extensively over the last three decades, their use as standalone perovskite-photoprotection thin films is novel and has the potential to extend photovoltaic lifetimes and advance the commercialization of PSCs.

TiO_2 and ZnO thin films can provide protection against UV degradation in PSCs without significantly compromising photovoltaic conversion efficiencies because their bandgaps of approximately 3.2 eV result in simultaneous strong UV-light absorption and high visible light transmittance. Moreover, the bandgaps of metal oxide semiconductors can be further optimized by tuning the thin film growth environment. In the case of TiO_2 and ZnO , the influence of temperature, oxygen partial pressure and doping on crystallinity, microstructure and optical properties has been studied thoroughly.

For TiO_2 , room temperature growth yields amorphous thin films, and crystallinity increases with temperature [34]. Moreover, by reducing the oxygen pressure during deposition, oxygen vacancies and Ti^{3+} interstitials are formed which contribute to narrowing the bandgap and increasing the UV absorption of the material [68]. Conversely, depending on

the substrate material, the gaseous environment and the deposition technique, ZnO films grown at room temperature can be amorphous or crystalline [69, 70, 71]. Low oxygen pressures also lead to the formation of oxygen vacancies in ZnO thin films, which can similarly contribute to a slight narrowing of the bandgap [72, 73]. Contrastingly, doping ZnO with a small percentage of aluminum atoms to form AZO will widen the bandgap via the Burstein-Moss effect [74]. Consequently, TiO₂, ZnO and AZO are excellent candidate materials which can be easily optimized for perovskite photoprotection.

Deposition of TiO₂, ZnO and AZO thin films has been performed by a variety of methods, including pulsed laser deposition (PLD) [75, 65], sputtering [76, 77], CVD [78, 79], molecular beam epitaxy (MBE) [80, 81], and solution-based methods [66, 82]. Among these techniques, PLD presents advantages in that the films produced are homogeneous, reproducible and have preserved stoichiometry [24]. Furthermore, the physical and optical properties of the film can easily be tuned by changing the PLD deposition parameters.

Chapter 3

3 Pulsed Laser Deposition

In PLD, a pulsed laser beam is focused on the surface of a solid target material. The laser photons are converted into thermal, chemical and mechanical energy, resulting in the rapid extraction of material from the surface of the target to form a plasma plume which condenses on the substrate [83]. Pulsed laser deposition was selected for the fabrication of the thin film encapsulation layers due to its versatility, reproducibility and precision. This technique produces highly uniform and reproducible films of precise thickness and preserved stoichiometry and is ideally suited for research since its working mechanism permits deposition of nearly all combinations of materials. Moreover, the use of a large-area PLD system, capable of depositing homogenous films over a 3 in.² area, also demonstrates great relevancy to the perovskite photovoltaics industry, in that significant effort is currently focused on scaling research-sized cells (~ 1 in.²) to a more commercially-important module-scale (> 1 in.²). Low-temperature PLD growth of thin films is also of great interest in perovskite solar cell applications because it is less energy intensive and yields more cost-effective vacuum-based thin films. Furthermore, the physical and optical properties of the films can easily be tuned by changing PLD deposition parameters such as the partial pressure of oxygen in the growth environment.

This chapter will examine the effects of oxygen pressure during metal oxide film growth on the resulting appearance, chemical composition and morphology of the coating. Importantly, this constitutes one of the first works to comparatively examine the role of oxygen pressure in room-temperature pulsed laser deposited metal oxide thin films for PSC encapsulation.

3.1 Experimental

TiO₂, ZnO and AZO thin films were deposited on p-type silicon (100) wafers (Polishing Corporation America, 3 in. diameter) and quartz substrates (McMaster-Carr, 1 in. \times 1 in.) by the PLD technique, using 3.5 in. diameter TiO₂ and ZnO and AZO ceramic targets purchased from Kurt J. Lesker with purities of 99.99%, 99.999% and 99.99%, respectively.

The ratio of ZnO to Al₂O₃ in the AZO target is 98:2 weight %. Prior to deposition, silicon wafers were etched in 2.5% HF acid solution for 2 minutes to remove the SiO₂ surface layer, then rinsed with Milli-Q water. Quartz substrates were cleaned by 10-minute sequential ultrasonication in each of the following three solvents: (i) acetone; (ii) isopropanol, and; (iii) methanol. A schematic of the large-area PLD system used for experimentation is given in Figure 1. It consists of a KrF excimer laser (Lambda Physik LPX-210i) with wavelength, $\lambda = 248$ nm, a variable beam attenuator (Microlas), beam steering and shaping optical lenses and mirrors, and a high-vacuum (up to 10^{-7} Torr) stainless-steel chamber (Epion Corp., PLD-3000). Herein, the beam from the KrF excimer laser is focused inside the vacuum chamber using mirrors which re-direct its irradiation pathway. The expanding and focusing lenses modify the size of the laser beam such that it has appropriate intensity and cross-sectional area (i.e., spot-size) for target ablation. Finally, a programmable mirror located at the end of the optical train permits laser rastering and ensures uniform ablation across the width of the target. Previously optimized laser parameters were used to ablate the targets: a laser energy of 600 mJ/pulse was applied at a pulse duration of 20 ns at full width at half maximum (FWHM) and frequency of 50 Hz. The resulting on-target energy density is 1.50 ± 0.25 J/cm² with a laser beam spot size of 4.2 mm². The silicon and quartz substrates to be coated were mounted on a circular Inconel plate with 3 in. diameter such that they face the target with a stand-off distance of 12 cm. To ensure uniform ablation and coating, both the target and substrate holder were rotated during deposition at rates of 17.5 and 35.0 revolutions/min, respectively. All depositions were carried out at room temperature. The PLD system is also equipped with a mass flow controller to adjust the flow of oxygen into the deposition chamber; the amount of oxygen is quantitated to a resolution of 1 mTorr according to its partial pressure.

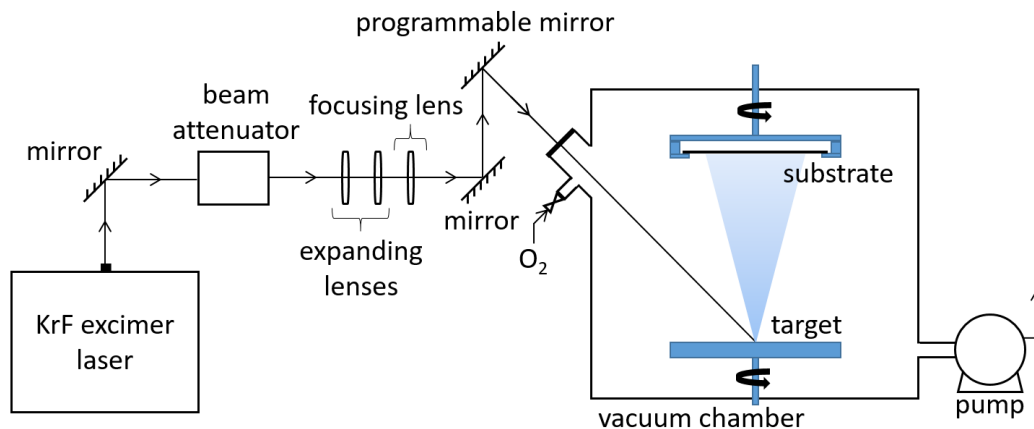


Figure 1: Schematic of the large-area pulsed laser deposition system used for experimentation, wherein a series of mirrors and optical lenses focus a KrF excimer laser beam into a vacuum chamber in order to ablate a target and deposit a thin film of target material onto a substrate.

3.1.1 Experimental Design

It is well known that the introduction of oxygen during metal oxide film growth has a strong influence on morphological and optical properties. Therefore, a goal of this work is to determine not only the material that is the most suitable for UV-protection of PSCs, but also the optimal oxygen partial pressure at which to grow thin films of that material by PLD. A series of preliminary experiments in which thin films of TiO₂, ZnO and AZO were deposited by PLD at oxygen partial pressures between 0 and 54 mTorr were used to determine the optimal oxygen pressure range over which to deposit the thin films for the encapsulation application. At 54 mTorr O₂, film growth was slow and UV absorption was negligible. Conversely, in vacuum (i.e., $<10^{-7}$ Torr O₂) films were opaque to visible light. Ultimately, a narrowed range, consisting of three oxygen pressures – 2, 5 and 20 mTorr – was selected since it produced films with more balanced UV absorption and visible light transmittance properties, hypothesized to be of greater interest for UV-protection applications. The number of oxygen pressures studied was set to three to provide sufficient data points to elucidate the relationship between oxygen pressure and light transmittance, while balancing the time and cost associated with each additional deposition.

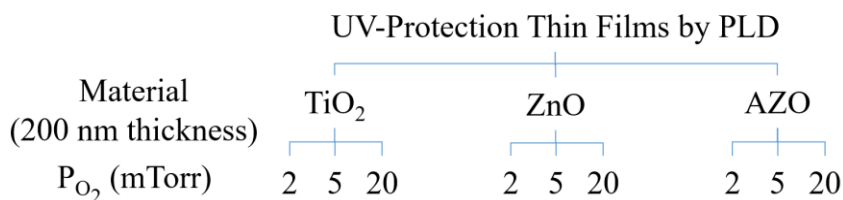


Figure 2: Schematic of the thin film deposition experimental design.

It should be noted that the pressure values selected are not evenly distributed across the total pressure range. These values were carefully selected to provide a spread in the optical transmission data because there is a more rapid increase in oxygen vacancies at low oxygen pressures [73, 84].

Studies have found that deposition rate decreases linearly with oxygen pressure [85]. Therefore, to control for the influence of thickness on optical transmittance, the deposition time was manipulated to achieve a constant film thickness of approximately 200 nm (for photoprotection purposes) across all oxygen pressures. This thickness was selected based on the extinction coefficients of the least absorptive candidate UV-protection material (i.e., TiO₂ deposited at 20 mTorr O₂), such that the thin films produced would exhibit complete absorption of light at wavelengths less than their absorption edge.

3.2 Coating Appearance

The appearance of the thin films after deposition varied depending on the target material and oxygen partial pressure used. High resolution camera images taken of the pulsed laser deposited thin films on their colourless, transparent quartz substrates are given in Figure 3.

While all coatings are highly transparent, their colouring is determined by the difference in reflectivity of each combination of materials and oxygen pressures. The TiO₂ coatings appear the most coloured and have a blue/purple tint. As oxygen pressure is increased from 2 to 20 mTorr, the appearance of TiO₂ coatings changes from coloured to entirely colourless. The ZnO coatings have a very slight pink/yellow tint that does not change significantly with oxygen pressure. On the contrary, AZO thin films lose their yellow tint

with increasing oxygen pressure, such that they are nearly colourless at 20 mTorr O₂. Overall, the TiO₂ thin films exhibit the largest variation in colour with oxygen pressure.

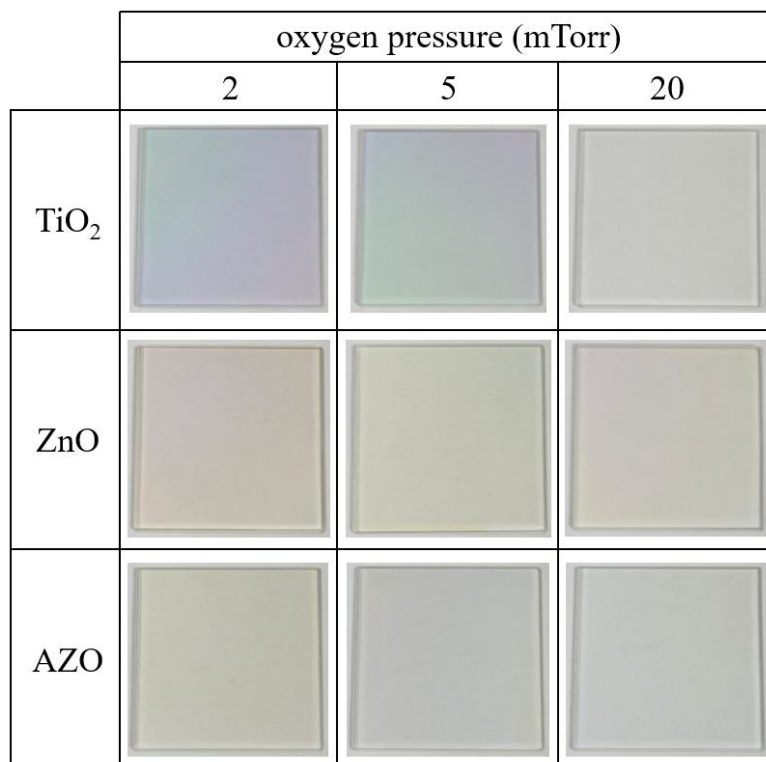


Figure 3: Photographs of TiO₂, ZnO and AZO thin films deposited on 1 x 1 in. quartz substrates by PLD at oxygen pressures of 2, 5 and 20 mTorr.

A gradient in colour exists across each substrate due to a spatial variation in the thin film thickness. It should be noted that with thin films, even nanoscale differences in thickness can have significant effects on the interference of reflected light, producing drastically different colouring. The degree to which the thickness varies spatially across the substrate is analyzed in Section 3.5.

3.3 Composition of Thin Films

X-ray photoelectron spectroscopy (XPS) was used to confirm the chemical composition of the pulsed laser deposited TiO₂, ZnO and AZO thin films on quartz and to identify the presence of oxygen vacancies at high (20 mTorr) and low (5 mTorr) oxygen partial pressures. XPS (Kratos AXIS Supra) analysis was performed by Surface Science Western

using a Kratos AXIS Supra X-ray photoelectron spectrometer on an analysis area of $300\ \mu\text{m} \times 700\ \mu\text{m}$ and a pass energy of 160 eV and 20 eV for survey and high-resolution scans, respectively. The surface of each sample was probed to a depth of 7 – 10 nm with a detection limit of 0.1 – 0.5 atomic %.

The full spectrum survey scans of the TiO₂ samples grown at 5 and 20 mTorr O₂ are given in Figure 4. All peaks can be attributed to the expected TiO₂ material, with the exception of the C 1s and N1s peaks which arise as a result of hydrocarbon-based surface contamination due to handling and exposure to ambient environments. High resolution XPS spectra of the Ti 2p and O 1s energy levels of the TiO₂ films at 5 and 20 mTorr O₂ are given in Figure 5. The C 1s peak at 285 eV was used to calibrate the spectra. Figure 5 a) and c) show the Ti 2p peak resolved into two Gaussian components: the Ti 2p_{3/2} peak at 458.6 eV and the Ti 2p_{1/2} peak at 464.3 eV, each of which are attributed to the Ti⁴⁺ ions in TiO₂ [86]. Ti⁴⁺ is the electronic configuration of Ti atoms in stoichiometrically oxidized TiO₂. However, closer inspection reveals that the Gaussian fitting is not perfect. In particular, there is a small shoulder on the lower binding energy side of the Ti 2p_{3/2} peak for both the 5 and 20 mTorr depositions (indicated by an arrow). This shoulder is attributed to the presence of Ti³⁺ ions, which are related to oxygen vacancies and typically form in low oxygen pressure conditions when there is insufficient O₂ to produce stoichiometric TiO₂ [87].

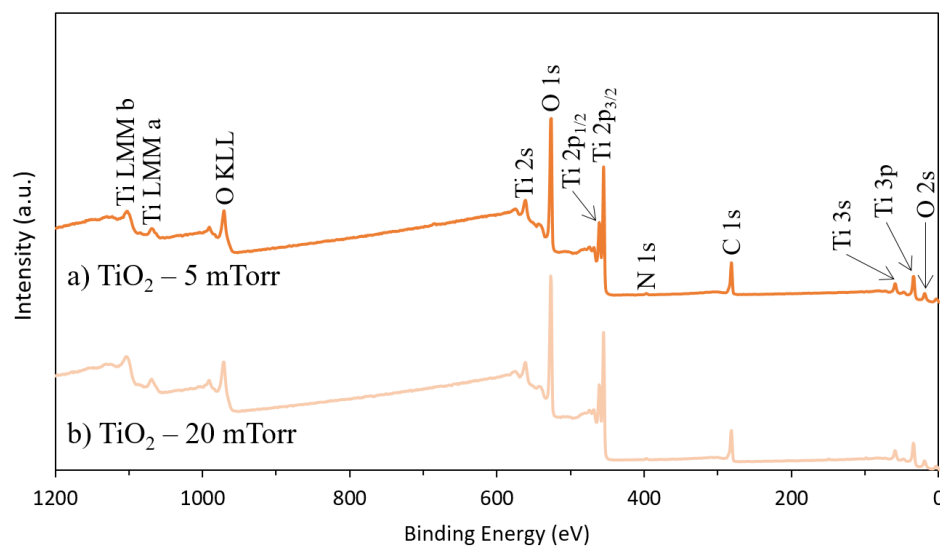


Figure 4: XPS spectra of the TiO₂ thin film samples deposited by PLD at a) 5 mTorr and b) 20 mTorr O₂.

It is expected that reducing oxygen pressure during film growth should yield a proportionally larger concentration of Ti³⁺ ions. However, in the present study, the size of the shoulder does not increase discernably with decreasing oxygen pressure from 20 to 5 mTorr. Considering that a previous study reported only a very slight increase in shoulder size when the pressure was reduced by five orders of magnitude [87], it is likely that there is, in fact, more Ti³⁺ in the TiO₂ deposited at 5 mTorr than at 20 mTorr, but that the increase cannot be appreciated by XPS given the relatively small decrease in pressure of less than one order of magnitude.

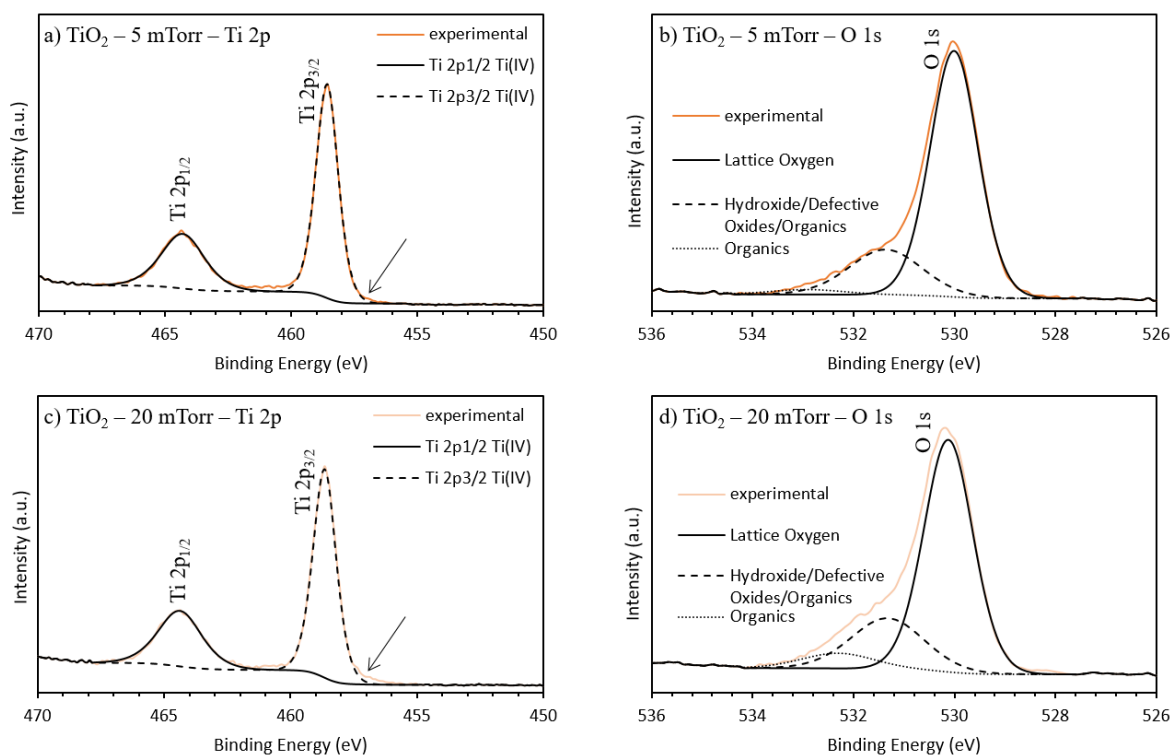


Figure 5: Deconvoluted high-resolution XPS spectra of the a) Ti 2p and b) O 1s peaks of TiO₂ deposited at 5 mTorr O₂ compared to the c) Ti 2p and d) O 1s peaks of TiO₂ deposited at 20 mTorr O₂.

Deconvolution of the O 1s spectra in Figure 5 b) and d) can elucidate the origins of oxygen contained in the TiO₂ films. The main peak at 530.1 eV is attributed to lattice oxygen in TiO₂. The asymmetry of the peak or the presence of a shoulder on the higher binding energy side of the peak indicates the presence of: (1) non-lattice oxygen arising from the formation of oxygen vacancies, or; (2) loosely adsorbed O₂ and oxygenated species such as H₂O and CO₂ arising from surface contamination and defects [88]. While the presence of a prominent shoulder is undeniable, given that the surface of the films was not plasma-cleaned prior to XPS analysis, it is impossible to differentiate its attribution to oxygen vacancies or surface contamination. As such, an increase in the concentration of oxygen vacancies with decreasing oxygen pressure cannot be ascertained.

Figure 6 gives the full spectrum XPS survey scans of the ZnO films deposited by PLD at 5 and 20 mTorr O₂. Only O, Zn, C and N elements were detected, confirming the growth

of the expected materials since all identified peaks (with the exception of the C 1s and N1s peaks, which appear as a result of surface contamination) are attributed to ZnO. High resolution scans for Zn and O were also performed, as shown in Figure 7. The Zn 2p_{3/2} peak at 1021.2 eV is characteristic of Zn²⁺ ions and has a constant binding energy regardless of oxygen pressure [89]. Moreover, the high degree of symmetry exhibited by the Zn 2p_{3/2} peak (i.e., no shoulders) indicates that Zn²⁺ is the only valence state of Zn present [90].

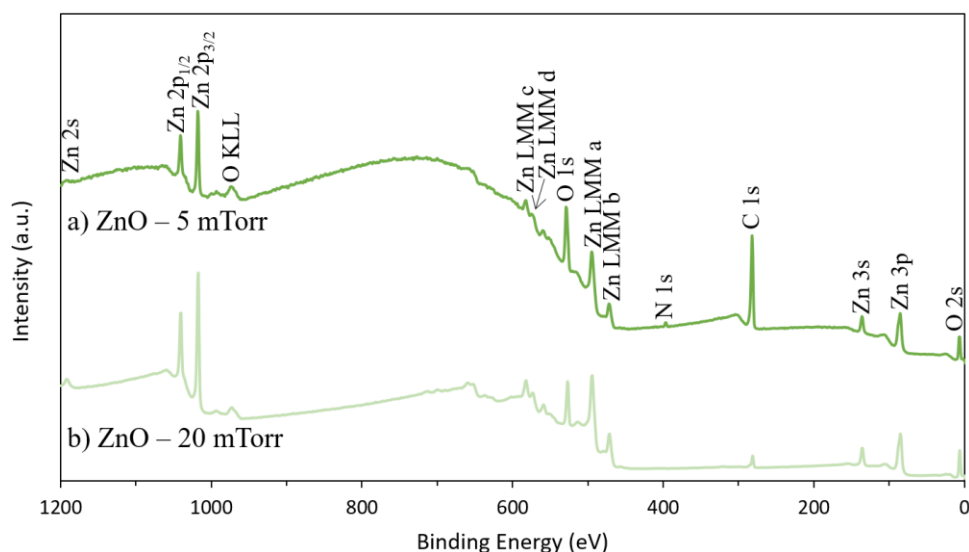


Figure 6: XPS spectra of the ZnO thin film samples deposited by PLD at a) 5 mTorr and b) 20 mTorr O₂.

As with the TiO₂ films, the deconvoluted O 1s spectra are used to understand the origins of oxygen in the ZnO film. The main O 1s peak at 530.1 eV is attributed to O²⁻ ions in the fully-oxidized Zn wurtzite structure, wherein Zn atoms have six nearest neighbor O²⁻ ions. The shoulder that broadens the high binding energy side of the main O 1s peak is ascribed to: (1) O²⁻ ions located in oxygen-deficient regions of the Zn lattice (i.e., where Zn atoms have fewer than six nearest neighbor O²⁻ ions), and (2) oxygenated surface contamination [90]. While the O 1s shoulder appears significantly larger in the ZnO thin film deposited at 5 mTorr O₂, than at 20 mTorr O₂, this is primarily due to an increased amount of organic surface contaminants. Furthermore, the present XPS analysis does not permit distinguishing oxygen vacancies from oxygen-based contaminants. Nonetheless, the

literature affirms that ZnO films grown in low-oxygen environments have increased concentrations of oxygen vacancies [77].

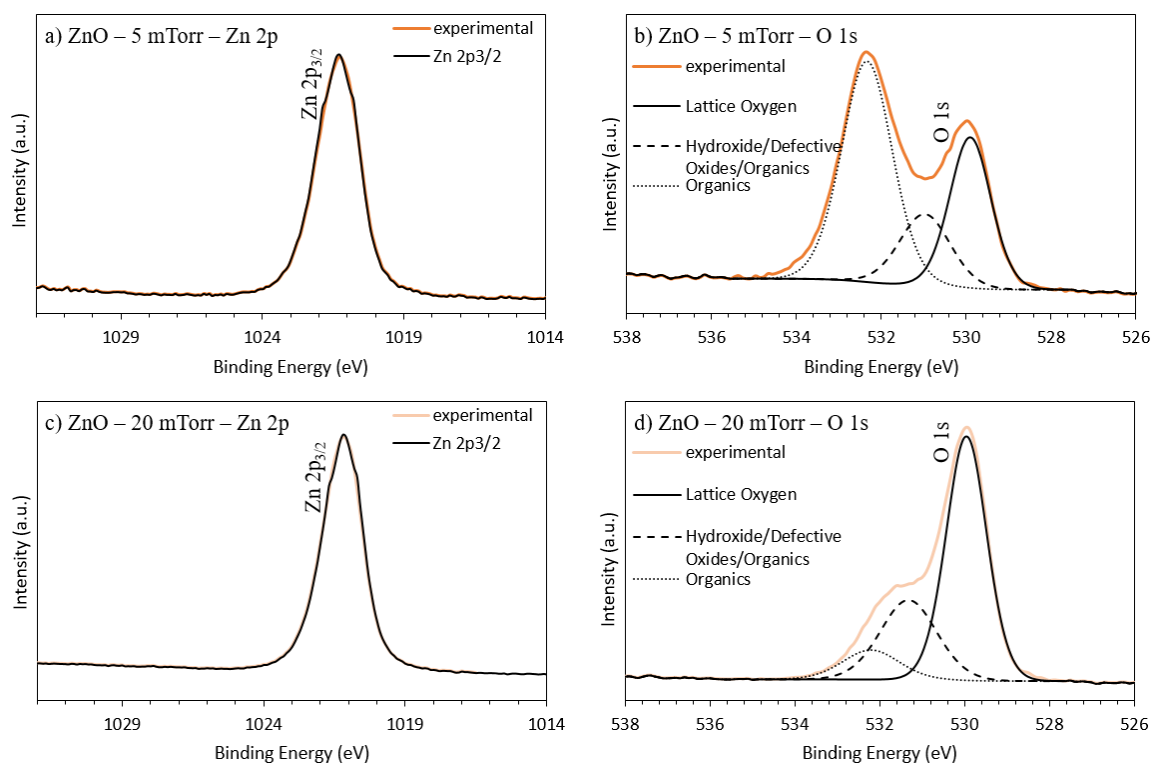


Figure 7: Deconvoluted high-resolution XPS spectra of the a) Zn 2p and b) O 1s peaks of ZnO deposited at 5 mTorr O₂ compared to the c) Zn 2p and d) O 1s peaks of ZnO deposited at 20 mTorr O₂.

The XPS survey scans for the AZO thin films grown at 5 and 20 mTorr are given in Figure 8. As expected, the spectra are very similar to those of ZnO in Figure 6. All of the same peaks indicative of ZnO film formation appear in the AZO survey scan, with the exception of one additional Al 2p peak at 73.7 eV which can be attributed to the Al doping. Due to the low Al doping %, this peak is not easily discerned at the presented survey scan magnification. A high resolution scan of the distinguishing Al 2p peak is shown in Figure 9 a) and c). The intensity of the Al 2p is small in comparison to the characteristic Zn 2p peaks due to the fact that ZnO was doped with only 2% Al. Furthermore, the intensity of the Al 2p peak is the same at both 5 and 20 mTorr O₂. Therefore, at the given magnitudes,

oxygen pressure does not measurably affect the uptake of Al by the ZnO lattice. Atomic composition analyses found that in both films, the atomic percentage of Al was 0.7%.

The high-resolution O 1s spectra for AZO at 5 and 20 mTorr O₂ were also taken to assess for the presence of oxygen vacancies with decreasing pressure. The O 1s peak is deconvoluted in the same way as ZnO, where the high binding energy shoulder is indicative of surface contaminants and oxygen deficient regions in the metal oxide framework.

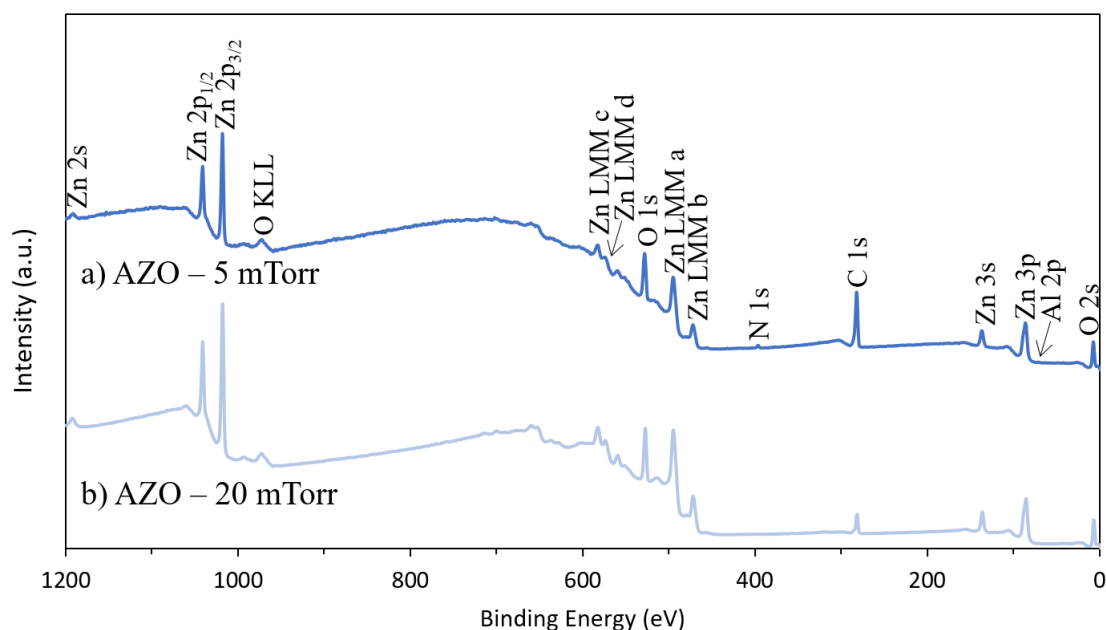


Figure 8: XPS spectra of the AZO thin film samples deposited by PLD at a) 5 mTorr and b) 20 mTorr O₂.

The O 1s shoulder in Figure 9 b), corresponding to the 5 mTorr condition is significantly more prominent than its 20 mTorr counterpart. While this may point to an increased formation of oxygen vacancies at low oxygen pressure, in the absence of surface cleaning prior to XPS analysis, the results remain inconclusive. However, since oxygenated surface contaminants are unlikely to diffuse to the XPS probing depth (7 – 10 nm), oxygen deficiencies are assumed to be principally responsible for the variations in O 1s shoulder size. Furthermore, studies of AZO depositions at similar oxygen pressures have confirmed that larger concentrations of oxygen vacancies are formed for this magnitude of decreasing

oxygen pressure [74]. Interestingly, the substantial difference in the size of the O 1s shoulder demonstrates an increased sensitivity to oxygen pressure of ZnO with Al-doping.

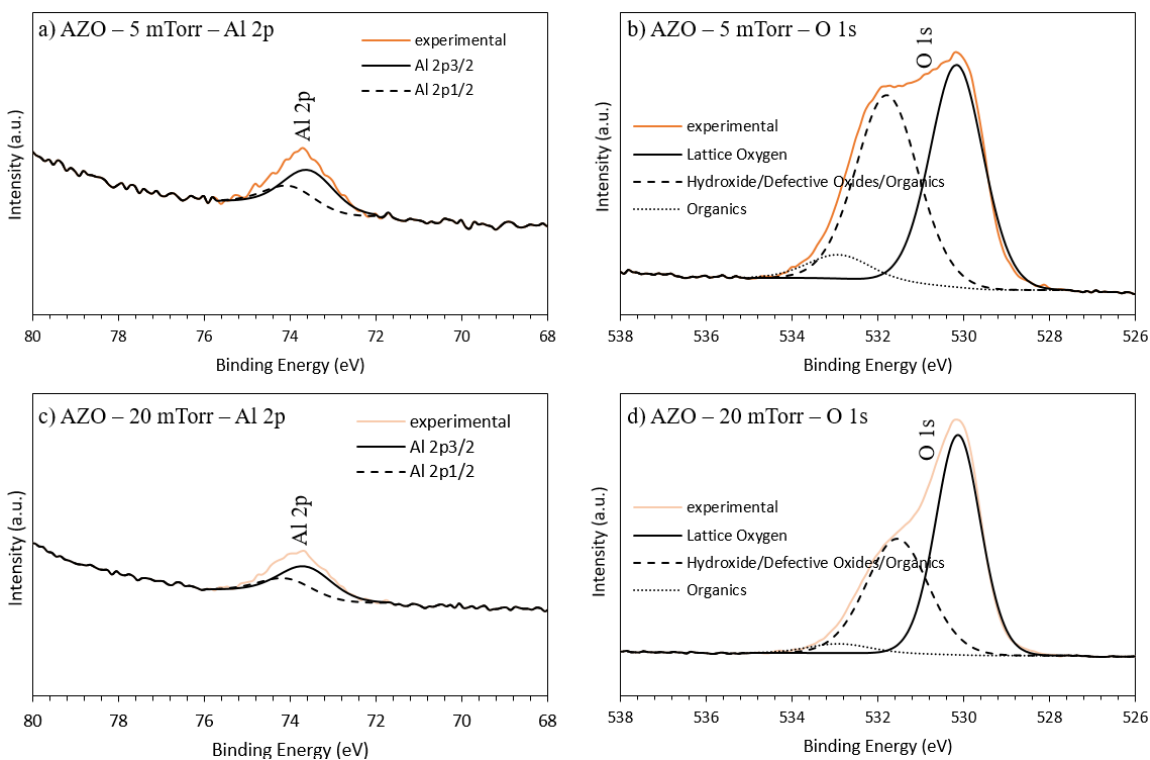


Figure 9: Deconvoluted high-resolution XPS spectra of the a) Al 2p and b) O 1s peaks of AZO deposited at 5 mTorr O₂ compared to the c) Zn 2p and d) O 1s peaks of AZO deposited at 20 mTorr O₂.

Oxygen vacancies can have significant influence on the bandgap and absorptive behaviour of metal oxide thin films, thereby affecting their ability to protect perovskites from degradation-inducing UV light. Therefore, the analysis of optical properties given in Chapter 4 will provide further insight into the relationship between oxygen pressure during film growth and the formation of oxygen vacancies.

3.4 Thin Film Morphology

Room temperature physical vapour depositions are advantageous in that no energy input is required for heating. However, in the absence of heating, impinging atoms may have insufficient energy to arrange themselves into crystal structures with long-range order.

Pulsed laser depositions, in particular, are capable of producing crystalline films at lower temperature than alternative techniques because the plasma generated by the laser yields highly energetic impinging atoms [47]. To verify the structure-type obtained by the pulsed laser depositions, 200 nm thin film samples of TiO₂, ZnO and AZO, deposited at 5 mTorr O₂ on silicon wafers, were analyzed by X-ray diffraction (XRD) using a Rigaku SmartLab system with CuK_α radiation ($\lambda=1.54056 \text{ \AA}$) and a glancing incident angle of 1°. The XRD patterns of the TiO₂, ZnO and AZO films grown by room temperature PLD in 5 mTorr O₂ are given in Figure 10.

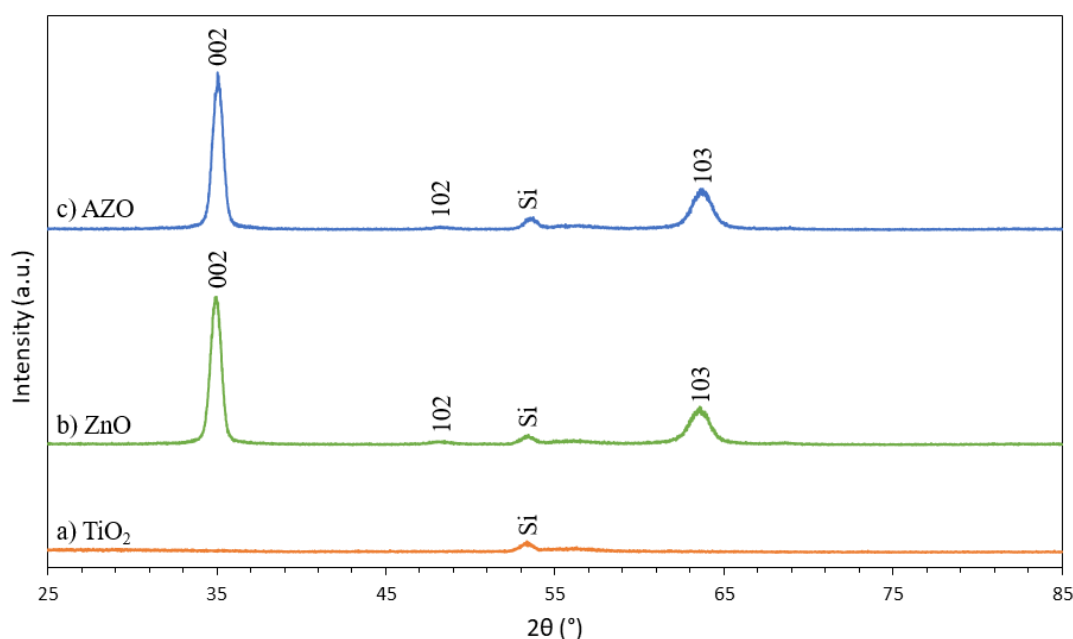


Figure 10: XRD patterns of a) TiO₂, b) ZnO, and c) AZO thin films deposited by room-temperature PLD in 5 mTorr O₂.

For TiO₂, room temperature deposition is expected to yield amorphous thin films, regardless of the oxygen pressure. It is only at high deposition temperatures above ~300 – 500°C that the anatase and rutile crystal phases emerge [67, 68]. From Figure 10 a), it is evident that an amorphous TiO₂ film was obtained since there are no visible diffraction peaks. The single low-intensity peak at 53.4° corresponds to a diffraction peak of the p-type silicon (100) substrate, and also appears in the Figure 10 b) and c) spectra of ZnO and AZO. For ZnO and AZO, both amorphous and crystalline films can be grown with room-

temperature pulsed laser depositions. Among many factors, the crystallinity of the room-temperature grown film depends on the PLD laser energy [71], oxygen pressure [91, 76], substrate material [69] and % Al doping [65]. Based on the presence of the (002), (102), and (103) orientation peaks at 35.0°, 48.2° and 63.7°, respectively, it is clear that the ZnO and AZO films are not amorphous. These planes correspond to the ZnO hexagonal wurtzite crystal structure (JCPDS # 36-1457) [92]. However, given the intensity of the characteristic peaks, the crystallites are small. Similar room-temperature PLD depositions also found weak ZnO/AZO crystallinity; these experiments reported increasing peak intensity with decreasing oxygen pressure, and the (103) plane only emerged below 22 mTorr O₂ [91]. Additionally, there are no Al or Al₂O₃ diffraction peaks in Figure 10 c) for AZO because the Al doping percentage is very low and the Al dopant atoms are substitutional in that they replace Zn atoms in the crystal lattice [71].

The Scherrer equation was used to determine the average grain size (D) based on the FWHM peak broadening (β):

$$D = \frac{0.9\lambda}{\beta \cos\theta} \quad (1)$$

where $\lambda = 1.54056 \text{ \AA}$ is the wavelength of the CuK $_{\alpha}$ X-ray and θ is the diffraction angle. The average grain sizes of the ZnO and AZO crystallites are given in Table 5. Measurement uncertainties were calculated based on being able to discern diffraction angles to a precision of $\pm 0.01^\circ$ (i.e., half the measurement resolution). The size of the crystal was found to be independent of Al doping: both ZnO and AZO have small crystallite sizes of approximately 13 nm. Further, the (002) and (103) ZnO orientations produced congruent grain sizes, given the uncertainty in the calculation.

Table 5: Average grain size of ZnO and AZO crystals grown by room temperature PLD in 5 mTorr O₂.

	Crystal Plane	D (nm)
ZnO	(002)	13.10 \pm 1.25
	(103)	12.66 \pm 1.27
AZO	(002)	12.94 \pm 1.22
	(103)	12.42 \pm 1.22

Field emission scanning electron microscopy (FESEM) was performed using a Hitachi SU8230 Regulus ultra-high resolution microscope with accelerating voltages ranging from 3 to 20 kV to image the surface of the thin film samples. Before imaging, the samples were coated with a thin layer of chromium to minimize charging artifacts. To compare the effect of oxygen pressure on film density and grain size, FESEM images of each material deposited at 5 and 20 mTorr O₂ are given in Figure 11.

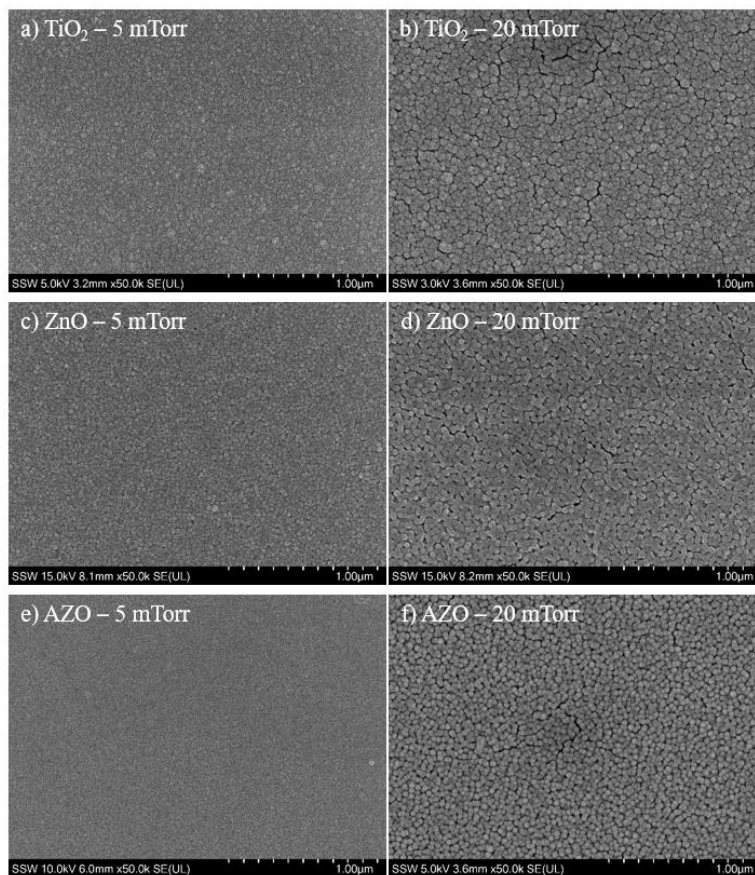


Figure 11: FESEM images of pulsed laser deposited: TiO₂ in a) 5, and b) 20 mTorr O₂; ZnO in c) 5 and, d) 20 mTorr O₂, and; AZO in e) 5, and f) 20 mTorr O₂.

The FESEM images demonstrate evenly distributed particulate microstructures, owing to the uniformity of the PLD method. In all cases, the materials are significantly denser and have more refined microstructures at lower oxygen pressure. Generally, in physical vapour deposition, density increases with decreasing deposition pressure due to a reduction in the

number of collisions between vapourized target atoms and residual or reactive gases, resulting in high target atom kinetic energy upon impingement [67].

All films have morphologies consisting of distinct particulate regions, refined to varying degrees depending on the material and oxygen pressure. For instance, the ZnO film deposited at 5 mTorr has particles – or agglomerated clusters of grains – with diameters of approximately 300 nm. Based on the grain sizes determined by XRD, each particle contains ~ 23 grains. At 20 mTorr O₂, the ZnO particle size increases by more than 50% to approximately 500 nm. Moreover, with Al doping at 5 mTorr O₂, the ZnO microstructure is refined such that the diameter of particles cannot be discerned at the given magnification. When oxygen pressure is increased to 20 mTorr, the AZO particle size increases to ~ 350 nm, but remains more refined than its ZnO counterpart at 20 mTorr. Given the amorphous nature of the TiO₂ thin films, it is more difficult to determine the size of particles. Nonetheless, in keeping with the relationship between oxygen pressure and density, the TiO₂ microstructure is significantly more refined at 5 mTorr than at 20 mTorr.

The pinholes and interparticle gaps present in the 20 mTorr films provide detrimental pathways for water and oxygen permeation. Since the WVTR and OTR of an encapsulant are proportional to its molecular packing density, thin films deposited at low oxygen pressure are more suitable for preventing water- and oxygen- induced degradation of perovskites. However, since the focus of this work is the prevention of photodegradation, the optical performance of the thin films is prioritized over their densities. Nonetheless, pinholes may also constitute micro-regions of high UV-light transmittance, with similar repercussions to photostability.

3.5 Thin Film Uniformity

Optical properties of thin films are highly dependent on thickness. As a result, the uniformity in thickness of the large-area PLD technique was evaluated to assess whether the absorption/transmittance of thin films has a radial variation that might affect encapsulation performance. Using the experimental methodology described in Section 3.1, approximately 50 – 100 nm of TiO₂, ZnO or AZO was deposited by PLD on silicon wafers with 3 in. diameter. The thickness was then measured by curve fitting interference

reflectometry (Scientific Computing International (SCI), FilmTek 2000) data in the 250 – 850 nm wavelength range using SCI’s generalized Lorentz oscillator model. Nine thickness measurements were taken for each silicon wafer at varying radial and angular positions, as indicated by the marked probing locations (‘x’) in Figure 12.

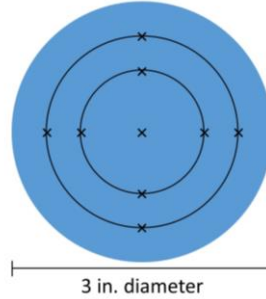


Figure 12: Scaled schematic of a 3 in. silicon wafer, indicating the reflectance spectrophotometry probing locations (‘x’).

The mean film thicknesses for each deposition condition are given in Table 6. Herein, error is quantified as: (i) a curve-fitting error, given by the root mean square error (RMSE), and; (ii) the 95% confidence interval around the mean (σ), given by the plus/minus (\pm) error in thickness and RMSE, and determined according to:

$$\sigma = t_{\alpha/2} \frac{s}{\sqrt{n}} \quad (1)$$

where s is the sample standard deviation, n is the number of samples and $t_{\alpha/2}$ is the value of the Student’s t -distribution at a confidence interval of 95% (i.e., for $\alpha/2 = 0.025$ and $n = 9$, $t = 2.306$). Unless otherwise stated, all \pm errors and uncertainties presented hereafter were also calculated according to Equation (1), and propagated, as necessary.

The uniformity of the thin film is captured in the mean thickness confidence interval. High \pm errors indicate large variations in thickness across the probed locations, while small \pm errors represent highly uniform thickness across the entire $\frac{\pi}{4}(3 \text{ in.})^2$ deposition area. Since the \pm error on thickness is less than 3.5 nm for all depositions, the PLD technique is considered to produce highly uniform thin films and the effect of spatial variation on variability in optical properties is considered near negligible.

Table 6: Mean thickness, curve-fitting RMSE and scatter index of TiO₂, ZnO and AZO thin films deposited by PLD at 2, 5 and 20 mTorr O₂.

Material	P_{O_2} (mTorr)	Mean Thickness (nm)	Mean RMSE	Scatter Index (%)
TiO ₂	2	55.68 ± 0.83	0.36 ± 0.02	2.02 ± 0.10
	5	58.68 ± 1.06	0.43 ± 0.01	2.58 ± 0.06
	20	60.69 ± 3.46	0.64 ± 0.03	3.95 ± 0.24
ZnO	2	88.32 ± 2.17	0.46 ± 0.04	3.63 ± 0.34
	5	86.55 ± 2.32	0.45 ± 0.05	3.60 ± 0.37
	20	96.95 ± 3.22	0.54 ± 0.06	3.60 ± 0.39
AZO	2	87.15 ± 1.24	0.46 ± 0.04	3.41 ± 0.26
	5	88.48 ± 1.41	0.42 ± 0.05	3.16 ± 0.37
	20	71.72 ± 1.03	0.30 ± 0.01	2.36 ± 0.07

In order to gauge the efficacy of the model used to determine thickness, it is necessary to normalize the RMSE values. This is given by the scatter index in Table 6, which is calculated as the quotient of the mean RMSE and the mean observed reflectance. Since all scatter indices are less than 5%, the model is said to accurately predict the measured values and the thicknesses are deemed reliable.

A final assessment of uniformity is given in the form of a visualization of the spatial gradation in thickness across the 3 in. diameter silicon wafer. Each plot in Figure 13 provides a colour map of thickness as a function of position on the silicon wafer, where red and blue colours represent the thickest and thinnest points, respectively.

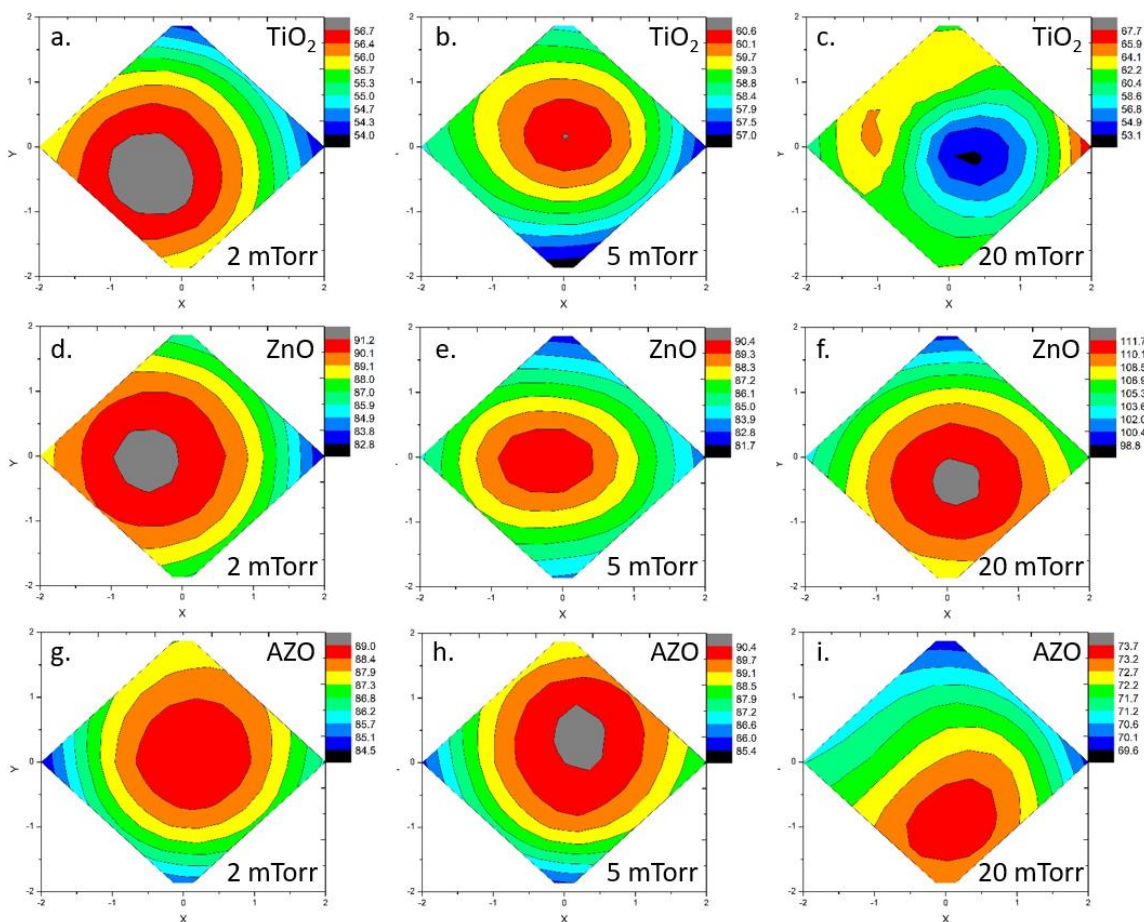


Figure 13: Visualization of the thickness of (a, b, c) TiO₂, (d, e, f) ZnO and (g, h, i) AZO thin films deposited by PLD at (a, d, g) 2, (b, e, h) 5 and (c, f, i) 20 mTorr O₂ across the 3 in. diameter silicon wafer.

While the difference between the minimum and maximum thicknesses is small across all deposition conditions, the films are consistently thickest at the center of the substrate. This is consistent with any deposition technique where material is vapourized in the form of a plume and condenses on the substrate: the concentration of material at the center of the plume is greater than at the edges of the plume [93]. However, in a case such as this, where a laser rastering program was used in order to coat large surface-area substrates, uniformity and the distribution of thickness across the substrate are highly dependent on the program script [94]. In fact, the minimal difference in magnitude between thickness at the center and edges of the substrate is indicative of a well-optimized laser rastering program. Figure 13 demonstrates that the given laser scanning parameters generally produce films with

radially decreasing thickness. Figure 13 c), which represents TiO₂ deposited in 20 mTorr O₂, is the only exception to the aforementioned rule. Here, thickness at the edge is greater than at the center, and thickness does not change linearly with radial position. Variations in uniformity across depositions exist because the rastering program was optimized to produce uniform coatings given a specific plume geometry. However, since the angular distribution of ablated material and the shape of the plasma plume depend on the target material and the ambient gas environment, differences in uniformity are expected for depositions of different materials in different oxygen gas environments [95]. Therefore, it is likely that a combination of the plume broadening effect [95] of depositing under high oxygen partial pressure and the use of TiO₂ as the ablation material accounts for the observed discrepancy in Figure 13 c). Other errors from extraneous variables such as the deposition atmosphere or the presence of impurities are deemed negligible since the depositions are carried out in a very controlled chamber environment with low base pressures ($\sim 10^{-7}$ Torr).

Based upon the presented analysis, a deposition rate for each of the deposition conditions was determined in order to inform the appropriate deposition time to produce the same UV-protective films, but with thicknesses of 200 nm for comparison of optical properties and perovskite photoprotection.

3.6 Conclusions

A detailed account of the apparatus and methodology used to deposit TiO₂, ZnO and AZO thin films by pulsed laser deposition was given. In particular, thin films 200 nm in thickness were deposited at room-temperature in varying oxygen partial pressure environments. The effect of oxygen pressure on the appearance, chemical composition and morphology of the films was investigated. It was found that all target materials produced transparent coatings but that those deposited at high O₂ pressure tended to be more colourless. Additionally, 200 nm thin films of TiO₂ were generally more tinted than ZnO and AZO films of the same thickness. XPS analysis confirmed that the pulsed laser deposited films had the expected chemical compositions corresponding to the target material from which they were ablated. Furthermore, high resolution XPS scans of the Ti 2p peak in TiO₂ revealed the formation

of Ti^{3+} ions, which are typically associated with oxygen vacancies and low- O_2 growth environments. While the same XPS spectra were unable to ascertain the presence of oxygen vacancies in the ZnO and AZO films, references from the literature were able to provide a basis for their presumed existence. It is expected that the concentration of oxygen vacancies in TiO_2 , ZnO and AZO will increase slightly with decreasing oxygen pressure and have important implications on optical properties. Moreover, deposition at room temperature was found to have significant influence on the molecular order obtained for each material, as determined by XRD: ZnO and AZO films were crystalline in nature, while TiO_2 was amorphous. FESEM provided a visualization of the particulate microstructure obtained for all films, and substantiated a strong inverse relationship between molecular density and oxygen pressure. Finally, an assessment of the uniformity of the PLD technique was conducted by using reflectance spectrophotometry to measure the thin film thickness at nine positions across a 3 in. substrate. The thickness varied radially by only approximately 3 nm, and as such the high degree of uniformity of the PLD method was validated.

Chapter 4

4 Optical Properties

The Sun supplies a large amount of energy to the Earth in the form of solar radiation. Depending on the wavelength of light emitted, the solar irradiance is classified as ultraviolet (UV, 200 nm – 400 nm), visible (400 nm – 750 nm), or infrared (750 nm – 1 mm). UV light is of particular interest because it has the shortest wavelength and is thereby the most energetic form of solar radiation. Due to the large amount of energy contained in photons emitted in the UV region, this light is capable of catalyzing degradation in organic compounds, such as MA-based perovskites. The UV spectrum is further divided into three emission regions: (1) UV-C light (200 nm – 260 nm); (2) UV-B light (260 nm – 315 nm), and; (3) UV-A light (315 nm – 400 nm). While UV-C light is the most energetic, virtually none of it reaches the Earth, because it is absorbed by oxygen in the atmosphere to create the ozone layer. Depending upon cloud coverage, a large portion of UV-B light is also absorbed by Earth's atmosphere. However, UV-A light is capable of passing through the atmosphere unaffected. Therefore, the longest wavelength and least energetic form of UV light – UV-A light – is actually the principal source of UV-induced degradation on Earth's surface.

Organic-inorganic lead halide perovskites have bandgaps from 1.55 to 1.6 eV [96]. Using spectroscopic ellipsometry, Lin et al. determined the extinction coefficient for MAPbI₃ as a function of wavelength and found that three distinct spectral regions exist: (1) at $\lambda > 800$ nm there is minimal absorption; (2) at $500 \text{ nm} < \lambda < 800 \text{ nm}$ there is moderate absorption, and; (3) at $\lambda < 500$ nm there is very strong absorption [97]. This moderate-to-strong absorption through the visible range is in alignment with the maximum solar radiation intensity (400 nm – 700 nm), making perovskites ideal absorber materials in solar cells. However, it also means they will absorb UV-light and are susceptible to photodegradation.

Thin film encapsulants for perovskite solar cells should demonstrate simultaneous strong UV light absorption or reflection and high visible light transmittance to prevent photodegradation without sacrificing device efficiency. Herein, the optical performance of the TiO₂, ZnO and AZO coatings deposited by PLD at room temperature in 2, 5 and 20

mTorr of oxygen is studied extensively in order to draw conclusions regarding the most suitable candidate materials for perovskite photoprotection.

4.1 Extinction Coefficients and Refractive Indices

Extinction coefficients (k) and refractive indices (n) are thickness-independent intrinsic material properties and constitute two of the most important properties used to understand how a thin film interacts with light. The extinction coefficient quantifies the propensity of a material to absorb light of a given wavelength, and dictates how thick a material must be to achieve complete absorption. In contrast, the refractive index is a measure of the degree to which the incident angle of light at a particular wavelength changes as it passes through a material. Typically, the refractive index increases with density in thin films [98]. For a photoprotection application, high n , high k at UV wavelengths, and near-zero k at visible wavelengths are preferred in order to produce dense films with low WVTR/OTR that have strong UV-light absorption and almost no visible light absorption. The extinction coefficients and refractive indices of the TiO₂, ZnO and AZO films were determined by interference reflectometry, according to the same procedure used to measure thin film thickness in Section 3.5. The same reflectance measurements taken at nine locations across each silicon wafer were used to fit the Lorentz oscillator model to obtain the extinction coefficients and refractive indices. As a result, the RMSEs reported for each deposition condition in Table 6 also pertain to this analysis.

The refractive indices of the TiO₂, ZnO and AZO thin films deposited by PLD at 2, 5 and 20 mTorr O₂ are given in Figure 14. In order to provide a straightforward comparison across deposition conditions, the refractive index at 368 nm – a wavelength of UV-A light that is used in Chapter 6 for irradiating perovskite samples – is plotted. TiO₂ has the highest refractive index of the materials studied, decreasing from 3.00 ± 0.01 at 2 mTorr O₂ to 2.45 ± 0.14 at 20 mTorr O₂. The magnitudes and relationship to oxygen pressure of the TiO₂ refractive indices are in very good agreement with those reported in the literature for similar PLD deposition conditions [67]. Due to the sensitivity of its microstructure to oxygen vacancies, TiO₂ also displays the largest variation in refractive indices with O₂ deposition pressure. The refractive indices of ZnO and AZO also decrease with O₂

pressure, but not as substantially. At their highest (i.e., at 2 mTorr O₂), the refractive indices of ZnO and AZO are 2.26 ± 0.02 and 2.25 ± 0.003 , respectively. ZnO and AZO exhibit similar refractive indices across all oxygen pressures due to the low Al doping % employed, however a slight decrease in n with Al doping may be ascertained. Both the magnitudes and the effect of Al-doping on the refractive index are consistent with those reported in the literature [65, 66].

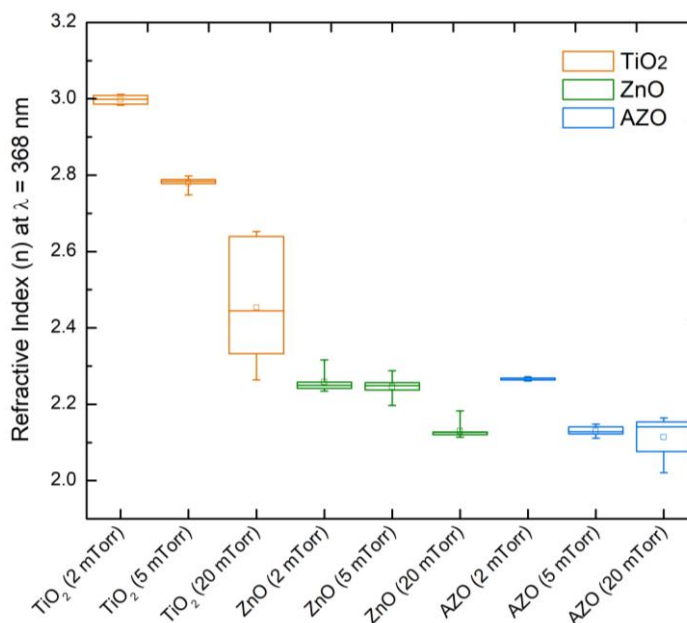


Figure 14: Refractive indices at $\lambda = 368$ nm of TiO₂, ZnO and AZO thin films deposited by PLD at 2, 5 and 20 mTorr O₂.

It should be noted that in general, the longest whiskers, and thereby the largest spreads in the data, correspond to materials deposited at high oxygen pressure. This is due to the inhomogeneous nature of films which are grown under large O₂ concentrations, and the difficulty that arises with fitting the Lorentz oscillator model to inhomogeneous films.

The refractive indices are also in good agreement with the film porosities, as given by the FESEM images in Section 3.4. TiO₂, which has the highest refractive index, produces the densest films; the ZnO and AZO thin films, which had similar refractive indices, also have similar packing densities. Moreover, the relationship between density, refractive index and

oxygen pressure, is very clear: for all materials, as the oxygen pressure is increased, the porosity increases and the refractive index decreases.

The absorption behavior of a thin film is central in evaluating its suitability for PSC photoprotection. Two important wavelengths must therefore be considered in the analysis of extinction coefficients. The first is $\lambda = 368$ nm, which corresponds to a wavelength of UV-A light at which perovskite samples are degraded in Chapter 6. The second is the onset of the visible light spectrum, $\lambda = 400$ nm, where absorption should be minimized to prevent PCE losses in solar cells. Figure 15 provides a comparison of the extinction coefficients at each of these wavelengths for TiO₂, ZnO and AZO thin films deposited by PLD at 2, 5 and 20 mTorr O₂.

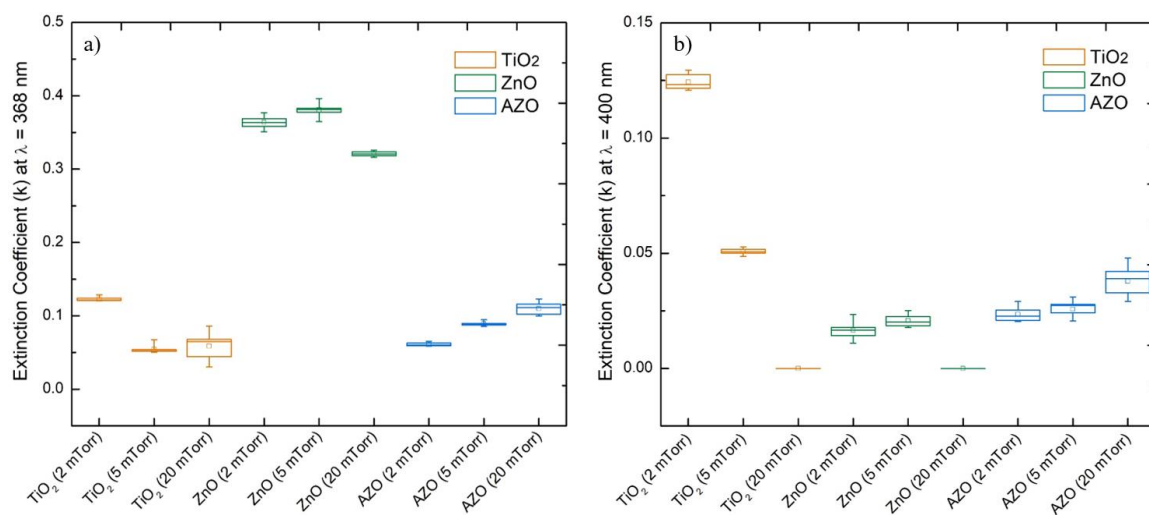


Figure 15: Extinction coefficients at a) $\lambda = 368$ nm and b) $\lambda = 400$ nm of TiO₂, ZnO and AZO thin films deposited by PLD at 2, 5 and 20 mTorr O₂.

Across all oxygen pressures, ZnO has much larger UV light extinction coefficients than either TiO₂ or AZO. For example, at 2 mTorr O₂, the $\lambda = 368$ nm extinction coefficients of TiO₂, ZnO and AZO are 0.12 ± 0.002 , 0.36 ± 0.007 , and 0.061 ± 0.002 , respectively. This indicates that for films of the same thickness, ZnO will absorb the most UV 368 nm light. Nonetheless, ZnO remains remarkably transparent to visible light with k as high as only 0.021 ± 0.002 at $\lambda = 400$. In fact, with the exception of only the 2 mTorr TiO₂, all of the films have relatively low extinction coefficients through at the onset of the visible

range. Furthermore, distinct relationships between the PLD oxygen pressure and absorption of each material are revealed. For TiO₂ and ZnO, absorption at $\lambda = 368$ nm and $\lambda = 400$ nm decreases with increasing oxygen deposition pressure. Conversely, the opposite relationship is true of AZO: here, an increase in extinction coefficients is associated with increasing O₂ deposition pressure. These phenomena are further uncovered and explained in the ensuing section. Overall, based upon the analysis of extinction coefficients and due to its superior propensity for UV light absorption, ZnO should provide the best protection against UV degradation without sacrificing visible light transmittance.

4.2 Transmittance, Reflectance and Absorptance

While the extinction coefficients provide a theoretical estimation of the intrinsic absorption behavior of the thin film materials, optical transmittance and reflectance measurements are taken to provide a holistic understanding of the true nature of the light-matter interaction. These measurements will combine the intrinsic absorptive properties of the materials with the effects of film thickness and inhomogeneities (defects, pores, nonuniformities, etc.). In particular, the percentage of light transmitted through a thin film is strongly dependent on the thickness of the film; according to the Beer-Lambert law, absorbance is directly proportional to the length of the optical path [99]. Therefore, in this comparative analysis of the optical properties of TiO₂, ZnO and AZO thin films, a constant material thickness of 200 nm was used across all samples (the of uniformity of which was previously discussed in Section 3.5). Additionally, the thin films were deposited on quartz substrates for the purpose of taking transmittance and reflectance measurements because quartz has near-zero absorption and reflection of UV, visible (Vis) and near-infrared (NIR) light, which will permit high resolution measurements with limited noise.

4.2.1 Experimental

Optical transmittance measurements were taken using an Ocean Insight Flame UV-Vis and NIRQuest spectrometers that detect wavelengths in the range of 250 – 850 nm and 850 – 2150 nm, respectively. To acquire a transmittance spectrum, the coated quartz sample is placed on a support between UV-Vis or NIR Ocean Insight optical fibers (model QP115-025-XSR or QP600-2-VIS-NIR) with core sizes of 115 μm and 600 μm , respectively. In

the case of UV-Vis measurements, the top fiber is connected to a SCI FilmTek light source which outputs light from 190 to 1100 nm using a combination of halogen and deuterium lamps. Conversely for NIR measurements, an Ocean Insight tungsten halogen light source (HL-2000-FHSA) which irradiates at 360 nm to 2.4 μm is used. The light is transmitted through the top optical fiber and illuminates the quartz sample. A second optical fiber positioned under the black support sends light transmitted through the sample to the appropriate spectrometer for detection. OceanView software is then used to process and analyze the transmittance data. In all transmittance measurements, quartz was used as a reference, thereby eliminating the influence of the substrate on the results.

Reflectance data was acquired across the UV-Vis-NIR spectrum using the same apparatus, however reflectance optical fibers (models R200-7-UV-VIS and R200-7-VIS-NIR) were used. These fibers have one probing terminal and two linking terminals which are connected to the light source and spectrometer, respectively. In this way, light from the light source illuminates the coated quartz sample through the probing fiber, which is positioned vertically above the sample. Any reflected light is captured by the same probing fiber positioned vertically overhead, however the optical pathway splits such that the reflected light is transmitted to the spectrometer for detection. The position of the probing fiber was optimized to a distance of 10.25 mm above the surface of the sample to maximize the intensity of reflected light. For all reflectance measurements, a $> 95\%$ reflectance aluminum mirror specular reflectance standard was used as a reference (Ocean Optics, model STAN-SSH). As pictured in the scaled schematic in Figure 16, three transmittance/reflectance measurements (diagonally: left, right and center) were taken for each sample to estimate the variability due to non-uniformities in the coating.



Figure 16: Scaled schematic of a 1 x 1 in. quartz substrate, indicating the spectroscopy probing locations ('x').

Additionally, each deposition condition was applied across a minimum of four quartz substrates. The uncertainties reported herein are therefore a reflection of the difference in experimental spectroscopy results obtained across all samples of a given deposition condition and across the three probing locations for each sample.

4.2.2 Results and Discussion

The UV to visible light transmittance spectra of TiO₂, ZnO and AZO thin films deposited at oxygen partial pressures from 0 to 20 mTorr are given in Figure 17. For each spectrum, the plotted transmittance is obtained from the center position of a representative coated quartz substrate.

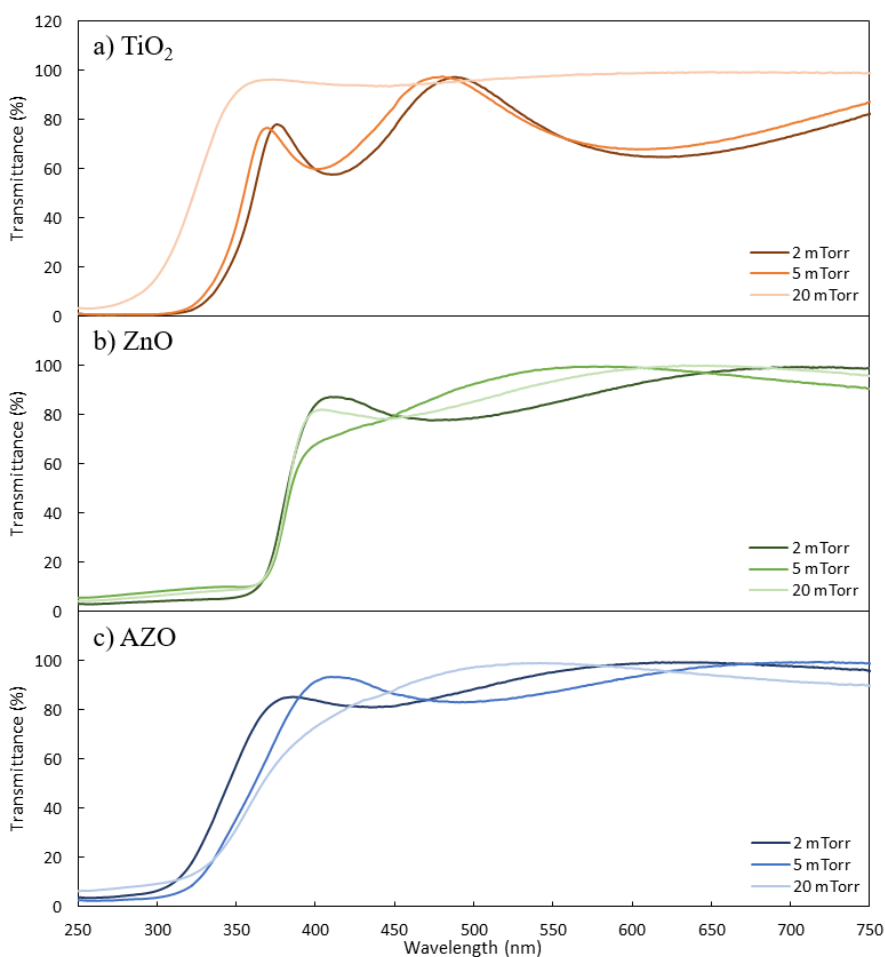


Figure 17: UV-Visible light transmittance spectra of a) TiO₂, b) ZnO, and c) AZO coatings deposited by PLD at oxygen partial pressures of 0, 2 and 20 mTorr.

The transmittance spectra provide evidence of the distinct responses of each thin film material to changes in oxygen pressure during pulsed laser deposition. TiO₂ thin films exhibit a very pronounced redshift in their absorption edge with decreasing O₂ pressure: at 20 mTorr O₂, the absorption edge is located at 342 ± 4 nm, while at 2 mTorr O₂, it is located at 368 ± 4 nm. This relationship between oxygen pressure and TiO₂ absorption is well documented in the literature. In general, the introduction of donor states within the bandgap of a semiconductor will reduce the incident photon energy required to yield absorption [100]. In the case of the pulsed laser deposited TiO₂ thin films, the oxygen vacancies and Ti³⁺ interstitials formed in low-oxygen pressure growth environments are intrinsic defects that give rise to unpaired electrons [101]. As a result of a surplus in mobile donor species, an intermediary donor level/defect state (i.e., a level between the valence and conduction bands) is generated just below the conduction band [101, 102]. Free electrons in the donor level require significantly less energy to be promoted into the conduction band, so the bandgap is said to have narrowed. In other words, depositing TiO₂ under low oxygen pressures is akin to “self-doping” the TiO₂, due to the formation of oxygen vacancies and Ti³⁺ species, which contribute to narrowing the bandgap and redshifting the absorption edge [68].

The strong dependence of the TiO₂ UV-light transmittance on oxygen pressure illustrated in Figure 17 a) is particularly interesting given the XPS analysis in Section 3.3, which found an unappreciable increase in the Ti³⁺ shoulder for TiO₂ deposited at 2 mTorr compared to 20 mTorr (Figure 5 a) and c)). The result points to the extreme sensitivity of the TiO₂ bandgap to changes in oxygen pressure during deposition.

Additionally, as oxygen pressure is reduced, TiO₂ transmittance through the visible range decreases significantly. For example, at 20 mTorr O₂, TiO₂ transmittance does not fall below 93% through the visible region. However, at 2 mTorr O₂, the visible light transmittance is $74.42 \pm 1.89\%$, on average, as it undulates between $57.72 \pm 1.89\%$ and $97.40 \pm 1.89\%$. This average decrease in visible light transmittance is due to the increased reflectance that emerges as a result of an increase in the TiO₂ refractive index with decreasing oxygen pressure. The overall sacrifice in visible light transmittance is also due to the presence of undulations, called interference fringes, in the spectra. Interference

fringes emerge as a result of a mismatch in the refractive indices of air, the thin film and the substrate: multiple reflections and transmissions at the air-film, film-substrate and substrate-air interfaces interfere constructively and destructively to produce interference fringes [103]. For this reason, the oxygen pressures which yield the highest TiO₂ refractive indices (i.e., 2 mTorr and 5 mTorr), also produce the most pronounced interference fringes.

The literature states that ZnO thin films should also exhibit a redshift of their absorption edge with decreasing oxygen pressure [104, 105]. The mechanism of bandgap narrowing in ZnO is similar to that of TiO₂, however its differences have important implications on the obtained transmittance behaviour. Notably, and contrary to what was observed for TiO₂, a redshift of the ZnO absorption edge is not appreciable at the presented PLD oxygen pressures. For example, ZnO coatings deposited at 2, 5 and 20 mTorr O₂, have an absorption edge located around 388 ± 2 nm, 389 ± 2 nm, and 385 ± 2 nm, respectively. Essentially, Zn¹⁺ interstitials have much higher formation energy than Ti³⁺ cations [106]. Therefore, in low oxygen pressure growth environments, ZnO films develop oxygen vacancies, but not Zn¹⁺ species [106]. As a result, for the same low PLD oxygen pressure, fewer charge carriers are introduced in ZnO than TiO₂, and a deeper dopant level (i.e., a level closer to the valence band) is obtained [106]. The ZnO bandgap is thereby narrowed to a much lesser degree than that of TiO₂, and a smaller redshift is observed. In fact, a relatively large concentration of oxygen vacancies in ZnO is required to detect any redshifting at all [105]. It is only when the oxygen vacancies supply a sufficiently large number of charge carriers that the redshift is detected, and thereafter redshifting increases with oxygen vacancy concentration [104, 105]. Therefore, it can be deduced that the current PLD oxygen pressures are insufficiently low to yield an appreciable narrowing of the ZnO bandgap.

Furthermore, visible light transmittance in ZnO remains relatively high and stable with decreasing oxygen pressure. At 2, 5 and 20 mTorr O₂, the minimum transmittance observed over the visible light region is $77.78 \pm 0.83\%$, $67.94 \pm 0.74\%$, and $78.31 \pm 1.37\%$, respectively. However, each of these also reach maxima of nearly 100%. Reflection and interference fringes account for the reductions in ZnO transmittance.

AZO thin films (i.e., ZnO thin films with 2% Al doping) demonstrate strong similarities to the ZnO films in their high visible light transparencies at all oxygen pressures. In the visible region, maxima approaching 100% are attained, while minima of $81.12 \pm 0.64\%$, $83.20 \pm 3.41\%$, and $73.21 \pm 0.62\%$ are reported for O₂ pressures of 2, 5 and 20 mTorr, respectively. However, a trend opposite to that of TiO₂ is observed in the UV region: as oxygen pressure is reduced, the absorption edge shifts towards shorter wavelengths. For instance, the 2 mTorr condition produces an absorption edge at 358 ± 4 nm, while for the 20 mTorr condition, the absorption edge is located at 372 ± 2 nm. Moreover, all of these absorption edges are significantly blueshifted from those of pure ZnO.

When ZnO is doped with Al, the Al atoms are incorporated substitutionally in the ZnO lattice, with Al atoms (radius ~ 0.51 Å) replacing Zn atoms (radius ~ 0.74 Å) [107]. Considering that aluminum has three valence electrons while zinc only has two, substitutional doping introduces a surplus of free electrons in the material and alters the structural, electrical and optical properties of ZnO [76]. In particular, an increase in the number of charge carriers with Al doping causes the ZnO absorption edge to shift towards shorter wavelengths [108]. This relationship between the optical bandgap and the charge carrier concentration in degenerate semiconductors is defined by the Burstein-Moss effect [109, 110]:

$$\Delta E_g = \left(\frac{\hbar^2}{2m^*} \right) (3\pi^2 n)^{\frac{2}{3}} \quad (2)$$

where ΔE_g quantifies the bandgap widening, \hbar is the reduced Planck's constant, m^* is the effective mass of electrons in the conduction band and n is the concentration of charge carriers. N-type degenerate semiconductors, such as AZO, have a sharp curvature in their conduction band, such that, upon doping, the conduction band states are rapidly populated with donor electrons [109]. When doping increases the carrier concentration in excess of the conduction band density of states, the Fermi level is pushed above the conduction band [111]. Consequently, the bandgap is effectively widened as electrons from the valence band can only be excited into unoccupied states above the Fermi level [108]. As the concentration of electrons increases, the height of the Fermi level above the conduction

band (and hence the apparent bandgap energy) increases according to the Burstein-Moss effect [111].

The redshift in the AZO absorption edge with increasing oxygen partial pressure is therefore attributed to a decrease in the concentration of charge carriers at elevated oxygen pressure. Essentially, as the concentration of oxygen is increased during deposition, AZO films exhibit: (1) a decrease in oxygen vacancies which act as donor species, and (2) a decrease in the concentration of Al substitutional atoms due to oxygen deactivation [76]. Both effects contribute to decreasing the carrier concentration and narrowing the bandgap. Moreover, the curvature of the ZnO conduction band is such that even relatively small changes in oxygen pressure produce pronounced shifts in the AZO absorption edge [112], as demonstrated in Figure 17 c).

The assertion that differences in observed transmittance are a result of changes in absorption due to the formation of oxygen vacancies is further substantiated by the analysis of absorbance and optical bandgap presented in Section 4.3.

Understanding the transmission behaviour of the thin films at NIR wavelengths can also provide insight into their suitability as encapsulant materials. Infrared radiation contains the thermal energy generated by the random motion of particles in all matter with temperature $> 0 K$. Therefore, an encapsulation which can prevent transmission of infrared light will synonymously impede thermal degradation of the perovskite. Figure 18 gives the NIR light transmission spectra of the TiO₂, ZnO and AZO thin films deposited at 2, 5 and 20 mTorr O₂. Both TiO₂ and AZO demonstrate a marked reduction in NIR transmittance with decreasing O₂ pressure. The minimum transmittance of TiO₂ in the NIR range decreases from approximately 97% to $72 \pm 1\%$ as the oxygen pressure is reduced from 20 to 2 mTorr. Similarly, for the same oxygen pressures, the minimum NIR transmittance of AZO decreases from approximately $74 \pm 1\%$ to $44 \pm 1\%$. Conversely, NIR transmittance remains above 85% in ZnO and is stable across all deposition pressures. The decrease in NIR transmittance observed with Al doping of ZnO has been reported in the literature and is a result of the increased concentration of charge carriers upon Al substitution [65]. Transmittance in the NIR region is proportional to electrical resistivity [113]; as the

concentration of charge carriers is increased by doping, resistivity is decreased and NIR transmittance is decreased. A similar explanation is made for the further reduction in AZO transmittance with decreasing O₂ pressure: decreasing O₂ pressure reduces oxygen-dopant deactivation and increases oxygen vacancies, thereby increasing the charge carrier concentration, and reducing NIR transmittance. In TiO₂, the reduction in NIR transparency is similarly correlated with the formation of Ti³⁺ species in the presence of low PLD oxygen pressure.

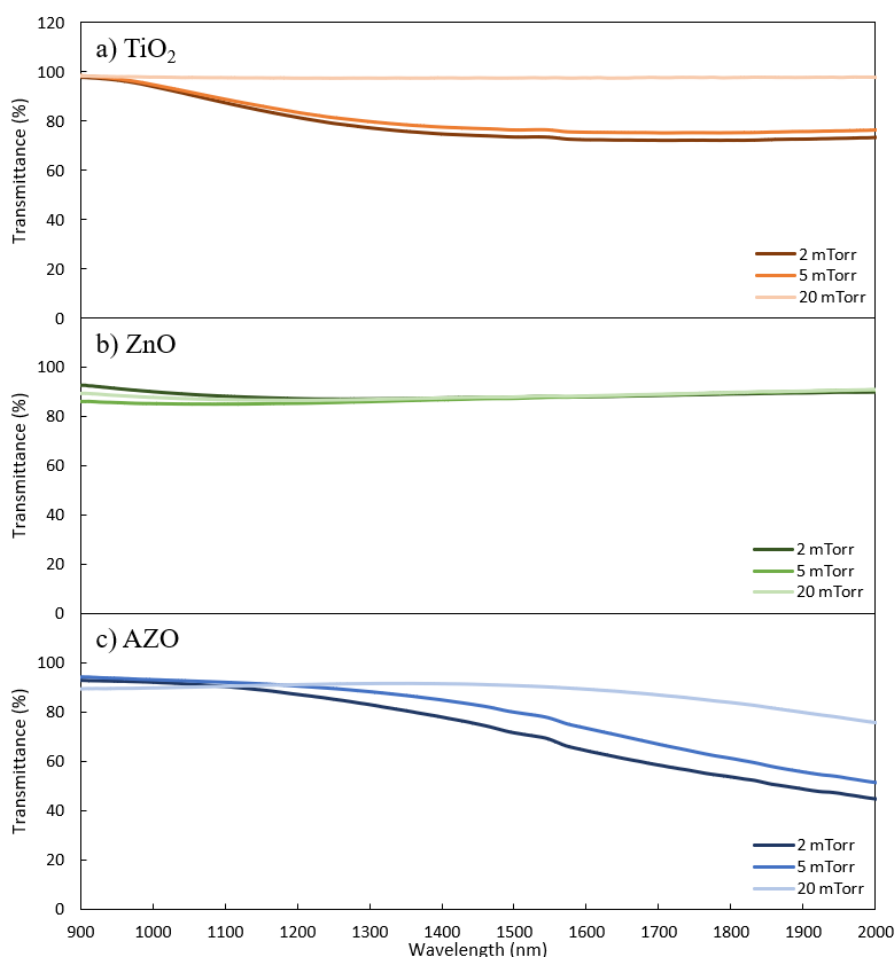


Figure 18: NIR light transmittance spectra of a) TiO₂, b) ZnO, and c) AZO coatings deposited by PLD at oxygen partial pressures of 0, 2 and 20 mTorr.

It is important to distinguish between reflectance and absorptance of degradation-inducing energy. Absorption of sufficiently energetic photons in inorganic semiconductors leads to the formation of free electron-hole pairs. In other words, when TiO₂, ZnO or AZO

photoprotective films prevent UV-degradation of the perovskite by absorbing UV light, free electrons and holes are generated. These energetic species can migrate into adjacent organic material layers and cause chemical reactions which can alter the structural, electrical and optical integrity of the materials and degrade them. This is a similar mechanism to that which causes photo-oxidative degradation at the TiO₂ electron transport layer – perovskite interface [8]. To prevent this form of degradation, degradation-inducing light should be reflected, not absorbed. Additionally, reflection of infrared light constitutes a better means of impeding thermal degradation than absorption. Figure 19 provides the light reflectance of TiO₂, ZnO and AZO thin films across the UV, visible and NIR wavelengths. Note that a break in the UV-Vis-NIR transmittance and reflectance data exists between 750 and 900 nm as a result of poor spectral resolution at the limits of the two UV-Vis and NIR spectrometers.

Figure 19 demonstrates that TiO₂ exhibits substantially higher reflectance than ZnO or AZO across the full spectrum of light. This behaviour is a result of the high refractive index of TiO₂, which causes high reflectance at the film-substrate and film-air interfaces [75]. In fact, for each material, the relationship between oxygen pressure and reflectance mimics that material's relationship between refractive index and oxygen pressure, as described in Section 4.1. Moreover, the reflectance data is consistent with the transmittance data in that the undulations of the interference fringes are the inverse of those observed in the transmittance spectra in Figure 17.

While TiO₂ has significantly higher UV and NIR light reflectance than its ZnO and AZO counterparts, it does not constitute the only encapsulating material capable of effectively delaying UV-degradation in perovskite solar cells. Should the thin photoprotective film be applied directly to an organic layer in the solar cell stack, TiO₂ is certainly advantageous. However, ZnO and AZO remain suitable candidates should they be deposited on an inorganic layer in the solar stack or on an insulating substrate to form hybrid glass or polymer encapsulations. This is the encapsulation approach taken herein.

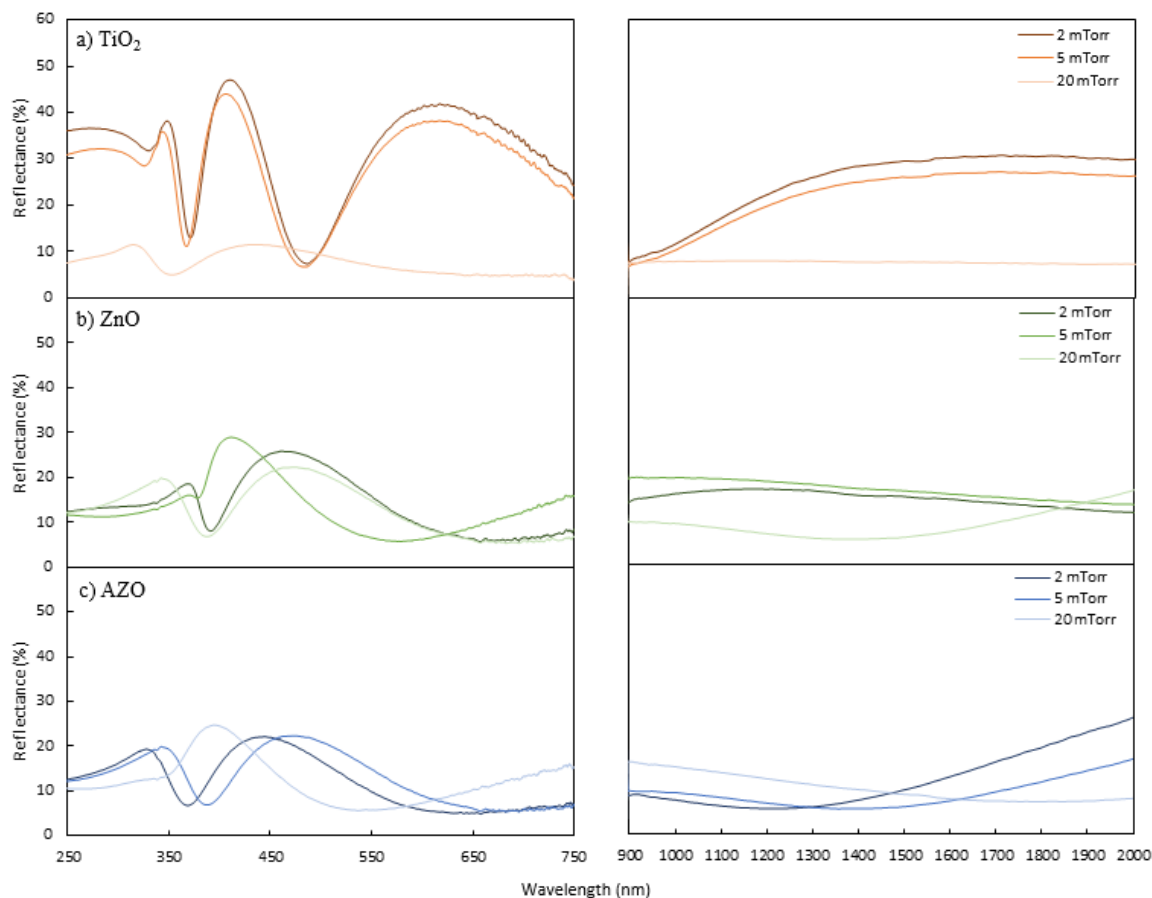


Figure 19: UV-Visible-NIR Light Reflectance of a) TiO₂, b) ZnO, and c) AZO coatings deposited by PLD at oxygen partial pressures of 0, 2 and 20 mTorr.

To determine the suitability of each coating as a thin film encapsulant for perovskite solar cells, the percentage of light irradiated from the sun that it absorbs/reflects was calculated. The spectrum of terrestrial solar irradiance was taken from ASTM G-173 and represents the AM1.5 solar power as a function of wavelength that reaches a surface on Earth tilted 37° towards the equator [114]. These conditions are optimized for photovoltaic panels positioned in the United States. Firstly, the absorption/reflection % of each coating was taken by subtracting its transmittance from unity at each wavelength. Next, the % absorption/reflection spectrum was multiplied by the irradiated sunlight spectrum to produce a spectrum which represents the absorbed/reflected irradiance. Finally, by integrating the absorbed/reflected irradiance curve to obtain the absorption/reflection area for each wavelength region (i.e., UV-B, UV-A, and visible) and comparing the results

against the areas obtained by integrating the same regions of the ASTM G-173 curve (which represent the total irradiance from the Sun), one obtains the percentage of light irradiated from the sun that is absorbed/reflected by the coating. This calculation procedure is described in further detail in Appendix A.

The trapezoidal method was used for numerical integration of the irradiation spectrums. The error of the integration is therefore defined as:

$$|E| \leq \frac{K(b-a)^3}{12n^2} \quad (3)$$

where b and a are the upper and lower bounds of the integration, n is the number of subintervals between $[a, b]$, and K is the maximum value of the second derivative of the function being integrated. Since the error is inversely proportional to the square of the number of subintervals, a small step size of 0.5 nm was selected for the integration. It is impossible to determine the true maximum value of the irradiance spectrum's second derivative because the function is given as a set of experimentally obtained values, and not as a mathematical function. Alternatively, the central difference method was used as a numerical estimation of the second derivative. Though this method introduces its own element of uncertainty, it is used nonetheless to gauge the order of magnitude of the integration error. Using this methodology, the areas under the ASTM G-173 solar irradiation curve are $0.68 \pm 0.02 \text{ W/m}^2$, $45.42 \pm 1.34 \text{ W/m}^2$ and $489.88 \pm 5.51 \text{ W/m}^2$ in the UVB, UVA, and visible light regions, respectively. These \pm errors, which represent the maximum possible integration errors, are relatively small and indicate that a sufficiently large number of subintervals was chosen for numerical integration by the trapezoidal method. A detailed description of the uncertainty propagation methodology applied to this analysis is given in Appendix A.

The percentage of UV-B, UV-A and visible light irradiated from the sun that is absorbed and reflected by the TiO₂, ZnO and AZO thin films at all studied oxygen pressures is illustrated in Figure 20. It further demonstrates the trends previously elucidated by the transmittance spectra in Figure 17. The percentage of UV-B and UV-A light absorbed/reflected by ZnO is high and remains relatively constant with decreasing PLD oxygen partial pressure. Additionally, for ZnO, there is a weak inverse relationship

between visible light absorption and oxygen pressure. AZO behaves similarly to ZnO in that it demonstrates minimal absorption/reflection of visible light and very strong absorption/reflection of UV-B light across all oxygen pressures. However, due the Burstein-Moss effect, UV-A absorption in AZO increases significantly from $32.7 \pm$ to 1.7% to $52.0 \pm 2.2\%$ with increasing O_2 pressure from 2 to 20 mTorr.

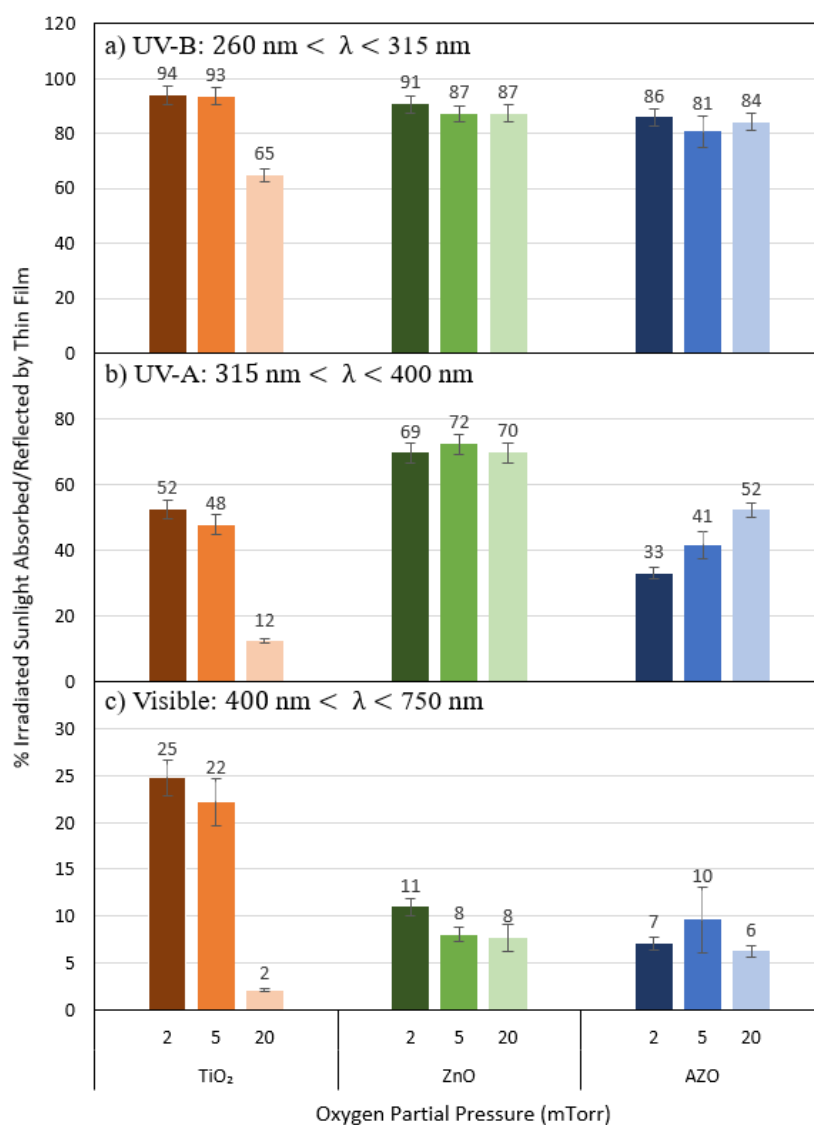


Figure 20: Percentage of a) UV-B, b) UV-A, and c) visible light irradiated from the Sun that is absorbed and reflected by the TiO₂, ZnO and AZO thin films as a function of the oxygen partial pressure at which they were deposited.

Figure 20 demonstrates an equally strong correlation between oxygen pressure and optical performance in TiO₂. A dramatic increase in UV-B, UV-A and visible light absorption is evident as the oxygen pressure is reduced from 20 to 5 mTorr. However, the difference in absorption between the 2 and 5 mTorr conditions is much less pronounced. This indicates that the concentration of oxygen vacancies and Ti³⁺ centers increases more significantly between 20 and 5 mTorr, than between 5 and 2 mTorr. From this analysis, it is evident that the 2 and 5 mTorr oxygen pressures constitute the best TiO₂ deposition conditions for perovskite solar cell encapsulation. Though their relatively high visible light absorptions may result in compromised device efficiencies, the 20 mTorr condition simply does not absorb enough UV light to be effective in preventing degradation.

It should be noted that as a result of filtration by the atmosphere, there is much more light irradiated in the visible range than in either of the UV ranges: $0.68 \pm 0.02 \text{ W/m}^2$, $45.42 \pm 1.34 \text{ W/m}^2$ and $489.88 \pm 5.51 \text{ W/m}^2$ in the UV-B, UV-A and visible light regions, respectively. Given the enormity of the visible light irradiance, it is therefore highly important to maximize visible light transmittance, otherwise device efficiency may be significantly compromised. Similarly, given that the intensity of UV-B light is very weak, it is less concerning than UV-A light in terms of the degradation it may induce in perovskites. In fact, this is the reason that UV-C light has not been considered in this analysis – effectively no UV-C light irradiated from the Sun will reach a photovoltaic panel mounted on Earth.

Importantly, Figure 20 facilitates a straightforward comparison of the difference in optical performance of the three thin film materials under investigation. At low oxygen pressure, there is almost no discernible difference between the TiO₂, ZnO and AZO coatings in terms of their interaction with UV-B light. In general, all three materials absorb the majority of UV-B light. However, differences emerge in the visible light region: low-oxygen pressure TiO₂ is approximately half as transparent to visible light as ZnO and AZO, while high-oxygen pressure TiO₂ is almost perfectly transparent. The most critical differences in optical properties are discerned in the UV-A range, where the high energy and intensity of light is capable of causing photodegradation in perovskites. Figure 20 demonstrates that across all oxygen pressures, the ZnO coatings transmit significantly less UV-A light than

their TiO₂ and AZO counterparts. For instance, at the 5 mTorr O₂ condition, which constitutes the oxygen pressure at which ZnO simultaneously absorbs/reflects the most UV-A light and the least visible light, ZnO absorbs/reflects 72.13 ± 3.05 W/m² of UV-A light, while TiO₂ and AZO absorb/reflect just over half that amount: 47.51 ± 3.06 W/m² and 41.38 ± 4.09 W/m², respectively. Therefore, based on its ability to effectively screen large amounts of UV-light while remaining highly transparent to visible light, it is clear that ZnO is the most effective material for encapsulation of PSCs.

4.3 Optical Bandgap

The bandgap is the optical property of a semiconductor that dictates which wavelengths of light have sufficient energy to be absorbed (i.e., promote an electron from the valence band to the conduction band), and which do not. In fact, it is the bandgap that positions the absorption edge, thereby creating distinct regions of absorption and transmission. The bandgap is commonly determined by the Tauc method [115], which suggests that there is a linear relationship between the absorption coefficient (α) and the energy of a photon ($h\nu$) as follows:

$$(ah\nu)^\gamma = A[h\nu - E_g] \quad (4)$$

where h is Planck's constant, ν is the frequency of photons, A is the slope in the linear region of the Tauc plot, E_g is the bandgap and γ is a material dependent property which defines the type of bandgap (i.e., $\gamma = 2$ for direct or $\gamma = \frac{1}{2}$ for indirect bandgaps). The photon frequency (ν) can then be simplified and expressed as a function of wavelength (λ), and the speed of light (c) according to:

$$\nu = \frac{c}{\lambda} \quad (5)$$

As given by Equation (4), plotting $(ah\nu)^\gamma$ as a function of $h\nu$ yields a Tauc plot from which E_g can be extrapolated as the x-intercept of the linear region. The absorption coefficient (α) can be determined from the transmittance and reflectance data obtained by UV-vis spectroscopy because any light that is not transmitted (T) or reflected (R) must be absorbed (A):

$$A = 100\% - T - R \quad (6)$$

The absorption spectra of the TiO₂, ZnO and AZO thin films calculated by Equation (6) are given in Appendix B. It is assumed in Equation (6) that the reflectance term is the percentage of light reflected solely by the thin film material (i.e., the material for which E_g is being determined). In reality, the reflectance data obtained herein includes some amount of reflection from the coating-substrate interface. Additionally, the calculation necessitates non-arbitrary values of transmittance and reflection. In other words, each data set must have been obtained using a reference which represents 100% transmittance and reflectance, respectively, such that the values of T and R represent the true percentage of incident light that was transmitted or reflected. While this was the case for the transmittance data, the reflectance data will introduce certain error since it was obtained using a reference with only > 95% reflectance. The absorption coefficient can then be expressed as a function of absorption (A) and film thickness (t):

$$\alpha = \frac{2.303A}{t} \quad (7)$$

Depending on its morphology and crystal structure, the direct or indirect bandgap will dominate in TiO₂ [64]. For this reason, the Tauc plots for both the direct and indirect electronic transitions of TiO₂ are given in Figure 21. The plotted spectra are representative of the absorption at the center of one of the coated quartz samples, however average bandgaps obtained for a minimum of four samples across three probing locations, each, are listed in Table 7.

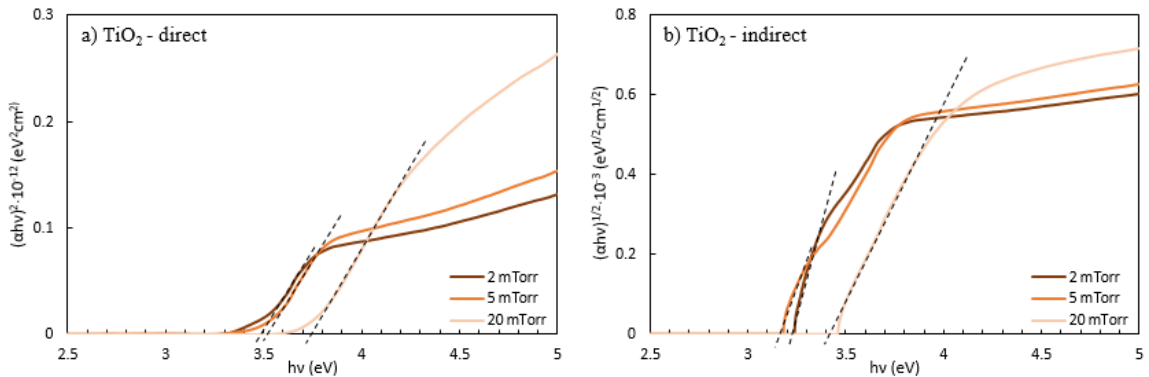


Figure 21: Absorbance spectra for the a) direct and b) indirect bandgaps of TiO₂ deposited by PLD at oxygen pressures of 2, 5 and 20 mTorr. Black dashed lines are used to extrapolate E_g from their intersection with the abscissa.

The direct bandgaps of TiO₂ are all substantially larger than the indirect ones. To determine the dominant electronic transition type and to validate the obtained bandgaps, the following equation can be used to predict the location of the absorption edge:

$$\lambda_{predicted} = \frac{hc}{E_g} \quad (8)$$

The direct bandgaps of TiO₂ deposited at 2, 5 and 20 mTorr are 3.49 ± 0.07 eV, 3.51 ± 0.05 eV and 3.75 ± 0.03 eV, respectively, and yield absorption edges at 355 ± 7 nm, 354 ± 5 nm, and 330 ± 3 nm. These absorption edges are all within 15 nm of those obtained experimentally in Figure 17. Conversely, the indirect bandgaps of TiO₂ extrapolated from the Tauc plot in Figure 21 b) are 3.18 ± 0.08 eV, 3.23 ± 0.05 eV, and 3.42 ± 0.07 eV for oxygen pressure of 2, 5 and 20 mTorr, respectively. These have corresponding unrealistic absorption edges at 389 ± 10 nm, 383 ± 6 nm, and 363 ± 7 nm, which are all more than 20 nm closer to the visible region their experimentally-obtained counterparts. Therefore, the direct bandgap seems to better predict the true absorption behaviour of the TiO₂ thin films. Any differences are likely due to the high refractive index of TiO₂, and thereby the large amount of reflection at the coating-substrate interface. Moreover, the results confirm the trends previously observed in the transmittance spectra and extinction coefficients: the TiO₂ bandgap narrows as the oxygen pressure is reduced due to the formation and self-doping nature of oxygen vacancies and Ti³⁺. Although the TiO₂ bandgap varies significantly with crystallinity, the films deposited by this room-temperature PLD method are similar to those reported in the literature for amorphous TiO₂ ($E_g \sim 3.5$ eV [64]).

ZnO and AZO are considered to be direct bandgap semiconductors [116, 117]. As a result, their direct electronic transition Tauc plots are given in Figure 22 and the extrapolated bandgaps are summarized in Table 7.

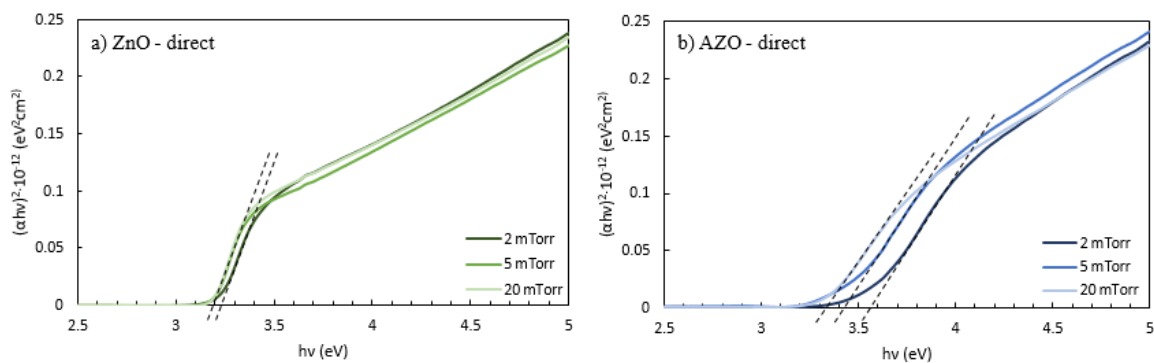


Figure 22: Absorbance spectra for the direct bandgaps of a) ZnO and b) AZO deposited by PLD at oxygen pressures of 2, 5 and 20 mTorr. Black dashed lines are used to extrapolate E_g from their intersection with the abscissa.

The absorption edges of ZnO and AZO predicted by the Tauc method very closely resemble those read from the experimental transmittance spectra. The relationships between bandgap and oxygen pressure are also in good agreement with those previously elucidated. In ZnO, bandgap energy is relatively constant with increasing oxygen pressure, and its magnitude is consistent with the literature ($E_g = 3.2$ eV [116]). When ZnO is doped with Al, its bandgap widens and becomes highly sensitive to changes in oxygen pressure due to the Burstein-Moss effect and the inverse influence of oxygen on the concentration of charge carriers. A narrowing of the AZO bandgap from 3.51 ± 0.01 eV to 3.35 ± 0.01 eV was observed with increasing oxygen pressure. The magnitude of the AZO bandgap depends on the concentration of dopant, deposition temperature and oxygen pressure, but similar studies found E_g from 3.3 eV – 3.6 eV [76], which are consistent with those reported herein.

Overall, ZnO thin films tend to have the narrowest bandgaps, while TiO₂ and AZO films have wider bandgaps, which change with oxygen pressure. As a result of the location of its corresponding absorption edge, the analysis finds that the ZnO material is able to absorb a larger amount of UV-A light than either TiO₂ or AZO, even at their most optimal oxygen deposition pressures.

Table 7: Direct bandgaps (E_g) of TiO₂, ZnO and AZO as a function of oxygen partial pressure. Predicted ($\lambda_{predicted}$) and experimental ($\lambda_{experimental}$) absorption edges are provided to validate the obtained E_g .

	P_{O_2} (mTorr)	E_g (eV)	$\lambda_{predicted}$ (nm)	$\lambda_{experimental}$ (nm)
TiO ₂	2	3.49 ± 0.07	355 ± 7	368 ± 4
	5	3.51 ± 0.05	354 ± 5	361 ± 4
	20	3.75 ± 0.03	330 ± 3	342 ± 2
ZnO	2	3.21 ± 0.01	386 ± 1	388 ± 2
	5	3.19 ± 0.00	388 ± 1	389 ± 2
	20	3.20 ± 0.00	387 ± 1	385 ± 2
AZO	2	3.51 ± 0.01	353 ± 1	358 ± 4
	5	3.39 ± 0.02	365 ± 2	368 ± 4
	20	3.35 ± 0.01	371 ± 1	372 ± 2

4.4 Conclusions

An experimental study was conducted to investigate the influence of oxygen pressure on the optical properties of TiO₂, ZnO and AZO thin films deposited by room temperature PLD, as they relate to PSC encapsulation. Interference reflectometry was used to obtain extinction coefficients and refractive indices, and UV-Vis-NIR spectroscopy was used to obtain transmittance spectra which were reported for oxygen partial pressures from 0 to 20 mTorr. The results show that the optical performance of TiO₂ and AZO is sensitive to PLD oxygen pressure within the tested range, and can therefore be optimized for the encapsulation application. In particular, TiO₂ was highly sensitive to changes in oxygen pressure: a significant increase in $\lambda = 368$ nm extinction coefficients and refractive indices, and a redshift in the absorption edge from 342 ± 2 nm to 368 ± 4 nm, accompanied by a narrowing of the bandgap were observed as the O₂ pressure was reduced from 20 mTorr to 2 mTorr. The above were found to correspond to an increase in oxygen vacancies and Ti³⁺ with decreasing oxygen. The AZO thin films exhibited the opposite trends which were justified by an increase in the concentration of charge carriers with decreasing oxygen pressure, according to the Burstein-Moss effect: by reducing O₂ pressure from 20 to 2 mTorr, the extinction coefficients and refractive indices at $\lambda = 368$ decreased and increased, respectively, and a blueshift of the absorption edge from 372 ± 2 nm to 358 ± 4 nm with widening bandgap was observed. Conversely, ZnO films had stable optical properties at deposition partial pressures between 2 and 20 mTorr O₂. In general, manipulation of the

oxygen pressure during all thin film depositions permitted tuning of the absorptive behaviour to maximize the potential to block UV-A light. However, ZnO coatings demonstrated significantly more UV-A light absorption/reflection than TiO₂ or AZO. At the oxygen pressures studied, ZnO, TiO₂, and AZO coatings exhibited maximum percentages of absorbed/reflected UV-A light of $72.13 \pm 3.05\%$, $52.30 \pm 2.72\%$, and $52.06 \pm 2.20\%$ at 5, 2 and 20 mTorr O₂, respectively. Moreover, TiO₂ had more severely compromised visible light transmittance than ZnO or AZO at the above conditions. As a result, the findings suggests that ZnO may be the most suitable candidate material for PSC encapsulation in terms of its optical properties.

Chapter 5

5 Coating Durability

Delaying perovskite degradation is not the only factor to consider in ensuring that perovskite solar cell lifetimes are sufficiently long for commercialization. A solar panel must also be durable enough to withstand normal operating conditions, such that it does not require significant maintenance or need to be disposed of and replaced due to mechanically- or environmentally-inflicted damage. Exposure to high temperature, low temperature, humidity and precipitation is common in normal outdoor operation. Moreover, debris can be picked up by the wind and collide with solar panels, marring or abrading them. Finally, cleaning with chemical solutions may be required to remove accumulated residue. Therefore, in designing a solar cell encapsulation for preventing perovskite degradation, durability in the predicted operating environment must also be considered. Herein, the durability of the 200 nm TiO₂, ZnO and AZO UV-protection layers deposited at 5 mTorr O₂ on 75 × 50 mm glass substrates (Corning 2947) is evaluated. Substrates with larger surface area were selected to accommodate larger-area testing.

5.1 Adhesion

Strong adhesion of a thin film to its substrate is vital to durability and prevention of delamination. The adhesion of the UV-protection films to their glass substrates was evaluated according to the MIL-C-48497A Military Specification's durability requirements for single or multilayer optical coatings (3.4.1.1). Transparent cellophane tape (1/2 in. wide, Type I L-T-90) was applied with firm pressure to the coated glass surface and then quickly removed by peeling at an angle perpendicular to the surface. An optical coating is said to have 'passed' the adhesion test if none of the coating is removed with the tape. The tested TiO₂, ZnO and AZO specimens were inspected by optical microscopy (Sensofar) and all were considered to have passed the adhesion test. This result demonstrates that the PLD technique has produced high quality films with good bonding strength to the glass substrate. If this work is to be adapted for flexible PSC encapsulations where the thin UV-protection films are deposited on polymer substrates, adhesion will need to be re-evaluated. Challenges with adhesion of ceramic thin films to polymer substrates

are common due to high internal strain resulting from large mismatches in the thermal expansion coefficients of the two materials.

5.2 Abrasion Resistance

Resistance to abrasion mimics the durability of the coatings against mechanical wear that might arise in normal operating conditions. Ideally, coatings should have high wear-resistance to ensure that delamination does not occur in the presence of mechanical abrasives, resulting in compromised ability to prevent perovskite degradation. The abrasion resistance of 200 nm TiO₂, ZnO and AZO coatings on glass was evaluated according MIL-C-48497A standard's Moderate Abrasion test (3.4.1.3). In this test method, an abrader is used to rub 50 linear strokes back and forth across the coating surface. The abrader is an Eraser Abrasion Coating Tester, capable of applying a constant force of 1 pound normal to the coated surface, to which a clean, dry CCC-C-440 1/4 in. thick cheesecloth is attached. A "pass" of the moderate abrasion test is declared when there are no signs of deterioration following the test. It should be noted that for films as thin as the ones investigated herein, this constitutes a very difficult test to pass.

Microscope images of the TiO₂, ZnO and AZO films before and after the moderate abrasion test are given in Figure 23. In all cases, the abrasion scratch marks appear as vertical lines in (ii). The images demonstrate that TiO₂ experiences the most severe damage due to abrasion. On the ZnO thin film, evidence of wear is visible, however the severity is drastically reduced. Contrastingly, there are nearly no detectable signs of wear on the AZO coating. This is consistent with reported hardness values for each material, where AZO is the hardest, and amorphous TiO₂ is the least hard [118, 119].

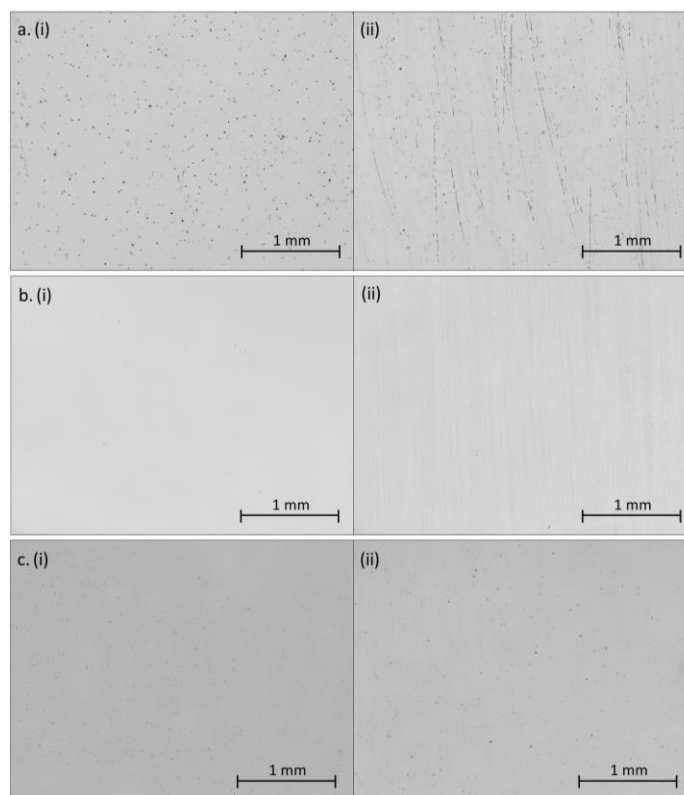


Figure 23: Microscope images (5x magnification) of (a) TiO₂, (b) ZnO, and (c) AZO thin films deposited at 5 mTorr O₂, (i) before and (ii) after the MIL-C-48497A moderate abrasion test.

While technically the TiO₂ and ZnO films did not pass the moderate abrasion test, a subsequent analysis was performed to determine the degree of delamination and to assess whether the coatings could still provide some protection against perovskite degradation after abrasion. To this end, the UV-Vis transmittance of each coating on Corning glass substrates was measured before and after the moderate abrasion test, using the experimental setup described in Section 4.2.1. The results are plotted against an uncoated Corning glass substrate in Figure 24. The degree of delamination after abrasion is assessed by comparing the coated spectra after abrasion with their uncoated counterpart. The metal oxide thin films under investigation all display signature marked absorption in the UV range. Delamination due to abrasion can therefore be detected as an increase in UV light transmittance toward a spectrum that resembles that of the glass substrate. This can be further quantified as the RMSE between coating transmittance before and after abrasion. The RMSEs calculated for

TiO₂, ZnO and AZO are 0.80, 1.39 and 2.07%, respectively, with normalized scatter indices of 1.23, 2.01 and 3.00%, respectively. Interestingly, even though the TiO₂ and ZnO coatings did not pass the moderate abrasion test by visual inspection, their transmittance spectra do not show signs of delamination. This result indicates that though marring occurred, the adhesion of the coatings to their substrate was strong enough such that the coatings can still provide nearly uncompromised protection against UV-induced degradation.

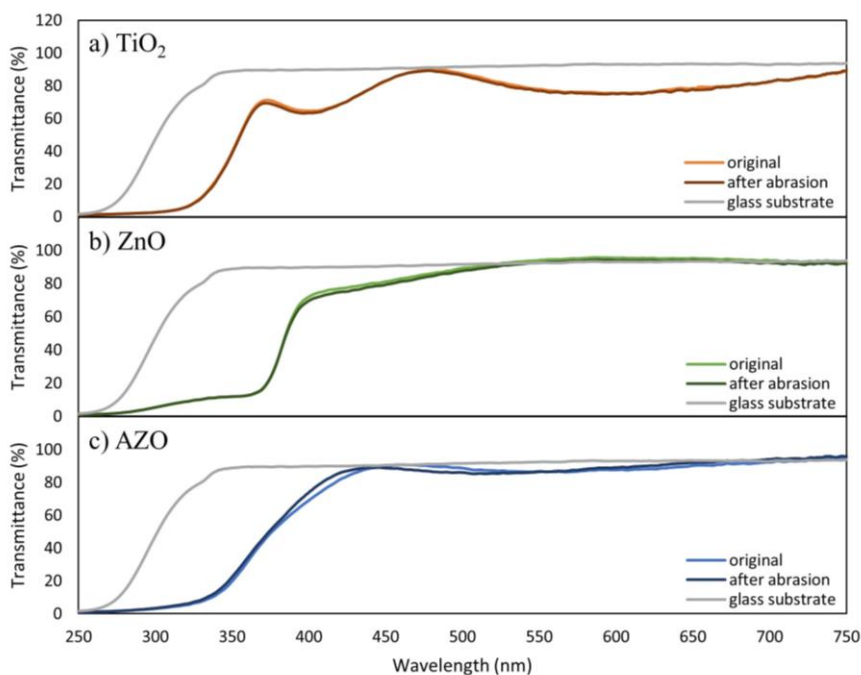


Figure 24: UV-Vis Transmittance of a) TiO₂, b) ZnO and c) AZO thin films before and after the MIL-C-48497A moderate abrasion test. All spectra are taken with air as a reference.

5.3 Chemical Stability

The resistance of the TiO₂, ZnO and AZO coatings to dissolution in chemicals was evaluated according to a modified version of the MIL-C-48497A solubility and cleanability tests (3.4.2.2). In the solubility test, each coated glass substrate was completely immersed and sonicated for 10 mins in: (i) water (Milli-Q); (ii) soapy water (MilliQ + 2 drops liquid detergent); (iii) acetone (Sigma-Aldrich, 99.9%), and; (iv) 2-propanol (Sigma-Aldrich,

99.9%). The coatings are then removed and allowed to dry by natural evaporation of the solvents. A surface that shows no evidence of coating removal constitutes a “pass.” Figure 25 provides camera images taken of the TiO₂, ZnO and AZO coatings before and after sonication in each of the chemical solutions. No signs of damage are apparent following immersion and sonication in any of the chemicals. As a result, each coating material passes the solubility test. This finding is consistent with the literature, which cites that TiO₂ [119], ZnO and AZO [120] thin films all have good chemical resistance.

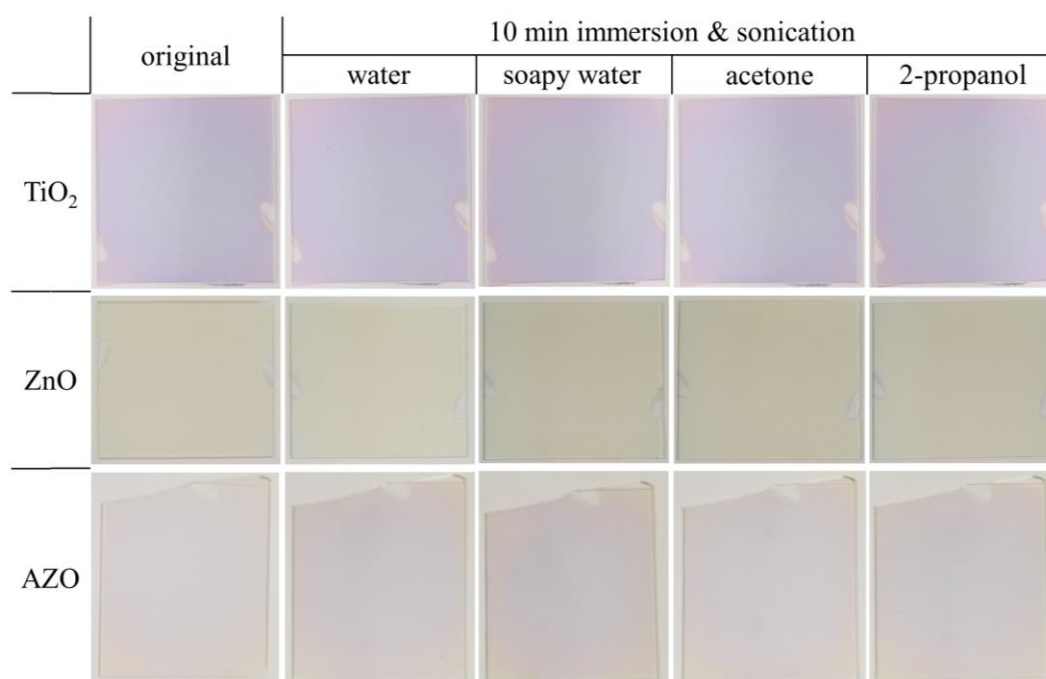


Figure 25: Camera images of the TiO₂, ZnO and AZO coatings before and after being subject to the MIL-C-48497A chemical solubility test.

In the cleanability test, the coatings are wiped with a cheesecloth moistened by submersion in each of the four solutions from the solubility test. The test mimics typical cleaning with a wetted cloth. The passing criteria for the cleanability test are no visible signs of coating removal or scratches. All of the tested coatings passed the cleanability test, indicating that the selected TiO₂, ZnO and AZO materials are appropriate for subsection to cleaning.

5.4 Conclusions

In summary, the durability of the TiO₂, ZnO and AZO thin film UV-protection coatings was evaluated by means of adhesion, abrasion, solubility and cleanability tests taken from the MIL-C-48497A Military Specification for optical coatings. A summary comparing the durability test results of each coating material is provided in Table 8. All of the tested materials exhibited excellent chemical resistance and passed the adhesion, solubility and cleanability tests. However, only the AZO coating passed the moderate abrasion test. The results indicate that AZO provides the best resistance to wear of all the materials tested, followed by ZnO, which also provides very good wear-resistance, and then TiO₂, which provides moderate wear-resistance. Nonetheless, the amount of material removed by the TiO₂ and ZnO abrasion tests was insignificant, such that their capacity for UV-protection was unaffected. Therefore, TiO₂, ZnO and AZO all constitute good candidate materials in terms of their application as durable wear- and chemical-resistant coatings for PSC encapsulation.

Table 8: Summary of durability test results.

MIL-C-48497A Test	TiO₂	ZnO	AZO
Adhesion	PASS	PASS	PASS
Abrasion	FAIL	FAIL	PASS
Solubility	PASS	PASS	PASS
Cleanability	PASS	PASS	PASS

Chapter 6

6 Perovskite Degradation Studies

Limited research to-date has focused on optimizing encapsulation strategies which target the prevention of UV-induced degradation in perovskites. However, since UV light is a catalyst of photo-oxidative degradation in perovskites, its elimination by absorption and reflection in thin film layers which supersede the perovskite layer, has the potential to greatly extend the lifetime of perovskite solar cells. A recent study by Ouafi et al. saw significant MAPbI₃ degradation and the formation of the PbI₂ degradation product after exposure of the perovskite to 12 hours of intense (350 mW/cm²) UV light under ambient temperature and 5% relative humidity [20]. This form of degradation was detected by: (1) a change in colour from black to yellow; (2) the respective disappearance and emergence of MAPbI₃ and PbI₂ diffraction peaks in the X-Ray diffractograms; (3) an increase in transmittance, and; (4) an increase in the void fraction, as determined by FESEM. The authors employed intrinsic stabilization techniques to successfully delay UV degradation via bromide incorporation.

Herein, the thin-film based hybrid encapsulation technology developed throughout this work is assessed for its ability to improve the UV stability of perovskites and optimized according to thin film material (TiO₂, ZnO and AZO) and PLD oxygen deposition pressure (2, 5 and 20 mTorr). Degradation of the perovskite is monitored by colour change, UV-Vis-NIR transmittance and XRD.

6.1 Experimental

6.1.1 Perovskite Layer Deposition

MAPbI₃ was obtained from Solaronix as a precursor solution of PbI₂ (1.2 mol/kg) and MA (1.2 mol/kg) in a mixture of gamma-butyrolactone and ethanol. The perovskite layer was deposited by spin coating (Laurell WS-200-4NPP/HFP) 85 μ L of precursor solution at 3000 rpm for 30 s on quartz substrates (McMaster-Carr, 1 in. \times 1 in.). It should be noted that quartz substrates were selected for experimentation due to their negligible absorption of UV light, however, outside of a research context, glass substrates are preferred for

encapsulation since they are more inexpensive. Moreover, since glass absorbs only a very small percentage of UV light [121], it will not provide sufficient protection from UV-degradation on its own, therefore necessitating the addition of UV-protection thin films. Before deposition, the quartz was cleaned with a mildly abrasive slurry of powder detergent and Milli-Q water to increase its hydrophilicity and ensure uniform coverage upon spin coating, followed by rinsing with additional Milli-Q water and isopropanol. Where a UV-protection thin film was used, the perovskite was spin coated on the side of the quartz opposite to the pulsed laser deposited TiO₂, ZnO or AZO. The samples were then annealed in dry air for 15 minutes at $65 \pm 2^\circ\text{C}$ in order to evaporate the gamma-butyrolactone and ethanol solvents and crystallize the MAPbI₃ without causing thermal degradation. The morphology of the resulting layer is revealed by FESEM (Hitachi SU8230 Regulus) according to previously described procedures. Figure 26 demonstrates the formation of distinct aggregates of MAPbI₃ crystals with varying diameter of $\sim 20 - 150 \mu\text{m}$ surrounded by voids.

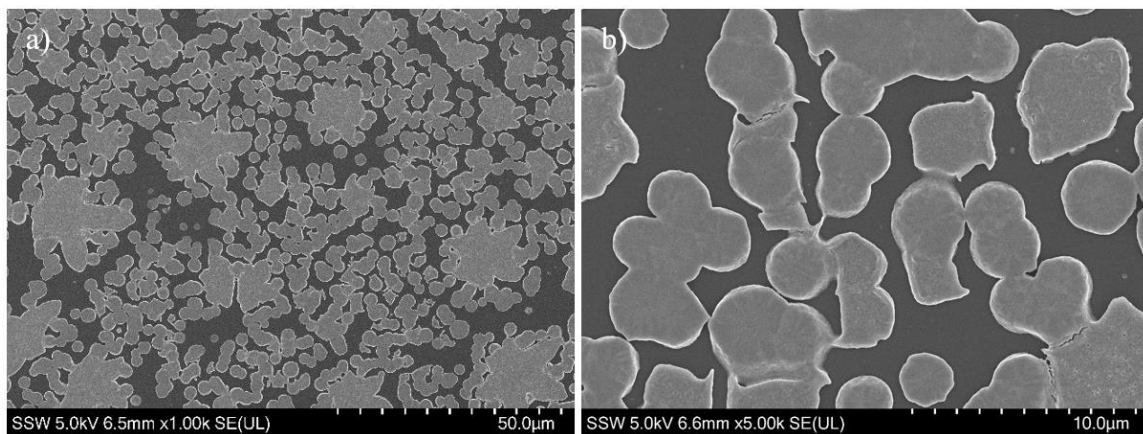


Figure 26: FESEM images at a) 1.00k and b) 5.00k magnification of the pristine perovskite layer deposited on a quartz substrate.

Maintaining uniform cluster diameter and thickness across spin coating depositions is crucial because the rate of degradation increases with the surface area exposed to degradants. As a result, the reproducibility of the MAPbI₃ layer was assessed by measuring the cluster height across three samples deposited using identical spin coating deposition parameters. Additionally, for each sample, the cluster height was measured at three

positions, according to the probing locations given in Figure 16. Furthermore, the height of aggregates was: (1) measured by optical profilometry using the Sensofar optical microscope to acquire a 3D profile of a $877.20 \mu\text{m} \times 660.48 \mu\text{m}$ surface area and corresponding ISO25178 surface texture parameters, and; (2) verified by mechanical profilometry using the Dektak 3ST stylus profilometer with a scan length of $4000 \mu\text{m}$, stylus force of 30 mg and a scan speed of $100 \mu\text{m/s}$. Results are given in Table 9.

Table 9: Mean height of MAPbI₃ clusters across three samples deposited using identical spin coating deposition parameters (85 μL , 3000 rpm, 30 s).

	Method	Sample 1	Sample 2	Sample 3	Average	Standard Deviation
Arithmetic Mean Height of Surface (nm)	<i>Optical Profilometry</i>	121 ± 12	140 ± 58	139 ± 26	133 ± 33	11
	<i>Mechanical Profilometry</i>	129 ± 15	147 ± 36	139 ± 20	138 ± 27	9

Optical and mechanical profilometry techniques found similar average arithmetic mean heights of $133 \pm 33 \mu\text{m}$ and $138 \pm 27 \mu\text{m}$, respectively, across the three samples. Moreover, the fairly small differences in average heights between samples yield low standard deviations, indicating good reproducibility of the spin coating deposition method. It should be noted that the relatively large \pm errors on the means are a reflection of the significant variation in the size of MAPbI₃ clusters in a single sample, as shown in Figure 26.

6.1.2 UV Degradation Methodology

To study the rate of perovskite photodegradation, samples were irradiated with 368 nm UV-A light using a NEARCAM energy-adjustable lamp. The UV lamp emission spectra are given in Figure 42 of Appendix B. Three lamps positioned side-by-side permitted simultaneous irradiation of three perovskite samples. The irradiation intensity of each lamp was adjusted to $230 \pm 10 \text{ mW/cm}^2$, as measured using a Linshang LS126A radiometer with UVALED-X0 probe, having a 10 mm measuring aperture. This represents an irradiance 50 times more intense than that of the UV light in the AM1.5 solar spectrum (i.e., 4.61 mW/cm^2 [114]). Hence, the samples studied herein are subject to accelerated UV

aging tests, where degradation occurs much more rapidly than it would under natural sunlight conditions. Additionally, to negate the confounding effects of water-induced degradation, UV degradation experiments were performed at ambient temperature in a positive pressure glovebox supplied with dry air, where the relative humidity was maintained at a level $< 2\%$.

Figure 27 a) provides a schematic of the test setup used for the degradation experiments. It depicts a UV lamp suspended normally above a coated quartz sample resting on a sample stage. In Figure 27 b) the illumination pathway is illustrated, wherein UV light directly irradiates the UV-protection thin film. Depending on the optical performance of the UV-protection film, some of the UV light is reflected/absorbed and the remainder is transmitted through the quartz substrate (which has negligible absorption) to the perovskite layer underneath. The UV light that reaches the perovskite is then capable of causing degradation.

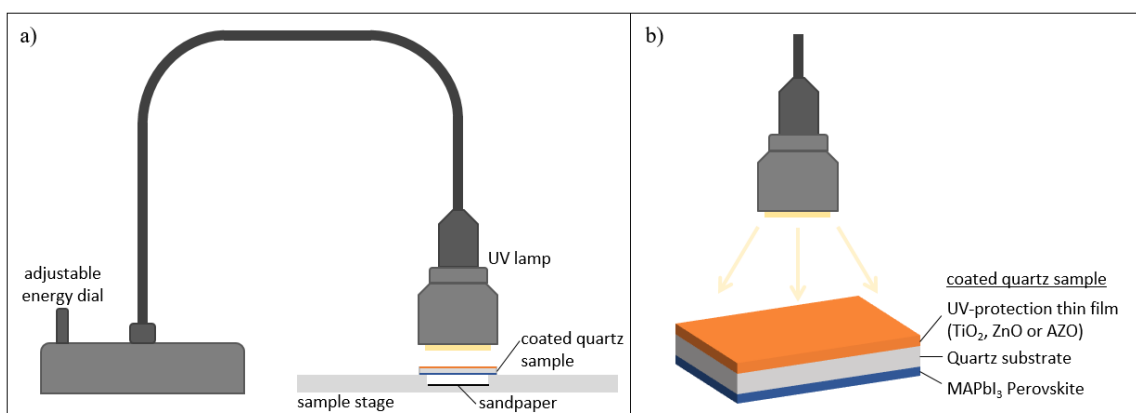


Figure 27: a) Schematic of the testing setup for UV degradation experiments with b) an enlarged view of the irradiated coated quartz sample layer configuration. Note that this schematic is not to-scale.

The distance from the edge of the light source to the surface of the coated quartz sample was set to 1.05 cm. At this close of a distance and with such a high intensity of light, it is conceivable that the temperature of the sample might increase so as to cause thermal degradation of the perovskite. However, a thermocouple positioned on the surface of a quartz substrate found that the temperature increased by less than 1°C over 1 hour of

continuous illumination. Therefore, thermal degradation is unlikely to confound the results obtained herein.

The sample stage was carefully engineered out of glass (Corning 2947) to satisfy a number of functionalities. First, a space with a depth of 0.35 cm and a width just less than the length of the quartz substrate was created over which the quartz is placed. In this way, the perovskite is exposed to air flow underneath such that: (1) the amount of heating is reduced to prevent thermal degradation, and; (2) there is sufficient oxygen to promote an accelerated form of photo-oxidative degradation. Secondly, a strip of 120-grit black sandpaper was secured across the bottom length of the space in the sample stage to prevent any UV light transmitted adjacent to the quartz sample and through the glass sample stage from being reflected off of the glovebox floor and onto the perovskite. Finally, glass was selected as the material of construction for the sample stage because it absorbs almost no UV light and therefore will not overheat and contribute to thermal degradation of the perovskite.

Perovskite layers protected by TiO₂, ZnO and AZO thin films deposited at 2, 5 and 20 mTorr O₂, were subject to 8 hours of UV light irradiation. Before exposure and at 2 hour intervals, the perovskite layers were assessed for signs of degradation by appearance and UV-Vis-NIR transmittance (methodology described in Section 4.2.1). All experiments were performed in replicate to ensure reproducibility.

6.2 Experimental Control

Before evaluating the ability of the UV-protection thin films to delay perovskite photodegradation, a control experiment was performed to confirm that UV light will induce substantial degradation and to ensure that oxidative mechanisms (in the absence of UV light) are not significant contributors to degradation. In the control experiment, four quartz samples were coated with only perovskite (i.e., no TiO₂, ZnO or AZO). Two samples were exposed to 8 hours of UV light irradiation, while the other two were left under ambient light conditions for the same amount of time.

Figure 28 provides a visualization of the degree to which each light source degrades the perovskite in 8 hours of exposure time. It clearly demonstrates that under UV light, the colour of the perovskite undergoes a drastic transformation from dark grey to yellow, indicating the formation of the PbI_2 degradation product. Contrastingly, the perovskite exposed to ambient light conditions in the glovebox environment (i.e., dry air, < 2% relative humidity) exhibits no colour change after 8 hours. Further extension of the ambient light experiment to 96 hours also did not precipitate any changes in colour.

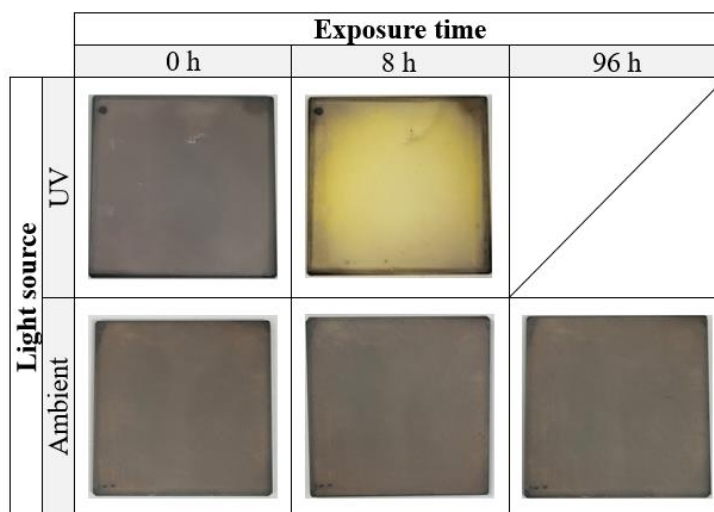


Figure 28: Camera images of perovskite-coated quartz samples degraded for 8 and 96 hours under UV and ambient light, respectively.

Examination of the UV-degraded sample by FESEM in Figure 29 reveals microstructural changes in MAPbI_3 due to UV exposure. A significant refinement in grain size and the formation of tiny voids within the MAPbI_3 clusters of grains is observed in the degraded sample. This is consistent with the microstructural changes reported by Ouafi et al. [20].

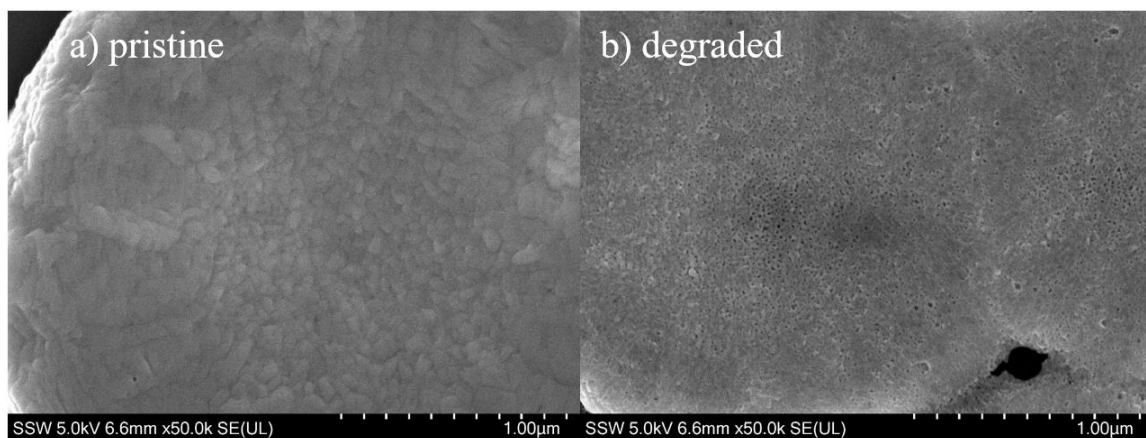


Figure 29: FESEM images at 50.0 k magnification of MAPbI₃ a) before and b) after exposure to 8 hours of UV radiation.

Degradation of perovskites is also identified by an increase in the percentage of transmitted light, due to the increase in porosity and the distinct transmittance behaviour of the PbI₂ degradation product [20]. Therefore, transmittance spectra of the perovskite samples degraded under UV and ambient light were acquired and are provided in Figure 30.

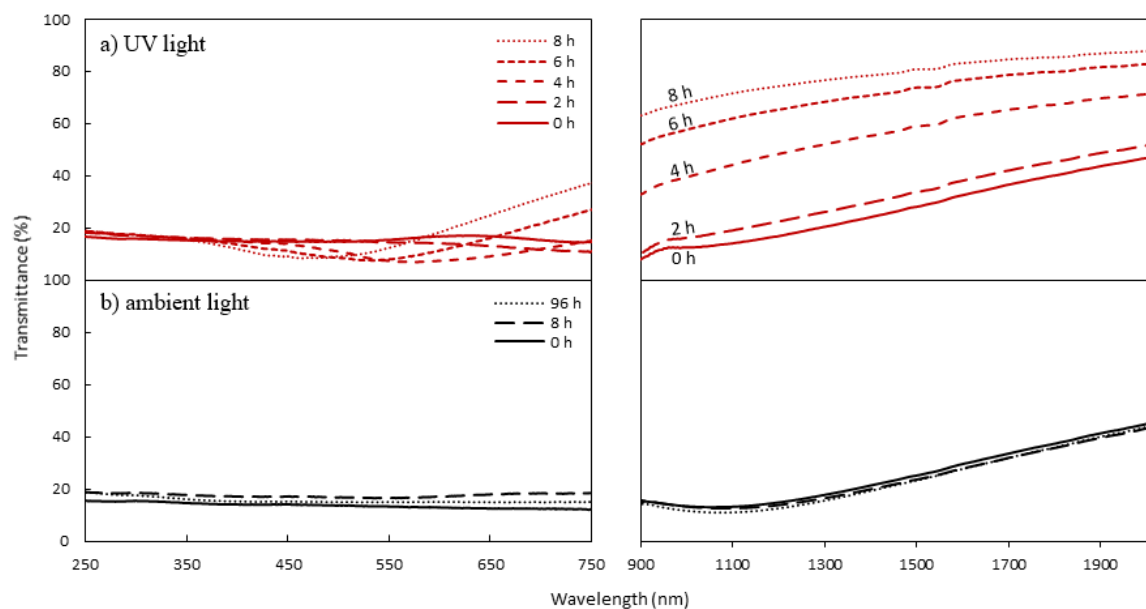


Figure 30: UV-Vis-NIR transmittance spectra of the perovskite coatings exposed to a) UV light and b) ambient over the course of 8 and 96 hours, respectively.

The trends are consistent with those revealed by the camera images: the perovskite exposed to UV light exhibits significant degradation in the form of increasing transmittance in just 8 hours, while the perovskite exposed to ambient light has stable transmittance over 96 hours.

Interestingly, the increase in transmittance in Figure 30 a) is most apparent at NIR wavelengths. This is attributed to a larger discrepancy in the transmittance behaviour of PbI_2 and MAPbI_3 at NIR wavelengths compared to visible and UV wavelengths. PbI_2 has a bandgap of 2.3 – 2.6 eV, resulting in the absorption of light with wavelengths less than 477 – 539 nm [122]. MAPbI_3 has a narrower bandgap of approximately 1.6 eV, with corresponding absorption at wavelengths less than 775 nm [3]. Consequently, as MAPbI_3 degrades to form PbI_2 , absorption at wavelengths less than ~ 550 nm remains high. Moreover, due to their bandgaps, neither material absorbs NIR light. Instead, increases in NIR transmittance with MAPbI_3 degradation are ascribed to an increase in porosity and the differences in reflectance of MAPbI_3 and PbI_2 . Above ~ 800 nm, MAPbI_3 has high reflectance [123], while PbI_2 has much lower reflectance [124]. According to optical principles, reflection of NIR light increases with conductivity [125, 99]. Since MAPbI_3 has a relatively high electrical conductivity that is 9 orders of magnitude larger than that of PbI_2 [126], a significant difference in the NIR reflectance behaviour of these two materials is expected. Furthermore, the decreases in transmittance around ~ 550 nm as MAPbI_3 degrades may be due to the formation of PbI_2 , which has a bandgap contributing to increased absorption.

The results indicate that oxygen and low humidity conditions alone are not sufficient to degrade the perovskite at the investigated time scale. Instead, the presence of UV light is necessary to induce degradation. In other words, it is concluded that UV light is principally responsible for degrading the perovskite in the present experiments. Furthermore, the findings justify the value of developing a PSC encapsulation that can reduce exposure of the perovskite layer to UV light.

6.3 Predicted Performance of UV-Protection Films

Based upon the analysis of the optical properties of TiO₂, ZnO and AZO thin films presented in Chapter 4, the materials may be ordered hierarchically in terms of their expected performance as UV-protection layers. Since the UV lamps employed herein irradiate light of wavelength 368 nm, the transmittance behaviour of each material at $\lambda = 368$ nm can be used to predict its ability to delay perovskite degradation. Materials with low $\lambda = 368$ nm transmittance will block a high percentage of UV light and be more effective at preventing photodegradation than their high-transmittance counterparts.

Figure 31 gives the $\lambda = 368$ nm transmittance of TiO₂, ZnO and AZO thin films deposited by PLD in 2, 5 and 20 mTorr O₂. ZnO films have significantly lower transmittance than TiO₂ and AZO; ZnO transmits less than 20% of light, while AZO and TiO₂ transmit upwards of 50 and 65%, respectively. Therefore, ZnO is predicted to be best at protecting perovskites from UV-induced degradation in the proposed experiments. Since the $\lambda = 368$ nm transmittance of ZnO changes insubstantially with PLD oxygen pressure, all ZnO films are expected to perform similarly. Conversely, TiO₂ and AZO exhibit significant changes in transmittance with oxygen pressure, where decreasing and increasing oxygen pressure is anticipated to improve degradation prevention, respectively.

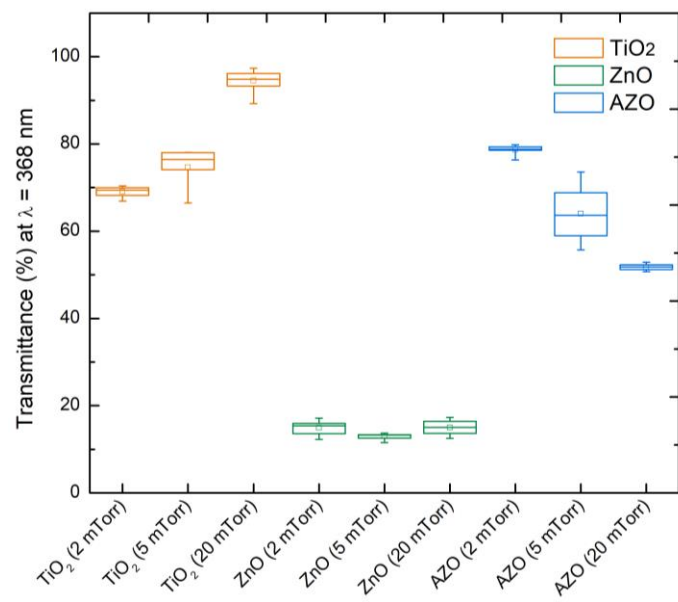


Figure 31: Percentage of 368 nm wavelength light transmitted by TiO₂, ZnO and AZO thin films deposited by PLD at 2, 5 and 20 mTorr O₂.

6.4 Results & Discussion

The efficacy of the TiO₂, ZnO and AZO UV-protection thin films deposited by PLD at 2, 5 and 20 mTorr O₂ was assessed by analyzing the appearance, transmittance and morphology of perovskite samples protected by said coatings during 8 hours of exposure to intense UV radiation. All results are compared to a control sample consisting of perovskite that is subject to the same radiation but not protected by a thin film layer.

6.4.1 Appearance

Degradation is first revealed in the appearance of a perovskite sample due to the characteristic yellow colour of the PbI₂ degradation product which is markedly different from the dark grey/black colour of pristine MAPbI₃. Figure 32 provides a means of comparing the appearance of perovskite samples protected by different thin film materials over the course of 8 hours of UV light exposure. Therein, the severity of degradation increases with the extent of the colour change from grey to yellow.

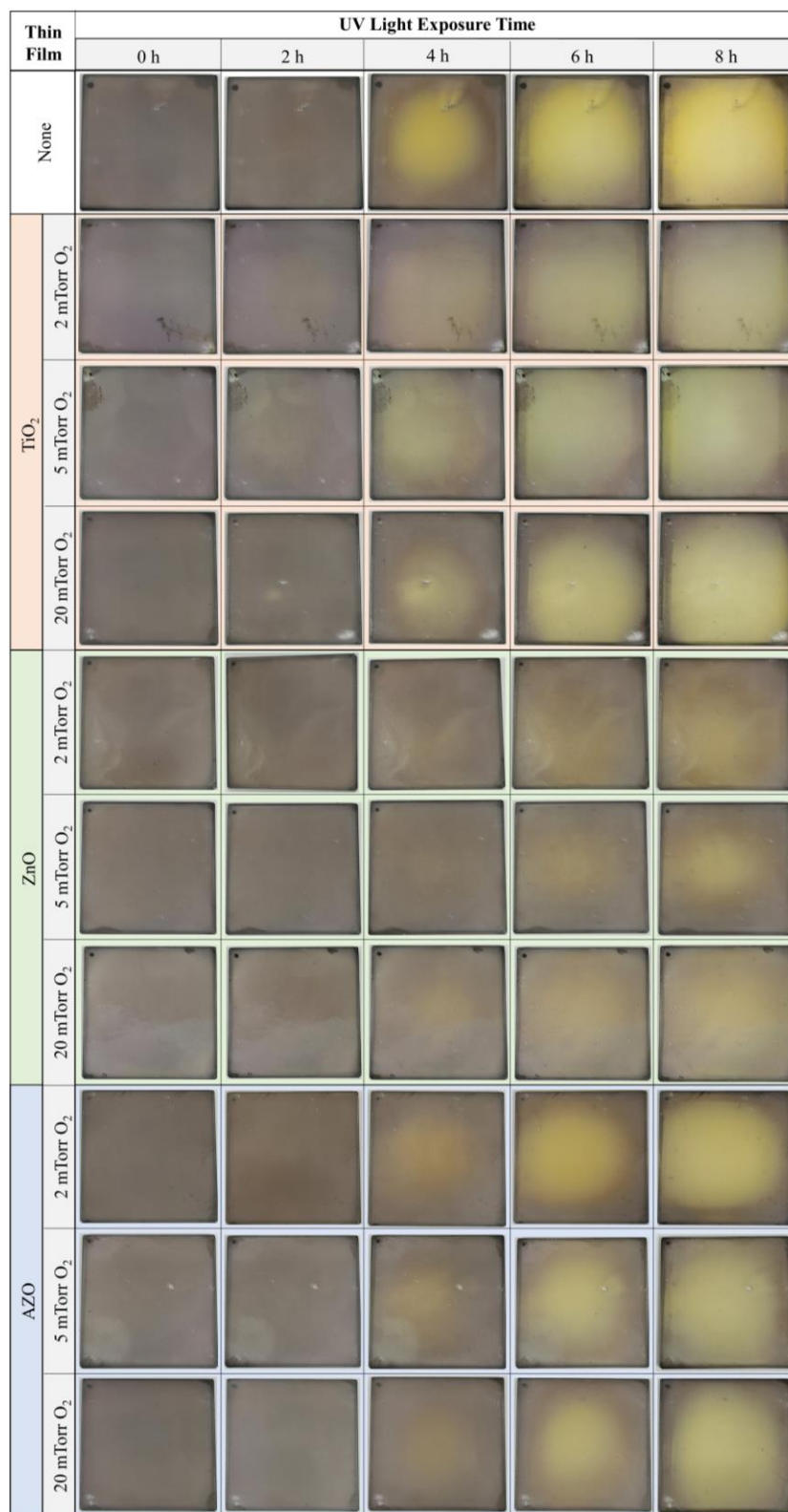


Figure 32: Camera images of thin film-protected perovskite samples exposed to UV light for 8 hours.

The first observation to note is that all perovskite samples protected by a thin film coating exhibit less colour change after 8 hours of UV radiation than the sample which was left unprotected. This finding establishes the merit in applying UV-protective films to prevent perovskite degradation. However, samples protected by thin films were not altogether absent of degradation indicators. Alternatively, the UV-protection thin films were found to delay the onset of degradation and reduce its severity to extents dependent on the composition and deposition pressure of the protective film. Nonetheless, delaying degradation by only a small amount in this accelerated aging experiment could result in significantly longer lifetimes under natural UV light intensities.

One material, in particular, emerges immediately as having most significantly prevented degradation: ZnO. In comparison to the unprotected perovskite sample which entirely transformed to have a bright yellow colour after 8 hours, the ZnO-protected samples show only minor yellowing concentrated around the center of the substrate. This non-uniformity in degradation is a result of the energy density reaching a maximum at the center of the lamp head and decaying radially as the light diffuses outward.

TiO₂ deposited at 20 mTorr O₂ and AZO deposited at 2 mTorr O₂ demonstrate the poorest propensities for inhibiting perovskite photodegradation. In fact, the perovskite samples protected by these thin films show only slightly less yellowing after 8 hours of UV aging than their unprotected counterpart. However, this result is in good agreement with the coating performances predicted in Figure 31, since these materials are expected to screen less than 20% of the incoming UV light.

Indeed, all of the colour change behaviour is in agreement with the material- and oxygen-dependent trends predicted in Figure 31: (1) ZnO outperforms TiO₂ and AZO; (2) all ZnO coatings perform similarly, regardless of oxygen pressure; (3) for TiO₂, degradation (i.e., intensity of yellow colour) increases with oxygen pressure, and; (4) for AZO, degradation decreases with oxygen pressure. Admittedly, the oxygen pressure dependencies of degradation are somewhat difficult to discern due to moderate differences in the percentage of light transmitted by TiO₂ and AZO deposited at varying oxygen pressures. For example, there is approximately a 30% difference in the amount of light transmitted by TiO₂ and

AZO coatings at their highest and lowest oxygen pressures. When these somewhat-limited differences in transmittance are compounded with experimental error, the trends in appearance and colour change may become slightly obscured.

6.4.2 Sources of Error

Three principal sources of experimental error were identified in conducting the degradation studies. Firstly, the use of three lamps limited the number of samples that could simultaneously undergo testing to three. Therefore, the degradation experiments spanned several weeks, giving rise to the potential for differences in the ambient testing environment (temperature, humidity, O₂ concentration, etc.) which could influence degradation rates. To mitigate this source of error, all experiments were conducted in a controlled-environment glovebox supplied with dry air. Nonetheless, ambient humidity and temperature were found to fluctuate by about 1% RH and 3°C, respectively. Secondly, the energy density of UV light was set using a coarse adjustment dial at the base of the lamps. Imprecision in the adjustment mechanism yielded a \pm error on the value of the energy density of approximately 10 mW/cm². Although this is more than double the intensity of UV light in the AM1.5 solar spectrum, it is unlikely to have major implications on the rate of degradation at the given time scale because it represents less than 5% of the energy density used for irradiation. In spite of that, the energy density was measured at all sampling intervals (i.e., at 0, 2, 4, 6 and 8 hours) and the dial adjusted to correction, when necessary. Thirdly, the spin coater reproducibility limits experimental error in that the rate of degradation is highly dependent on the presence of defects and thickness of the perovskite. The reproducibility of the spin coating method was evaluated in Section 6.1.1, and elucidated a relatively narrow distribution in the height of perovskite clusters across three samples. Nevertheless, some amount of error is expected due to the highly sensitive relationship between the rate of degradation and the thickness of the perovskite. Overall, the experimental methodology is considered sound because the results are in good agreement with the predicted performances.

6.4.3 Changes in Transmittance

While the appearance of perovskite samples provides a qualitative means of identifying degradation, the severity of the degradation is better quantified according to the transmittance behaviour of the perovskite. Since MAPbI_3 has strong reflection across the NIR spectrum while PbI_2 has much weaker reflection, a change in sample transmittance with UV exposure time suggests that the sample has degraded. Moreover, the magnitude of the change is indicative of the degree to which the sample is degraded. Figure 33, Figure 34 and Figure 35 give the transmittance spectra of perovskite samples subject to 8 hours of UV radiation under the protection of TiO_2 , ZnO and AZO thin films, respectively. Transmittance spectra were taken at 2 hour intervals over the course of the aging tests. While each sample was probed at 3 radial positions, the given graphs represent the transmittance at the center of the substrate, where the intensity of light is at its maximum.

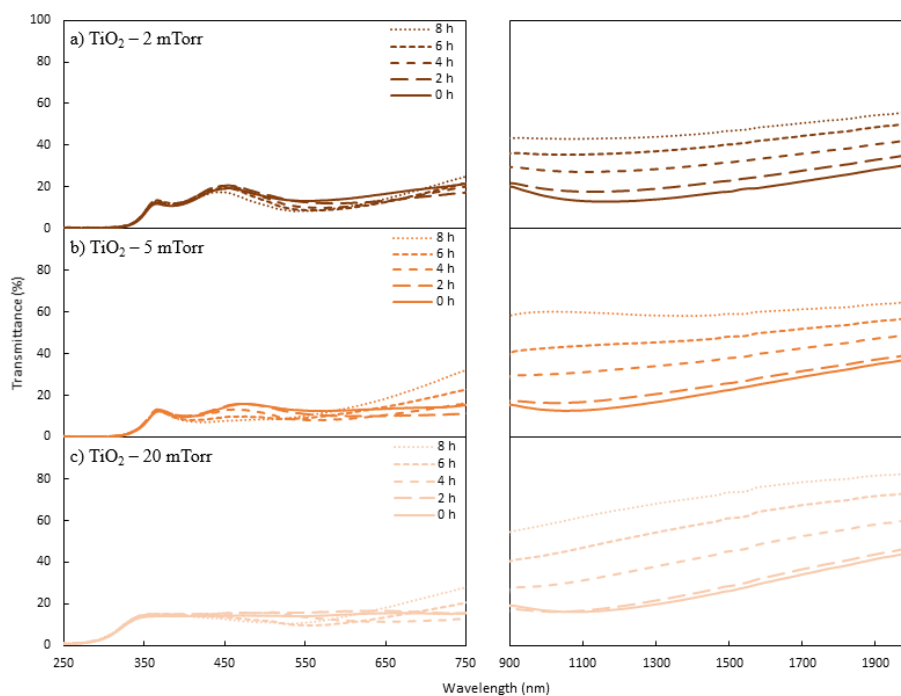


Figure 33: UV-Vis-NIR transmittance as a function of UV light exposure time of perovskite samples protected by TiO_2 thin films deposited at a) 2, b) 5, and c) 20 mTorr O_2 .

Figure 33 demonstrates fairly significant increases in transmittance with UV exposure time for all perovskite samples protected by TiO₂ thin films. Similar changes are evident in the spectra of the AZO-protected perovskite in Figure 35. However, Figure 34 reveals that the perovskite samples protected by ZnO experience much more modest increases in transmittance

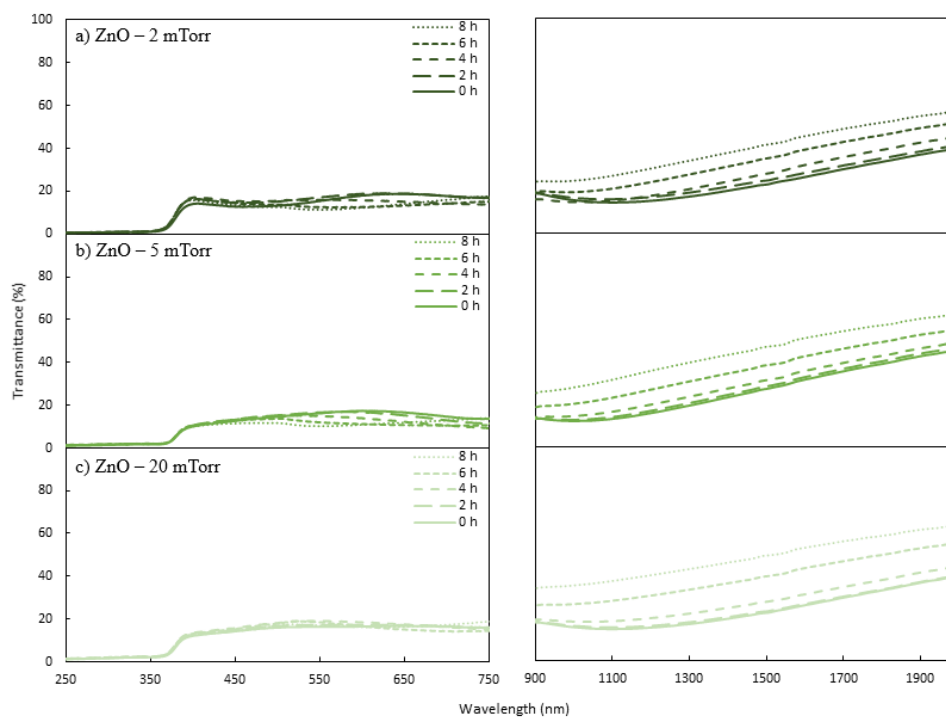


Figure 34: UV-Vis-NIR transmittance as a function of UV light exposure time of perovskite samples protected by ZnO thin films deposited at a) 2, b) 5, and c) 20 mTorr O₂.

In all Figures 33 - 35, the changes in transmittance are most apparent at NIR wavelengths due to the weak reflectance of the PbI₂ degradation product. It should also be noted that the visible-light portion of the transmittance spectra are reasonably different in appearance than the perovskite control samples given in Figure 30. This is a result of the metal oxide thin films deposited opposite the perovskite, which reduce the transmittance at UV wavelengths to near-zero. In fact, close inspection reveals that the absorption edges of the degraded samples perfectly match those of the metal oxide films to which they correspond in Figure 17. Importantly, the presence of the UV protection films does not affect the

discernment of degradation from the transmittance spectra because the metal oxide films are highly transparent through the visible and NIR regions. Where the films have slightly reduced transmittance, the magnitude of the perovskite sample transmittance will be similarly reduced. However, the changes in transmittance from UV exposure remain unaffected. Moreover, in many cases, the visible light transmittance actually appears to decrease with UV exposure time. This behaviour is explained by an increase in absorption due to the formation of the PbI_2 degradation product.

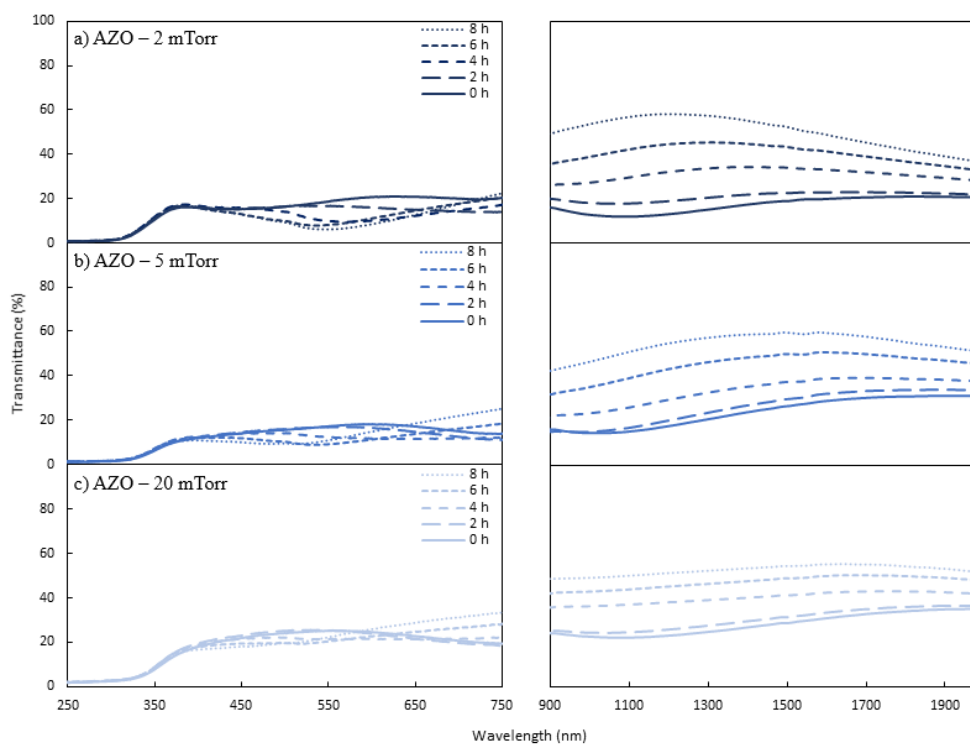


Figure 35: UV-Vis-NIR transmittance as a function of UV light exposure time of perovskite samples protected by AZO thin films deposited at a) 2, b) 5, and c) 20 mTorr O_2 .

A straightforward means of comparing the performance of the UV-protection thin films is obtained by determining the change in transmittance with UV exposure time. Since the most appreciable differences present at NIR wavelengths where metal oxide thin films are highly transparent and large differences in the transmittance behaviour of MAPbI_3 and PbI_2 exist, the calculation approximates the change in transmittance by taking the average change across three equidistant wavelengths in the NIR spectra. It should be noted that for

the purpose of the analysis, the arithmetic difference, and not the percent difference was taken, so as not to weigh changes at low transmittance more heavily than those at high transmittance. Finally, the changes in transmittance were normalized against the change in transmittance of the unprotected perovskite samples after 8 hours of UV radiation. Figure 36 provides the comparison of the normalized average change in NIR transmittance as a function of UV degradation time for samples protected by all TiO₂, ZnO and AZO thin films. Therein, the error is representative of differences between replicate samples, and does not reflect radial changes across each substrate due to the varying nature of light intensity with radial position.

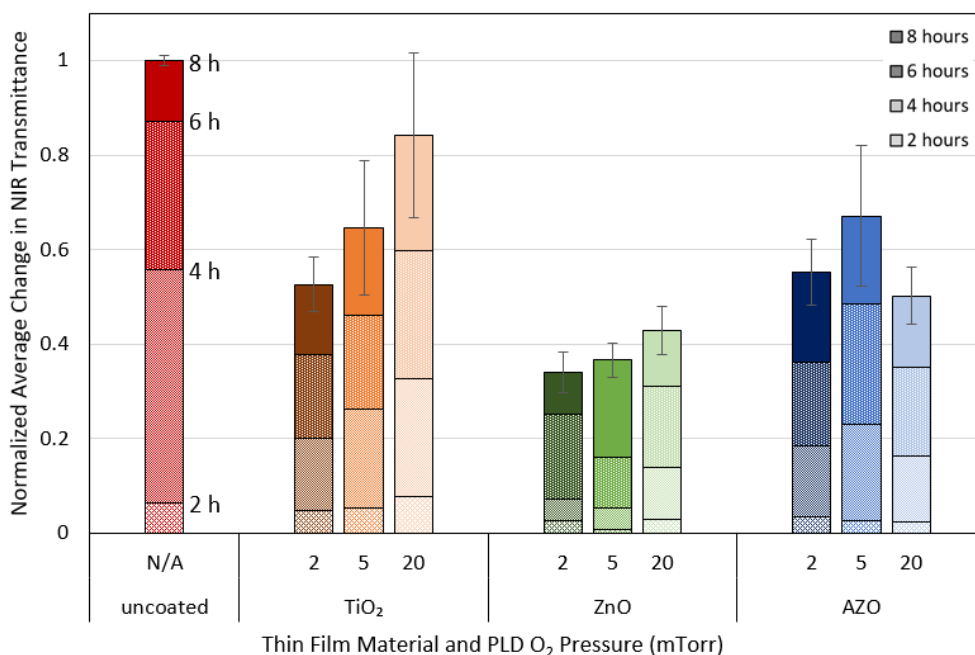


Figure 36: Normalized average change in NIR ($900 \text{ nm} < \lambda < 2000 \text{ nm}$) transmittance of thin film protected perovskite exposed to 8 hours of UV radiation.

For all samples, the rate of perovskite degradation is slow in the first two hours of UV radiation, as indicated by comparatively small changes in transmittance at this time interval. In the subsequent six hours, the rate increases and differences between protective coatings are exacerbated. Samples protected by TiO₂ thin films show variable transmittance changes depending on the oxygen pressure used for TiO₂ growth. For instance, changes in transmittance decrease dramatically from $84 \pm 17\%$ to $53 \pm 6\%$ of

the total changes exhibited by the unprotected perovskite, as the TiO₂ deposition pressure is reduced from 20 to 2 mTorr O₂. This trend is in good agreement with the expected performance based on the optical properties of TiO₂, which are influenced by the concentration of oxygen vacancies and Ti³⁺. The influence of charge carrier concentration on the absorption behaviour of AZO thin films is also demonstrated in the transmittance changes: broadly, there is a decrease in degradation severity with increasing O₂ deposition pressure. For AZO, maximal and minimal transmittance changes of $67 \pm 15\%$ and $50 \pm 6\%$ were experienced in samples with O₂ deposition pressures of 5 and 20 mTorr, respectively. Experimental error is responsible for smaller transmittance changes in the 2 mTorr sample than the 5 mTorr sample. The ZnO samples exhibit the most stable performance with varying O₂ pressure. Nonetheless, a slight increase in transmittance changes is observed with increasing O₂ pressure. For instance, transmittance changes of $34 \pm 4\%$ are reported for ZnO at 2 mTorr O₂, while a higher deposition pressure of 20 mTorr O₂ yields changes of $43 \pm 5\%$.

Overall, the analysis permits determination that ZnO thin films are most adept at preventing perovskite photodegradation. The best ZnO sample was grown by PLD in 2 mTorr O₂, and performs better than both the best TiO₂ and AZO protective coatings. By addition of the 2 mTorr ZnO coating, perovskite degradation – in terms of changes in transmittance behaviour – is reduced by approximately 66%. This reduction in degradation by more than half that of the unprotected sample represents a promising way to significantly delay photodegradation in perovskites and extend PSC lifetimes.

6.4.4 X-Ray Diffraction

XRD is another measurement tool that can be used to assess for the presence of degradation in perovskite samples exposed to UV light. Figure 37 gives the XRD spectra of thin film UV protection layer-coated and uncoated perovskite samples following 8 hours of accelerated UV aging. XRD was performed using the methodology previously described in Section 3.4. For the purpose of this analysis, only TiO₂, ZnO and AZO thin films deposited at 20 mTorr O₂ were considered because this pressure represents the condition where differences in optical properties are maximal. Furthermore, the degraded perovskite spectra are compared to that of a pristine sample which has not been exposed to UV light.

The pristine sample shows an intense diffraction peak at 14.3° and moderately intense peaks at 28.7° and 32.0° corresponding to the (110), (220), and (310) crystal planes of the tetragonal MAPbI_3 perovskite, respectively [127]. Less intense peaks at 20.2° , 23.7° and 24.8° are also related to MAPbI_3 [128].

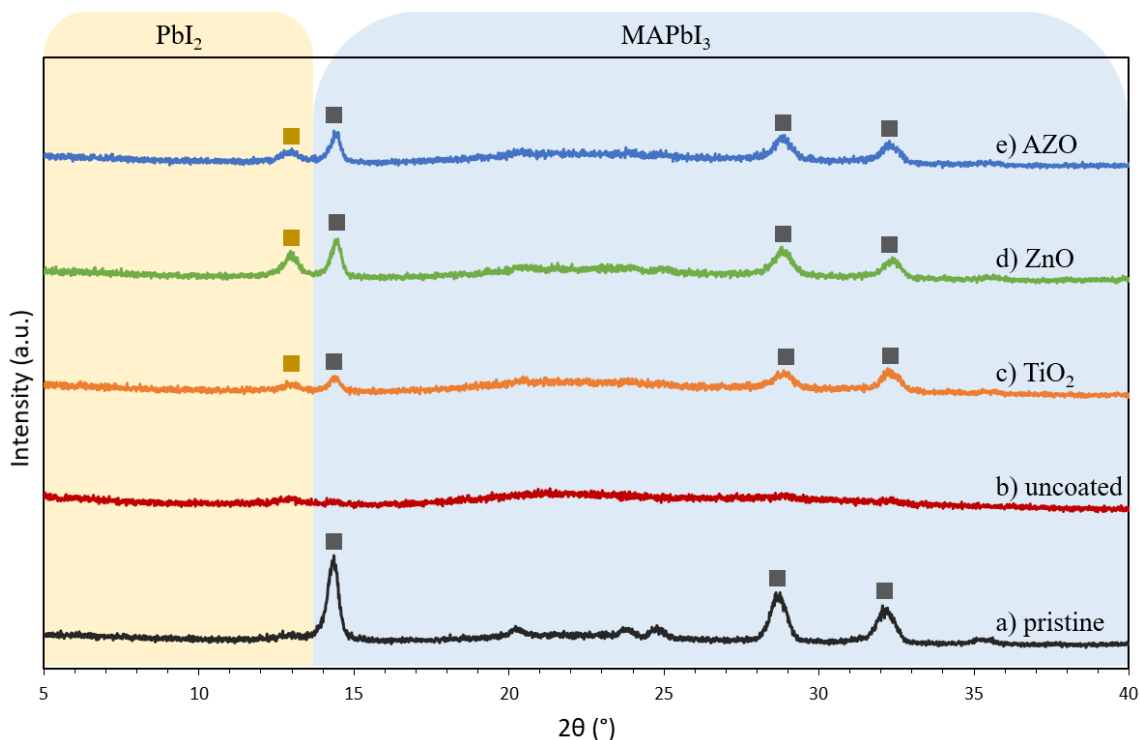


Figure 37: XRD patterns of MAPbI_3 perovskite b) without and with c) TiO_2 , d) ZnO , and e) AZO UV protection thin films deposited by PLD at 20 mTorr O_2 following 8 hours of UV radiation. The XRD pattern of a) pristine uncoated MAPbI_3 prior to UV radiation is shown for comparison.

Exposure of the uncoated sample to UV light results in a morphological change from crystalline to amorphous, as evidenced by the disappearance of discernable diffraction peaks in Figure 37 c). Addition of the thin film UV protection layers helps to prevent this change: Figure 37 demonstrates a clear decrease in the intensity of the MAPbI_3 peak at 14.3° , indicating a decrease in crystallinity but not a full transformation to the amorphous phase. This suggests that all coated samples are less degraded than their uncoated counterpart. Furthermore, degradation of the protected samples reveals a new peak at 13.0° , for which PbI_2 is responsible [20]. The finding reveals that degradation of MAPbI_3 first

precipitates a crystalline PbI_2 phase, followed by a transformation to the amorphous phase as degradation continues to completion. The coatings can thereby be classified according to their ability to prevent degradation based upon the intensities of the 13.0° PbI_2 and 14.3° MAPBI_3 peaks: the greater the intensity of the peaks, the higher the crystallinity of the film and the less degradation to which it has succumbed. Consequently, ZnO is the superior photoprotection coating, followed by AZO then TiO_2 . This conclusion is in good agreement with the absorption behaviour of each of the thin film materials as well as the previously surmised results on changes in colour and transmittance.

6.5 Projected Effectiveness in Solar Cells

In this study, samples were irradiated with 368 nm monochromatic UV light to simulate an accelerated form of the degradation they might experience under ambient solar light. In reality, the AM1.5 spectrum contains UV light with wavelengths from 260 – 400 nm. As a result, one might argue that the thin film which provides the best protection against degradation under 368 nm UV light might be less well-suited to providing protection against degradation arising from the AM1.5 spectral UV light. However, the degradation experiments conducted herein revealed that the 368 nm transmittance of TiO_2 , ZnO and AZO thin films was entirely able to predict photoprotective performance. That is to say, the thin film which exhibited the lowest transmittance at 368 nm also provided the best protection against degradation. It would therefore similarly be expected that the thin films which have the lowest transmittance across all UV wavelengths of light would be most effective for preventing perovskite photodegradation under ambient solar irradiation. These metrics were previously determined in Figure 20 by calculating the percentage of UV-A and UV-B light irradiated by the Sun that is absorbed and reflected by each of the TiO_2 , ZnO and AZO thin films. It revealed an identical trend to what was obtained in the degradation experiments under 368 nm irradiation. Importantly, ZnO remains the material expected to provide superior protection to perovskite degradation under AM1.5 solar light. This assessment relies on the assumption that all UV wavelengths of light have the same ability to catalyze degradation. In reality, shorter wavelengths of light represent higher energy photons which will contribute to elevated rates of degradation [13]. Nonetheless, since most of the thin film materials exhibited very strong UV-B absorption, and that

differences in absorption between materials emerged primarily in a narrow region of the UV-A range, the assumption is considered to be of negligible consequence.

Additionally, resource limitations of the present study did not permit evaluation of the developed photoprotective coatings in encapsulations for perovskite solar cells. Nonetheless, it is expected that the photoprotective coating that delays perovskite degradation most significantly in this work will also provide the most protection against UV-induced degradation in perovskite solar cells. In other words, the material which is able to screen the most UV light without compromising visible light transmittance, will be most suited to PSC encapsulation. Based on the current analysis, ZnO was identified as being the most promising candidate material for the encapsulation application.

Recent research on the stability of PSCs has found that adjacent materials in the solar stack, such as the charge transport layers, can participate in perovskite degradation mechanisms. In fact, a prevalent form of UV-induced degradation in PSCs originates in the metal oxide charge transport layer, where photoexcitation yields reactive superoxide species which can cause rapid photo-oxidative degradation of the adjacent perovskite layer [8]. In order to provide a better projection as to the effectiveness of the ZnO photoprotective films in combatting the additional degradation mechanisms that arise in the presence of charge transport layers, a porous TiO₂ layer, which mimics the most commonly used electron transport layer (ETL) in PSCs, was added adjacent to the perovskite in the present degradation studies.

6.5.1 Addition of a TiO₂ ETL

A 50 nm TiO₂ ETL mimic layer was deposited by PLD (Section 3.1) on the quartz substrate prior to deposition of the perovskite by spin coating. An oxygen pressure of 54 mTorr was used for the deposition in order to obtain a porous film which resembles the mesoporous TiO₂ ETL commonly used in PSCs. Figure 38 demonstrates the positioning of the TiO₂ layer between the perovskite and quartz substrate, such that, upon irradiation, any UV light not screened by the UV-protection film will first pass through the TiO₂ layer before it reaches the perovskite underneath. All samples were degraded under 8 hours of 230

mW/cm² UV light, according to the previously described methodology. Where a ZnO UV-protection film was included, the ZnO was deposited by PLD at 20 mTorr O₂.

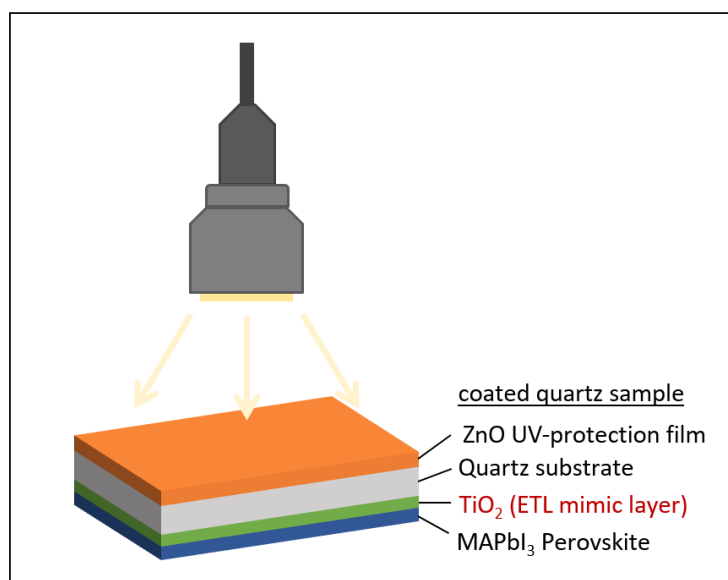


Figure 38: An enlarged view of the irradiated coated quartz sample layer configuration with addition of a TiO₂ layer that mimics the electron transport layer in PSCs. Note that this schematic is not to-scale.

Camera images taken at 2 hour intervals over the course of 8 hours of UV radiation are given in Figure 39 and reveal the rapid nature of the photo-oxidative degradation in the presence of TiO₂. For example, the onset of yellowing in the unprotected sample with TiO₂ occurred prominently after only 2 hours of radiation, compared to an onset at 4 hours for the sample that did not include TiO₂. Additionally, yellowness after 8 hours was more severe in the sample with TiO₂. Identical observations can be made with regards to the inclusion or exclusion of TiO₂ in the ZnO-protected perovskite samples.

In order to assess the efficacy of the ZnO protective coatings in the presence of a TiO₂ ETL, the camera images of the ZnO-protected sample are compared to their unprotected counterparts. The images demonstrate that by inclusion of the ZnO protection layer, the onset of yellowing is delayed by 2 hours. However, after 8 hours of UV exposure, the perovskite has yellowed severely. Nonetheless, regions of unchanged colour remain at the edges of the quartz substrate (where the energy density of UV light is reduced), indicating

that the ZnO coating continues to provide some protection even after subjection to 8 hours of harsh UV conditions.

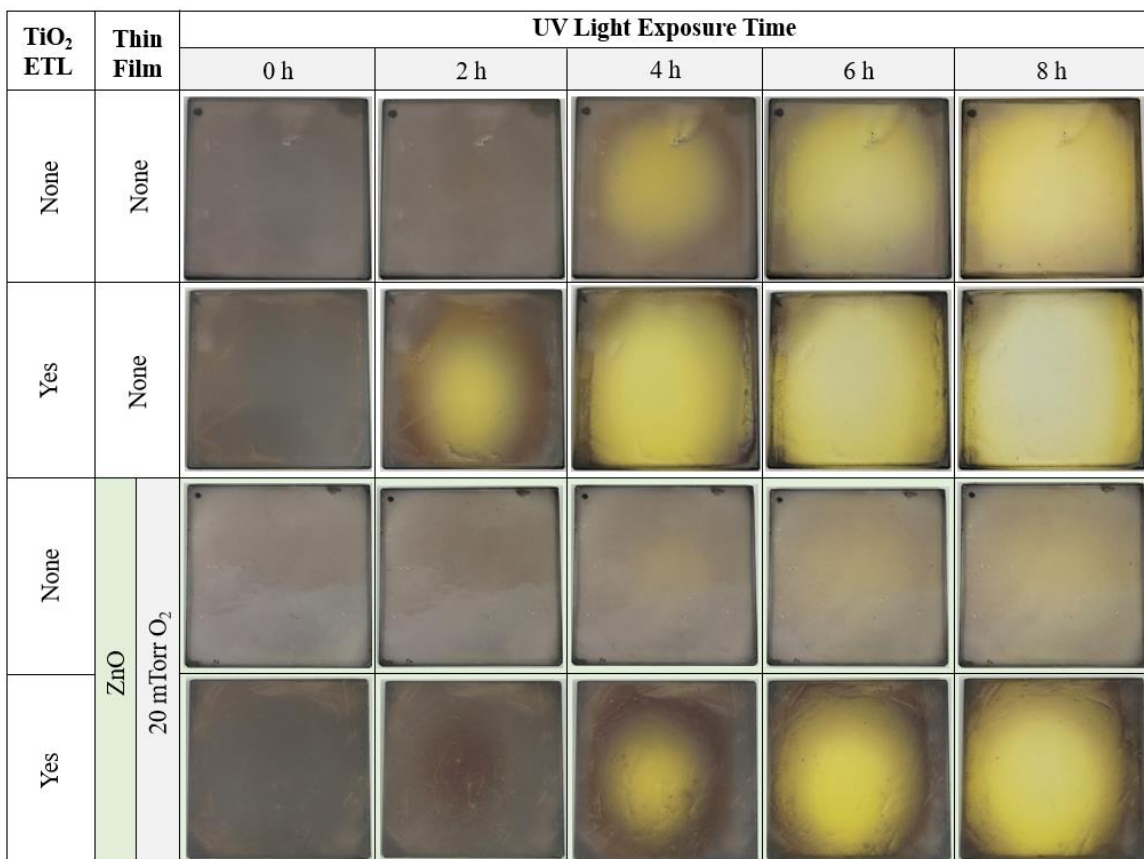


Figure 39: Camera images of ZnO-protected perovskite samples with a TiO₂ ETL after 8 hours of UV radiation. For comparison, images of samples degraded without TiO₂ ETLs and/or thin UV-protection films are also provided.

To better quantify the degradation in the samples with perovskite adjacent to TiO₂, UV-Vis-NIR spectra were taken and the normalized average change in NIR transmittance was computed. Figure 40 presents a summary of the results.

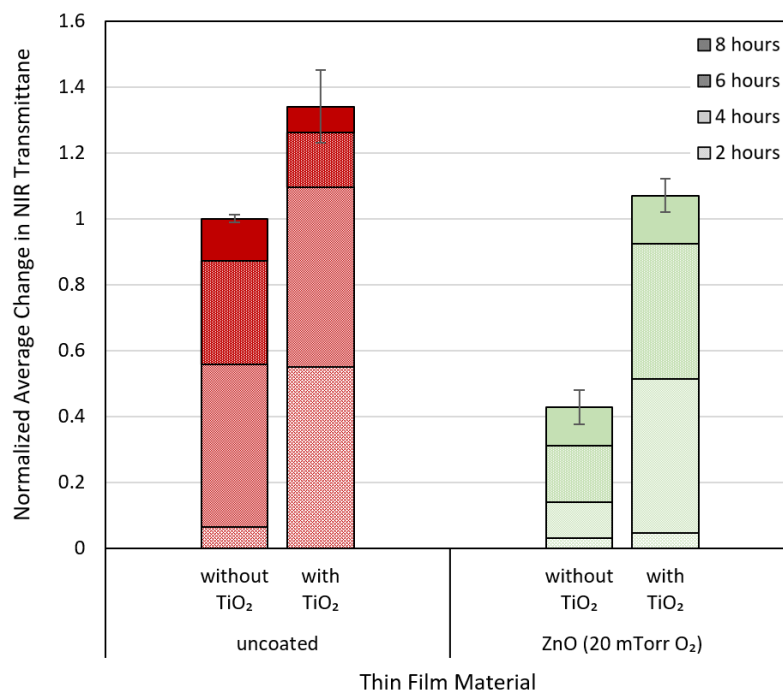


Figure 40: Normalized average change in NIR ($900 \text{ nm} < \lambda < 2000 \text{ nm}$) transmittance of uncoated and ZnO-protected perovskite with and without a TiO₂ ETL after 8 hours of UV exposure.

The data clearly demonstrates that by inclusion of the TiO₂ ETL, increases in transmittance are greater than when it had been excluded. For instance, the unprotected and ZnO-protected samples exhibit transmittance changes which increase by a factor of approximately 1.35 and 2.5, respectively with the deposition of TiO₂ adjacent to the perovskite. Evidently, the addition of TiO₂ seems to have more significantly impacted degradation with a ZnO protection layer. However, closer inspection reveals an issue with the length of UV exposure time in drawing comparative conclusions between the protected and unprotected samples.

Theoretically, the rate of degradation is expected to increase at the beginning of UV exposure. Then, with time, the degradation rate should slow, as MAPbI₃ is converted to PbI₂ and the surface area of exposed MAPbI₃ decreases. Eventually, degradation must stop altogether because once all of the MAPbI₃ has reacted to form PbI₂, the perovskite cannot continue to degrade. By noting that the rate of degradation is proportional to the magnitude

of transmittance changes, Figure 40 demonstrates that the rate of degradation is slow at the beginning of UV radiation and increases after 2 hours. As degradation proceeds, its rate decreases. However, in the case of the unprotected perovskite with TiO₂ ETL, degradation nears completion after only 4 hours of UV radiation and slows dramatically thereafter; additional transmittance changes between hours 4 and 8 of the experiment are limited, as the upper threshold of transmittance is approached. Therefore, an assessment of the efficacy of the ZnO protective coating after 8 hours of UV exposure cannot be made in comparison to its unprotected counterpart because the protected sample was allowed to degrade an additional 4 hours after the point at which the unprotected sample had nearly finished degrading. Instead, more informative conclusions as to the effectiveness of ZnO in delaying degradation are drawn after 4 hours of UV radiation. At this point, the protected and unprotected samples exhibit transmittance changes of $51 \pm 5\%$ and $109 \pm 11\%$, respectively. In other words, the protected sample experiences less than half of the changes in transmittance of the unprotected sample. Therefore, while the addition of a TiO₂ ETL certainly accelerates degradation of the perovskite, protection with ZnO thin films still constitutes an effective strategy in significantly improving stability and extending PSC lifetimes.

It is also important to note that this study has intentionally selected MAPbI₃ as the perovskite for degradation experiments because it is the most readily degradable perovskite material, and therefore provides a means of easily assessing changes in stability. However, significant progress in intrinsic stabilization has found alternative perovskite materials, such as those with X-site and A-site substitutions, which exhibit slower rates of degradation. While these findings are promising, there remains to be a perovskite material proposed that demonstrates adequate stability in outdoor environments over the long-term. Therefore, it is clear that a combination of intrinsic stabilization and encapsulation strategies will be necessary for PSC commercialization. Similarly, the perovskite precursor solution and spin coating technique employed in this work produced a perovskite layer consisting of distinct aggregates of MAPbI₃ crystals with significantly higher surface area than what would be obtained in PSCs that use more conventional monolithic perovskite layers. Therefore, in the present study, the high surface area of MAPbI₃ exposed to UV light permitted a more accelerated form of degradation than what might be observed in

monolithic PSCs. The degradation experiments conducted herein, revealed a failure of the MAPbI₃ perovskite after only a few hours of accelerated UV aging. Importantly, while this is not sufficient for commercialization purposes, it is representative of the much longer operational lifetimes of intrinsically stabilized monolithic perovskites, which stand, equally, to benefit from the photoprotection of thin UV-absorption films.

6.6 Conclusions

A series of experiments were performed to evaluate the degree to which the TiO₂, ZnO and AZO thin protective films could delay photodegradation in perovskites. Irradiation of perovskite samples with high energy density UV-A light found significant UV-induced degradation, establishing the importance of PSC encapsulations which target UV light impermeability. Degradation of MAPbI₃ to PbI₂ was observed in the form of a colour change from grey to yellow and an increase in NIR transmittance. All perovskite samples protected by metal oxide thin films were less severely degraded after 8 hours of UV radiation than their unprotected counterparts. However, significant differences in the ability of the thin films to prevent degradation were observed and were found to correlate with the inherent optical properties of each material. These differences were quantified according to changes in sample transmittance. Samples with TiO₂ protective films exhibited increasingly severe degradation with increasing PLD oxygen pressure. Conversely, AZO-protected samples showed a decreasing severity of degradation with increasing PLD oxygen pressure. Yet, regardless of oxygen pressure, the ZnO protective coatings were most effective in preventing perovskite photodegradation. After 8 hours of UV radiation, ZnO-protected samples exhibited only minimal yellowing and experienced transmittance changes of less than $43 \pm 5\%$ compared to the unprotected sample. These trends were found to be in good agreement with the efficacies predicted based upon the effect of material and oxygen growth environment on UV absorption. XRD analysis was used to identify the formation of PbI₂ upon UV exposure and found a transformation from the crystalline to amorphous phase with complete degradation. Finally, TiO₂ was deposited adjacent to the perovskite layer to replicate the photo-oxidative degradation mechanisms that exist in PSCs with TiO₂ ETLs. Even under this accelerated form of UV-induced degradation, the ZnO protective coatings still proved effective, limiting increases in

transmittance after 4 hours of UV radiation to only $47 \pm 7\%$ of those experienced by the unprotected sample. Therefore, the presented strategy, which employs a ZnO thin film for UV-protection, is promising for use in PSC encapsulations and has the potential to significantly extend device lifetimes.

Chapter 7

7 Conclusions and Recommendations

A summary of the current status of perovskite solar cell encapsulation research was presented. It found that significant efforts have focused on addressing the oxygen- and water- induced degradation of perovskites through glass-to-glass, polymer, thin film and hybrid encapsulation strategies. However, most encapsulation techniques left the perovskite vulnerable to photodegradation. Therefore, this work was motivated in bridging the gap towards photostability in order to extend the lifetimes and thereby the commercial viability of perovskite solar cells.

The use of stable, inorganic metal oxide thin films with bandgaps suited to absorbing UV light was identified as a means of preventing UV-induced degradation in perovskites. Consequently, thin films of TiO₂, ZnO and AZO were deposited at room-temperature by the highly-uniform, pulsed laser deposition technique. Moreover, as a result of its influence on the absorptive behaviour of the materials, the oxygen partial pressure in the deposition environment was varied between 2, 5 and 20 mTorr. It was found that all thin films were highly transparent to visible light but that those deposited at high O₂ pressure tended to be slightly more colourless. XPS analysis revealed the formation of Ti³⁺ ions in the TiO₂ films and provided evidence for an increased concentration of oxygen vacancies in the TiO₂, ZnO and AZO films deposited at low O₂ pressure. The oxygen growth environment was also found to impact the film morphology, with increased thin film density observed by FESEM at lower oxygen pressures. Finally, XRD determined that under the present deposition conditions, ZnO and AZO films were crystalline in nature, while TiO₂ was amorphous.

Subsequently, the relationship between the oxygen deposition pressure and optical properties of TiO₂, ZnO and AZO thin films was elucidated. Interference reflectometry and UV-Vis-NIR spectroscopy found that the optical properties of TiO₂ and AZO thin films were sensitive to variations in oxygen pressure. In TiO₂, the formation of defect states contributed to narrowing the bandgap, while in AZO, the Burstein-Moss effect applies, such that a widening of the bandgap is observed for increasing carrier concentration. As a

result, the absorption edges of TiO₂ and AZO thin films were noticeably blueshifted and redshifted, respectively, with increasing O₂ deposition pressure. Conversely, the optical properties of the ZnO films were much more stable under the investigated conditions. To evaluate the suitability of the thin films for perovskite solar cell photoprotection, the percentage of UV and visible light absorbed by each coating was determined. At their respective optimal oxygen pressures of 2, 5 and 20 mTorr, TiO₂, ZnO and AZO thin films were maximally able to block $52.30 \pm 2.72\%$, $72.13 \pm 3.05\%$, and $52.06 \pm 2.20\%$ of UV-A light. The same deposition conditions produced TiO₂, ZnO and AZO coatings which absorbed/reflected $24.79 \pm 1.91\%$, $8.05 \pm 0.75\%$, and $6.25 \pm 0.60\%$ of visible light. Therefore, as a result of its superior ability to screen UV light without significantly sacrificing visible light transparency, ZnO was identified as the most promising material for the encapsulation application.

Additionally, since the typical solar panel operating environment demands mechanical durability and chemical stability, the adhesion, abrasion resistance and chemical resistance of each thin film was evaluated. All of the tested materials exhibited excellent adhesion, and passed the chemical solubility and cleanability tests. While AZO demonstrated the best abrasion resistance, all materials were deemed sufficiently durable for use as photoprotective coatings.

Next, the photoprotective quality of the thin films was assessed by irradiating perovskite samples with ultra-high energy density UV-A light (230 mW/cm^2) through all combinations of thin film materials and oxygen pressures. Samples with TiO₂ and AZO protective coatings exhibited increasingly and decreasingly severe degradation, respectively, with increasing PLD oxygen pressure. However, all ZnO protective coatings, regardless of oxygen pressure, were more effective in preventing perovskite photodegradation than either of the best TiO₂ or AZO samples. For instance, after 8 hours of UV radiation, the best TiO₂-, ZnO-, and AZO-protected samples exhibited transmittance changes of $53 \pm 6\%$, $34 \pm 6\%$, and $50 \pm 6\%$, respectively, compared to the unprotected sample. Accompanied by only minimal yellowing after 8 hours of UV exposure, the 2 mTorr ZnO sample was thereby determined to be most adept at preventing UV-induced degradation in perovskites. Finally, a photoactive TiO₂ layer was deposited adjacent to the

perovskite in order to better replicate the photo-oxidative degradation mechanisms in perovskite solar cell stacks. Even under this highly accelerated form of UV-induced degradation, the ZnO protective coatings still proved effective, limiting increases in transmittance to only $47 \pm 7\%$ of those experienced by the unprotected sample. Therefore, ZnO thin films grown by pulsed laser deposition at oxygen pressures between 2 and 20 mTorr demonstrate tremendous promise and are considered to be the most suitable of the investigated materials for extending the lifetimes of perovskite solar cells.

A number of recommendations were identified in conducting the present analysis that represent avenues for future improvement and further research. Firstly, previous work in inorganic thin films has demonstrated horizontal translations of the absorption edge with increasing film thickness. At present, all thin protective films were deposited with thicknesses of 200 nm in order to control for the effect of thickness on absorption. This thickness was selected to produce thin films that exhibit complete absorption of light at wavelengths less than their absorption edge. However, optimization of thin film thickness represents an opportunity for further tuning of the absorption behaviour and potentially better photoprotective performance.

Secondly, resource limitations did not permit encapsulating perovskite solar cells to see how their efficiency and performance changes with UV light exposure. Evidently, this is vital to evaluate whether the photoprotective thin films will function as anticipated. Furthermore, it would permit assessment of the degree to which losses in visible light due to absorption/reflection of the thin films might compromise power conversion efficiencies. Therefore, testing of the proposed encapsulations with real solar cells is a top priority for future work.

Thirdly, while the UV-protection films are currently envisaged for use in hybrid thin film/glass encapsulations, they may also be applied directly to the solar stack or as hybrid thin film/polymer encapsulations in order to retain device flexibility and roll-to-roll compatibility. With the elimination of glass as a component of the encapsulation, the WVTR and OTR of the thin films are called into question. Therefore, future work should look to evaluate the WVTR and OTR of thin films grown in various pulsed laser deposition

environments, such that compatibility of the proposed strategy with flexible devices may be established.

Finally, this work confirmed that perovskites degrade rapidly and severely upon exposure to UV light with an energy density 50 times more intense than that of the UV light in the AM1.5 solar spectrum. However, it would be interesting to determine how quickly the same samples might degrade under normal UV light intensities, and whether the photoprotective coatings remain effective in substantially extending lifetimes under more natural conditions. Moreover, a comparison of the degree to which UV light, water, oxygen and heat are responsible alone and in combination for inducing perovskite degradation could provide insight into where future encapsulation efforts should be principally focused. For example, determining the factors by which water- and oxygen- induced degradation are accelerated by UV light, and whether these forms of degradation might be slowed via the addition of photoprotective films, could further justify the incorporation of UV-screening materials in perovskite solar cell encapsulations.

References

- [1] "Best Research-Cell Efficiency Chart," National Renewable Energy Laboratory (NREL), 2022. [Online]. Available: <https://www.nrel.gov/pv/cell-efficiency.html>. [Accessed 27 05 2022].
- [2] Z. Liu, L. Kruckemeier, B. Krogmeier, B. Klingebiel, J. A. Marquez, S. Levchenko, S. Oz, S. Mathur, U. Rau, T. Unold and T. Kirchartz, "Open-circuit voltages exceeding 1.26 V in planar methylammonium lead iodide perovskite solar cells," *ACS Energy Letters*, vol. 4, no. 1, pp. 110-117, 2019.
- [3] N. G. Park and H. Segawa, "Research direction toward theoretical efficiency in perovskite solar cells," *ACS Photonics*, vol. 5, no. 8, pp. 2970-2977, 2018.
- [4] N. G. Park, "Halide perovskite photovoltaics: history, progress, and perspectives," *MRS Bulletin*, vol. 43, pp. 527-533, 2018.
- [5] J. Gong, S. Darling and F. You, "Perovskite photovoltaics: Life-cycle assessment of energy and environmental impacts," *Energy & Environmental Science*, vol. 8, pp. 1953-1968, 2015.
- [6] Z. Song, C. McElvany, A. Phillips, I. Celik, P. Krantz, S. Watthae, G. Liyanage, D. Apul and M. Heben, "A techno-economic analysis of perovskite solar module manufacturing with low-cost materials and techniques," *Energy & Environmental Science*, vol. 10, pp. 1297-1305, 2017.
- [7] H. J. Snaith, "Present status and future prospects of perovskite photovoltaics," *Nature Materials*, vol. 10, pp. 372-376, 2018.

- [8] C. Boyd, R. Cheacharoen, T. Leijtens and M. McGehee, "Understanding degradation mechanisms and improving stability of perovskite photovoltaics," *Chemical Reviews*, vol. 119, pp. 3418-3451, 2019.
- [9] J. H. Noh, S. H. Im, T. N. Mandal and S. I. Seok, "Chemical management of colourful, efficient, and stable inorganic-organic hybrid nanostructured solar cells," *Nano Letters*, vol. 13, no. 4, pp. 1764-1769, 2013.
- [10] J. S. Yun, J. Kim, T. Young, R. J. Pattersn, D. Kim, J. Seidel, S. Lim, M. A. Green, S. Huang and A. Ho-Baillie, "Humidity-induced degradation via grain boundaries of HC(NH₂)₂PbI₃ planar pervoskite solar cells," *Advanced Functional Materials*, vol. 28, no. 11, p. 1705363, 2018.
- [11] Q. Wang, B. Chen, Y. Liu, Y. Deng, Y. Bai, Q. Dong and J. Huang, "Scaling behaviour of moisture-induced grain degradation in polycrystalline hybrid perovskite thin films," *Energy & Environmental Science*, vol. 10, pp. 516-522, 2017.
- [12] J. Gong, M. Yang, D. Rebollar, J. Rucinski, Z. Liveris, K. Zhu and T. Xu, "Divalent anionic doping in perovskite solar cells for enhanced chemical stability," *Advanced Materials*, vol. 30, no. 34, p. 1800973, 2018.
- [13] A. Farooq, I. M. Hossain, S. Moghadamzadeh, J. A. Schwenzler, T. Abzieher, B. S. Richards, E. Klampaftis and U. W. Paetzold, "Spectral dependence of degradation under ultraviolet light in perovskite solar cells," *ACS Applied Material Interfaces*, vol. 10, no. 26, pp. 21985-21990, 2018.
- [14] G. Y. Kim, A. Senocrate, T.-Y. Yang, G. Gregori, M. Gratzel and J. Maier, "Large tunable photoeffect on ion conduction in halide perovskites and implications for photodecomposition," *Nature Materials*, vol. 17, pp. 445-449, 2018.

- [15] N. H. Nickel, F. Lang, V. V. Brus, O. Shargaieva and J. Rappich, "Unraveling the light-induced degradation mechanisms of CH₃NH₃PbI₃ perovskite films," *Advanced Electronic Materials*, vol. 3, no. 12, p. 1700158, 2017.
- [16] W. Li, W. Zhang, S. Van Reenen, R. J. Sutton, J. Fan, A. A. Haghighirad, M. B. Johnston, L. Wang and H. J. Snaith, "Enhanced UV-light stability of planar heterojunction perovskite solar cells with caesium bromide interface modification," *Energy and Environmental Science*, vol. 9, pp. 490-498, 2016.
- [17] B. Roose, J.-P. Baena, K. C. Godel, M. Graetzel, A. Hagfeldt, U. Steiner and A. Abate, "Mesoporous SnO₂ electron selective contact enables UV-stable perovskite solar cells," *Nano Energy*, vol. 30, pp. 517-522, 2016.
- [18] M. M. Tavakoli, F. Giordano, S. M. Zakeeruddin and M. Gratzel, "Mesoscopic oxide double layer as electron specific contact for highly efficient and UV stable perovskite photovoltaics," *Nano Letters*, vol. 18, no. 4, pp. 2428-2434, 2018.
- [19] Q. Jiang, X. Zhang and J. You, "SnO₂: A wonderful electron transport layer for perovskite solar cells," *Small*, vol. 14, no. 31, p. 1801154, 2018.
- [20] M. Ouafi, B. Jaber, L. Atourki, R. Bekkari and L. Laanab, "Improving UV stability of MAPbI₃ perovskite thin films by bromide incorporation," *Journal of Alloys and Compounds*, vol. 746, pp. 391-398, 2018.
- [21] M. I. Saidaminov, J. Kim, A. Jain, R. Quintero-Bermudez, H. Tan, G. Long, F. Tan, A. Johnston, Y. Zhao, O. Voznyy and E. Sargent, "Suppression of atomic vacancies via incorporation of isovalent small ions to increase the stability of halide perovskite solar cells in ambient air," *Nature Energy*, vol. 3, pp. 648-654, 2018.
- [22] C. Chen, H. Li, J. Jin, X. Chen, Y. Cheng, Y. Zheng, D. Liu, L. Xu, H. Song and Q. Dai, "Long-lasting nanophosphors applied to UV-resistant and energy storage

- perovskite solar cells," *Advanced Energy Materials*, vol. 7, no. 20, p. 1700758, 2017.
- [23] T. Song, X. Feng, H. Ju, T. Fang, F. Zhu, W. Liu and W. Huang, "Enhancing acid, base and UV light resistance of halide perovskite $\text{CH}_3\text{NH}_3\text{PbBr}_3$ quantum dots by encapsulation with ZrO_2 sol," *Journal of Alloys and Compounds*, vol. 816, p. 152558, 2020.
- [24] Q. Dong, Y. Shi, C. Zhang, Y. Wu and L. Wang, "Energetically favored formation of SnO_2 nanocrystals as electron transfer layer in perovskite solar cells with high efficiency exceeding 19%," *Nano Energy*, vol. 40, pp. 336-344, 2017.
- [25] B. Conings, J. Drijkoningen, N. Gauquelin, A. Babayigit, J. D'Haen, L. D'Olieslaeger, A. Ethirajan, J. Verbeeck, J. Manca, E. Mosconi, F. De Angelis and H.-G. Boyen, "Intrinsic thermal instability of methylammonium lead trihalide perovskite," *Advanced Energy Materials*, vol. 5, no. 15, p. 1500477, 2015.
- [26] S.-H. Turren-Cruz, A. Hagfeldt and M. Saliba, "Methylammonium-free, high-performance, and stable perovskite solar cells on a planar architecture," *Science*, vol. 362, no. 6413, pp. 449-453, 2018.
- [27] C. Liu, W. Li, C. Zhang, Y. Ma, J. Fan and Y. Mai, "All-inorganic CsPbI_2Br perovskite solar cells with high efficiency exceeding 13%," *Journal of the American Chemical Society*, vol. 140, no. 11, pp. 3825-3828, 2018.
- [28] A. J. Yun, J. Kim, B. Gil, H. Woo, K. Park, J. Cho and B. Park, "Incorporation of lithium fluoride restraining thermal degradation and photodegradation of organometal halide perovskite solar cells," *Energy & Environmental Science*, vol. 12, no. 45, pp. 50418-50425, 2020.
- [29] G. Griffini and S. Turri, "Polymeric materials for long-term durability of photovoltaic systems," *Journal of Applied Polymer Science*, vol. 133, no. 11, p. 43080, 2015.

- [30] S. Cros, R. de Bettignies, S. Berson, S. Bailly, P. Maisse, N. Lemaitre and S. Guillerez, "Definition of encapsulation barrier requirements: A method applied to organic solar cells," *Solar Energy Materials and Solar Cells*, vol. 95, pp. S65-S69, 2011.
- [31] J. Li, R. Xia, W. Qi, X. Zhou, J. Cheng, Y. Chen, G. Hou, Y. Ding, Y. Li, Y. Zhao and X. Zhang, "Encapsulation of perovskite solar cells for enhanced stability: Structures, materials and characterization," *Journal of Power Sources*, vol. 485, p. 229313, 2021.
- [32] F. Corsini and G. Griffini, "Recent progress in encapsulation strategies to enhance the stability of organometal halide perovskite solar cells," *Journal of Physics: Energy*, vol. 2, p. 031002, 2020.
- [33] L. Shi, T. L. Young, J. Kim, Y. Sheng, L. Wang, C. Y, Z. Feng, M. J. Keevers, X. Hao, P. J. Verlinden, M. A. Green and A. W. Y. Ho-Baillie, "Accelerated lifetime testing of organic-inorganic perovskite solar cells encapsulated by polyisobutylene," *ACS Applied Material Interfaces*, vol. 9, no. 30, pp. 25073-25081, 2017.
- [34] C. A. Aranda, L. Calio and M. Salado, "Toward commercialization of stable devices: An overview on encapsulation of hybrid organic-inorganic perovskite solar cells," *Crystals*, vol. 11, no. 519, 2021.
- [35] Q. Dong, F. Liu, M. K. Wong, H. W. Tam, A. B. Djurisic, A. Ng, C. Surya, W. K. Chan and A. M. C. Ng, "Encapsulation of perovskite solar cells for high humidity conditions," *ChemSusChem*, vol. 9, pp. 2597-2603, 2016.
- [36] S. Emami, J. Martins, D. Ivanou and A. Mendes, "Advanced hermetic encapsulation of perovskite solar cells: the route to commercialization," *Journal of Materials Chemistry A*, vol. 8, pp. 2654-2662, 2020.

- [37] S. Castro-Hermosa, G. Lucarelli, M. Top, M. Hafland, J. Fahlteich and T. M. Brown, "Perovskite photovoltaics on roll-to-roll coated ultra-thin glass as flexible high-efficiency indoor power generators," *Cell Reports Physical Science*, vol. 1, no. 5, p. 100045, 2020.
- [38] Z. Liu, B. Sun, T. Shi, Z. Tang and G. Liao, "Enhanced photovoltaic performance and stability of carbon counter electrode based perovskite solar cells encapsulated by PDMS," *Journal of Materials Chemistry A*, vol. 4, pp. 10700-10709, 2016.
- [39] B. McKenna, J. R. Troughton, T. M. Watson and R. C. Evans, "Enhancing the stability of organolead halide perovskite films through polymer encapsulation," *RSC Advances*, vol. 7, pp. 32942-32951, 2017.
- [40] F. Bella, G. Griffini, J.-P. Correa-Baena, G. Saracco, M. Gratzel, A. Hagfeldt, S. Turri and C. Gerbaldi, "Improving efficiency and stability of perovskite solar cells with photocurable fluoropolymers," *Science*, vol. 354, no. 6309, pp. 203-206, 2016.
- [41] H.-H. Fang, J. Yang, S. Tao, S. Adjokatse, M. E. Kamminga, J. Ye, G. R. Blake, J. Even and M. A. Loi, "Unravelling light-induced degradation of layered perovskite crystals and design of efficient encapsulation for improved photostability," *Advanced Functional Materials*, vol. 28, 2018.
- [42] G. S. Han, J. S. Yoo, F. Yu, M. L. Duff, B. K. Kang and J.-K. Lee, "Highly stable perovskite solar cells in humid and hot environments," *Journal of Materials Chemistry A*, vol. 5, pp. 14733-14740, 2017.
- [43] J. H. Jang, B.-J. Kim, J.-H. Kim, E. Han, E. Y. Choi, C. H. Ji, K.-T. Kim, J. Kim and N. Park, "A novel approach for the development of moisture encapsulation poly(vinyl alcohol-co-ethylene) for perovskite solar cells," *ACS Omega*, vol. 4, pp. 9211-9218, 2019.

- [44] C.-Y. Chang, K.-T. Lee, W.-K. Huang, H.-Y. Siao and Y.-C. Chang, "High-performance, air-stable, low-temperature processed semitransparent perovskite solar cells enabled by atomic layer deposition," *Chemistry of Materials*, vol. 27, pp. 5122-5130, 2015.
- [45] G. Nisato, H. Klumbies, J. Fahlteich, L. Muller-Meskamp, P. van de Weijer, P. Bouten, C. Boeffel, D. Leunberger, W. Graehlert, S. Edge, S. Cros, P. Brewer, E. Kucukpinar and D. Girolamo, "Experimental comparison of high-performance water vapor permeation measurement methods," *Organic Electronics*, vol. 15, pp. 3746-3755, 2014.
- [46] M. Kim, T.-W. Kang, S. H. Kim, E. H. Jung, H. H. Park, J. Seo and S.-J. Lee, "Antireflective self-cleaning and protective film by continuous sputtering of a plasma polymer on inorganic multilayer for perovskite solar cells application," *Solar Energy Materials and Solar Cells*, vol. 191, pp. 55-61, 2019.
- [47] E. Y. Choi, J. Kim, S. Lim, E. Han, A. W. Y. Ho-Baillie and N. Park, "Enhancing stability for organic-inorganic perovskite solar cells by atomic layer deposited Al₂O₃ encapsulation," *Solar Energy Materials and Solar Cells*, vol. 188, pp. 37-45, 2018.
- [48] F. J. Ramos, T. Maindron, S. Bechu, A. Rebai, M. Fregnaux, M. Bouttemy, J. Rousset, P. Schulz and N. Schneider, "Versatile perovskite solar cell encapsulation by low-temperature ALD-Al₂O₃ with long-term stability improvement," *Sustainable Energy Fuels*, vol. 2, pp. 2468-2479, 2018.
- [49] Y. Lee, N. J. Jeon, B. J. Kim, H. Shim, T.-Y. Yang, S. Seok, J. Seo and S. G. Im, "A low-temperature thin-film encapsulation for enhanced stability of a highly efficient perovskite solar cell," *Advanced Energy Materials*, vol. 8, p. 1701928, 2018.

- [50] Z. Liu, L. Qiu, L. K. Ono, S. He, H. Zhanhao, M. Jiang, G. Tong, Z. Wu, Y. Jiang, D.-Y. Son, Y. Dang, S. Kazaoui and Y. Qi, "A holistic approach to interface stabilization for efficient perovskite solar modules with over 2,000-hour operational stability," *Nature Energy*, vol. 5, pp. 596-604, 2020.
- [51] N. M. R. Fumani, F. A. Roghabadi, A. Maryam, S. M. Sadrameli, V. Ahmadi and F. Najafi, "Prolonged lifetime of perovskite solar cells using a moisture-blocked and temperature-controlled encapsulation system comprising a phase change material as a cooling agent," *ACS Omega*, vol. 5, no. 13, pp. 7106-7114, 2020.
- [52] G. Grancini, C. Roldan-Carmona, I. Zimmermann, E. Mosconi, X. Lee and D. Martineau, "One-year stable perovskite solar cells by 2D/3D interface engineering," *Nature Communications*, pp. 1-8, 2017.
- [53] S. Lee, H. Choi, S. Shin, P. J. G. Ham, H. Jung and H. Jeon, "Permeation barrier properties of an Al₂O₃/ZrO₂ Multilayer deposited by remote plasma atomic layer deposition," *Current Applied Physics*, vol. 14, no. 4, pp. 552-557, 2014.
- [54] D.-W. Choi, S.-J. Kim, K.-B. Chung and J.-S. Park, "A study of thin film encapsulation on polymer substrate using low temperature hybrid ZnO/Al₂O₃ layers atomic layer deposition," *Current Applied Physics*, vol. 12, pp. 19-23, 2012.
- [55] S.-U. Shin and A. O. Ryu, "Optical transmittance improvements of Al₂O₃/TiO₂ multilayer OLED encapsulation films processed by atomic layer deposition," *Journal of Electronic Materials*, vol. 50, pp. 2015-2020, 2021.
- [56] S.-J. Bao, C. M. Li, J.-F. Zang, X.-Q. Cui and J. Guo, "New nanostructured TiO₂ for direct electrochemistry and glucose sensor applications," *Advanced Functional Materials*, vol. 18, no. 4, pp. 591-599, 2008.
- [57] J. Xu, Q. Pan, Y. Shun and Z. Tian, "Grain size control and gas sensing properties of ZnO gas sensor," *Sensors and Actuators B: Chemical*, vol. 66, pp. 277-279, 2000.

- [58] R. Georgekutty, M. K. Seery and S. C. Pillai, "A highly efficient Ag-ZnO photocatalyst: synthesis, properties, and mechanism," *Journal of Physical Chemistry C*, vol. 112, no. 35, pp. 13563-13570, 2008.
- [59] O. Teruhisa, M. Takahiro and M. Michio, "Photocatalytic activity of S-doped TiO₂ photocatalyst under visible light," *Chemistry Letters*, vol. 32, no. 4, pp. 364-365, 2003.
- [60] J. T. Carneiro, T. J. Savenije, J. A. Moulijn and G. Mul, "How phase composition influences optoelectronic and photocatalytic properties of TiO₂," *Journal of Physical Chemistry C*, vol. 115, no. 5, pp. 2211-2217, 2011.
- [61] A. B. Djuricic, A. M. C. Ng and X. Y. Chen, "ZnO nanostructures for optoelectronics: material properties and device applications," *Progress in Quantum Electronics*, vol. 34, no. 4, pp. 191-259, 2010.
- [62] B. Hussain, A. Ebong and I. Ferguson, "Zinc oxide as an active n-Layer and antireflection coating for silicon based heterojunction solar cell," *Solar Energy Materials and Solar Cells*, vol. 139, pp. 95-100, 2015.
- [63] B. S. Richards, "Single-material TiO₂ double-layer antireflection coatings," *Solar Energy Materials and Solar Cells*, vol. 79, no. 3, pp. 369-390, 2003.
- [64] A. Welte, C. Waldauf, C. Brabec and P. Wellmann, "Application of optical absorbance for the investigation of electronic and structural properties of sol-gel processed TiO₂ films," *Thin Solid Films*, vol. 516, pp. 7256-7259, 2008.
- [65] G. P. Bharti and A. Khare, "Structural and linear and nonlinear optical properties of Zn_{1-x}Al_xO (0 < x < 0.10) thin films fabricated via pulsed laser deposition technique," *Optical Materials Express*, vol. 6, no. 6, pp. 2063-2080, 2016.

- [66] A. M. Alsaad, A. A. Ahmad, I. A. Qattan, Q. M. Al-Bataineh and Z. Albatineh, "Structural, optoelectrical, linear, and nonlinear optical characterizations of dip-synthesized undoped ZnO and group III elements (B, Al, Ga, and In)-doped ZnO thin films," *Crystals*, vol. 10, pp. 252-269, 2020.
- [67] A. Ishii, Y. Nakamura, I. Oikawa, A. Kamegawa and H. Takamura, "Low-temperature preparation of high-n TiO₂ thin films on glass by pulsed laser deposition," *Applied Surface Science*, vol. 347, pp. 528-534, 2015.
- [68] R. Hong, C. Deng, M. Jing, H. Lin, C. Tao and D. Zhang, "Oxygen flows-dependent photocatalytic performance in Ti³⁺ doped TiO₂ thin films," *Optical Materials*, vol. 95, p. 109224, 2019.
- [69] F. K. Shan, B. C. Shin, S. W. Jang and Y. S. Yu, "Substrate effects of ZnO thin films prepared by PLD technique," *Journal of the European Ceramic Society*, vol. 24, pp. 1015-1018, 2004.
- [70] F. K. Shan and Y. S. Yu, "Band gap energy of pure and Al-doped ZnO thin films," *Journal of the European Ceramic Society*, vol. 24, pp. 1869-1872, 2004.
- [71] Y. Liu, L. Zhao and J. Lian, "Al-doped ZnO films by pulsed laser deposition at room temperature," *Vacuum*, vol. 81, pp. 18-21, 2006.
- [72] L.-W. Lai and C.-T. Lee, "Investigation of optical and electrical properties of ZnO thin films," *Materials Chemistry and Physics*, vol. 110, pp. 393-396, 2008.
- [73] E. M. Bachari, G. Baud, B. A. S. Amor and M. Jacquet, "Structural and optical properties of sputtered ZnO films," *Thin Solid Films*, vol. 348, no. 1, pp. 165-172, 1999.

- [74] S.-M. Park, T. Tomemori, T. Ikegami and K. Ebihara, "The growth of transparent conductive Al-doped ZnO thin films at room temperature," *Advances in Nanomaterials and Processing*, vol. 124, pp. 211-215, 2007.
- [75] T. Hitosugi, A. Ueda, Y. Furubayashi, Y. Hirose, S. Konuma, T. Shimada and T. Hasegawa, "Fabrication of TiO₂-based transparent conducting oxide films on glass by pulsed laser deposition," *Japanese Journal of Applied Physics*, vol. 46, pp. 86-88, 2007.
- [76] S. Bose, R. Arokiyadoss, P. Bhargav, G. Ahmad, S. Mandal, A. K. Barua and S. Mukhopadhyay, "Modification of surface morphology of sputtered AZO films with the variation of the oxygen," *Materials Science in Semiconductor Processing*, vol. 79, pp. 135-143, 2018.
- [77] A. A. Camacho-Berrios, V. M. Pantojas and W. Otano, "Reactive sputtered ZnO thin films: influence of the O₂/Ar flow ratio on the oxygen vacancies and paramagnetic active sites," *Thin Solid Films*, vol. 692, p. 137641, 2019.
- [78] H. M. Yates, M. G. Nolan, D. W. Sheel and M. E. Pemble, "The role of nitrogen doping on the development of visible light-induced photocatalytic activity in thin TiO₂ films grown on glass by chemical vapour deposition," *Journal of Photochemistry and Photobiology A: Chemistry*, vol. 179, pp. 213-223, 2006.
- [79] S. Fay, U. Kroll, C. Bucher, E. Vallat-Sauvain and A. Shah, "Low pressure chemical vapour deposition of ZnO layers for thin-film solar cells: temperature-induced morphological changes," *Solar Energy Materials and Solar Cells*, vol. 86, no. 3, pp. 385-397, 2005.
- [80] D. C. Look and D. C. Reynolds, "Characterization of homoepitaxial p-type ZnO grown by molecular beam epitaxy," *Applied Physics Letters*, vol. 81, no. 10, pp. 1830-1832, 2002.

- [81] Y. Matsumoto, R. Takahashi, M. Murakami, T. Koida, X.-J. Fan, T. Hasegawa, T. Fukumura, M. Kawasaki, S.-Y. Koshihara and H. Koinuma, "Ferromagnetism in Co-doped TiO₂ rutile thin films grown by laser molecular beam epitaxy," *Japanese Journal of Applied Physics*, vol. 40, pp. 1204-1206, 2001.
- [82] U. G. Akpan and B. H. Hameed, "The advancements in sol-gel method of doped-TiO₂ photocatalysts," *Applied Catalysis A: General*, vol. 375, no. 1, pp. 1-11, 2010.
- [83] J. T. Cheung, "History and fundamentals of pulsed laser deposition," in *Pulsed Laser Deposition of Thin Films*, New York, John Wiley & Sons, 1994, pp. 1-22.
- [84] G. Shukla, P. K. Mishra and A. Khare, "Effect of annealing and O₂ pressure on structural and optical properties of pulsed laser deposited TiO₂ thin films," *Journal of Alloys and Compounds*, vol. 489, no. 1, pp. 246-251, 2010.
- [85] J.-L. Zhao, X.-M. Li, J.-M. Bian, W.-D. Yu and X.-D. Gao, "Structural, optical and electrical properties of ZnO films grown by pulsed laser deposition (PLD)," *Journal of Crystal Growth*, vol. 276, no. 3, pp. 507-512, 2005.
- [86] Y. Ju, L. Li, Z. Wu and Y. Jiang, "Effect of oxygen partial pressure on the optical property of amorphous titanium oxide thin films," *Energy Procedia*, vol. 12, pp. 450-455, 2011.
- [87] B. Gobaut, P. Orgiani, A. Sambri, E. di Gennaro, C. Aruta, F. Borgatti, V. Lollobrigida, D. Ceolin, J.-P. Rueff, R. Ciancio, C. Bigi, P. Das, J. Fujii, D. Krizmancic, P. Torelli, I. Vobornik, G. Rossi, F. Granozio, U. di Uccio and G. Panaccione, "Role of oxygen deposition pressure in the formation of Ti defect states in TiO₂(001) anatase thin films," *ACS Applied Materials & Interfaces*, vol. 9, pp. 23099-23106, 2017.
- [88] S. Kazan, "Growth and characterization of TiO₂ thin films by PLD technique," *Journal of the Institute of Science and Technology*, vol. 11, no. 1, pp. 221-226, 2021.

- [89] E. Hasabeldaim, O. M. Ntwaeaborwa, R. E. Kroon, D. E. Motaung, E. Coetsee and H. C. Swart, "Effect of PLD growth atmosphere on the physical properties of ZnO:Zn thin films," *Optical Materials*, vol. 74, pp. 76-85, 2017.
- [90] X. Li, Y. Wang, W. Liu, G. Jiang and C. Zhu, "Study of oxygen vacancies' influence of the lattice parameter in ZnO thin films," *Materials Letters*, vol. 85, pp. 25-28, 2012.
- [91] R. Kek, K.-C. Tan, C. H. Nee, S. L. Yap, S. F. Koh, A. Arof, T. Y. Tou and S. S. Yap, "Effects of pressure and substrate temperature on the growth of Al-doped ZnO films by pulsed laser deposition," *Materials Research Express*, vol. 7, p. 016414, 2020.
- [92] P. G. Devi and A. S. Velu, "Synthesis, structural and optical properties of pure ZnO and Co-doped ZnO nanoparticles prepared by the Co-precipitation method," *Journal of Theoretical and Applied Physics*, vol. 10, pp. 233-240, 2016.
- [93] D. B. Geohegan, "Diagnostics and Characteristics of Pulsed Laser Deposition Laser Plasmas," in *Pulsed Laser Deposition of Thin Films*, New York, John Wiley & Sons, 1994, pp. 115-165.
- [94] A. S. Kuzanyan and A. A. Kuzanyan, "Pulsed Laser Deposition of Large-Area Thin Films and Coatings," in *Applications of Laser Ablation*, IntechOpen, 2016.
- [95] K. L. Seanger, "Angular Distribution of Ablated Material," in *Pulsed Laser Deposition of Thin Films*, New York, John Wiley & Sons, Inc., 1994, pp. 199-227.
- [96] A. K. Jena, A. Kulkarni and T. Miyasaka, "Halide perovskite photovoltaics: background, status, and future," *Chemical Reviews*, vol. 119, pp. 3036-3103, 2019.
- [97] Q. Lin, A. Armin, R. C. R. Nagiri, P. L. Burn and P. Meredith, "Electro-optics of perovskite solar cells," *Nature Photonics*, vol. 9, pp. 106-112, 2015.

- [98] D. Mergel, D. Buschendorf, S. Eggert, R. Grammes and B. Samset, "Density and refractive index of TiO₂ films prepared by reactive evaporation," *Thin Solid Films*, vol. 371, pp. 218-224, 2000.
- [99] G. R. Fowles, *Introduction to Modern Optics*, 2nd Ed., New York: Courier Corporation, 1989.
- [100] B. Bharti, S. Kumar, H.-N. Lee and R. Kumar, "Formation of oxygen vacancies and Ti³⁺ state in TiO₂ thin film and enhanced optical properties by air plasma treatment," *Scientific Reports*, vol. 6, p. 32355, 2016.
- [101] R. V. Nair, V. S. Gummaluir, M. V. Matham and C. Vijayan, "A review on optical bandgap engineering in TiO₂ nanostructures via doping and intrinsic vacancy modulation towards visible light applications," *Journal of Physics D: Applied Physics*, vol. 55, p. 313003, 2022.
- [102] C. Dette, M. A. Perez-Osorio, C. S. Kley, C. E. Patrick, P. Jacobson, F. Giustino, S. J. Jung and K. Kern, "TiO₂ anatase with a bandgap in the visible region," *Nano Letters*, vol. 14, no. 11, pp. 6533-6538, 2014.
- [103] M. Emam-Ismail, E. R. Shaaban and M. El-Hagary, "A new method for calculating the refractive index of semiconductor thin films retrieved from their transmission spectra," *Journal of Alloys and Compounds*, vol. 663, pp. 20-29, 2016.
- [104] J. Wang, Z. Wang, B. Huang, Y. Ma, Y. Liu, X. Qin, X. Zhang and Y. Dai, "Oxygen vacancy induced band-gap narrowing and enhanced visible light photocatalytic activity of ZnO," *ACS Applied Material Interfaces*, vol. 4, no. 8, pp. 4024-4030, 2012.
- [105] H. Liu, F. Zeng, Y. Lin, G. Wang and F. Pan, "Correlation of oxygen vacancy variations to band gap changes in epitaxial ZnO thin films," *Applied Physics Letters*, vol. 102, p. 181908, 2013.

- [106] S. Lany and A. Zunger, "Dopability, intrinsic conductivity, and nonstoichiometry of transparent conducting oxides," *Physical Review Letters*, vol. 98, p. 045501, 2007.
- [107] Y. Li, R. Yao, H. Wang, X. Wu, J. Wu, X. Wu and W. Qin, "Enhanced performance in Al-doped ZnO based transparent flexible transparent thin-film transistors to oxygen vacancy in ZnO film with Zn-Al-O interfaces fabricated by atomic layer deposition," *ACS Applied Material Interfaces*, vol. 9, no. 13, pp. 11711-11720, 2017.
- [108] M. Wang, K. E. Lee, S. H. Hahn, E. J. Kim, S. Kim, J. S. Ching, E. W. Shin and C. Park, "Optical and photoluminescent properties of sol-gel Al-doped ZnO thin films," *Materials Letters*, vol. 61, pp. 1118-1121, 2007.
- [109] E. Burstein, "Anomalous optical absorption limit in InSb," *Physical Reviews*, vol. 93, pp. 632-633, 1954.
- [110] T. S. Moss, "The interpretation of the properties of indium antimonide," *Proceedings of the Physical Society Section B*, vol. 67, pp. 775-782, 1954.
- [111] K. G. Saw, N. M. Aznan, F. K. Yam, S. S. Ng and S. Y. Pung, "New insights on the Burstein-Moss shift and band gap narrowing in indium-doped zinc oxide thin films," *PLoS One*, vol. 10, no. 10, 2015.
- [112] X. Q. Gu, L. P. Zhu, L. Cao, Z. Z. Ye, H. P. He and P. K. Chu, "Optical and electrical properties of ZnO:Al thin films synthesized by low-pressure pulsed laser deposition," *Materials Science in Semiconductor Processing*, vol. 14, pp. 48-51, 2011.
- [113] J.-Y. Lin, K.-D. Zhong and P.-T. Lee, "Plasmonic behaviors of metallic AZO thin film and AZO nanodisk array," *Optics Express*, vol. 24, no. 5, pp. 5125-5135, 2016.

- [114] "Reference Air Mass 1.5 Spectra," NREL, [Online]. Available: <https://www.nrel.gov/grid/solar-resource/spectra-am1.5.html>. [Accessed 11 March 2022].
- [115] J. Coulter and D. Birnie, "Assessing tauc plot slope quantification: ZnO thin films as a model system," *Physica Status Solidi B*, vol. 255, p. 1700393, 2018.
- [116] S. J. Pearton, D. P. Norton, K. Ip, Y. W. Heo and T. Steiner, "Recent progress in processing and properties of ZnO," *Superlattices and Microstructures*, vol. 34, pp. 3-32, 2003.
- [117] J. H. Park, J. M. Shin, S.-Y. Cha, J. W. Park, S.-Y. Jeong, H. K. Pak and C.-R. Cho, "Deposition-temperature effects on AZO thin films prepared by RF magnetron sputtering and their physical properties," *Journal of Korean Physical Society*, vol. 49, pp. 584-588, 2006.
- [118] S. Pat, R. Mohammadigharehbagh, S. Ozen, V. Senay, H. Yudar and S. Korkmaz, "The Al doping effect on the surface, optical, electrical and nanomechanical properties of the ZnO and AZO thin films prepared by RF sputtering technique," *Vacuum*, vol. 141, pp. 210-215, 2017.
- [119] J. M. Lackner, W. Waldhauser, R. Ebner, B. Major and T. Schoberl, "Pulsed laser deposition of titanium oxide coatings at room temperature - structural, mechanical and tribological properties," *Surface and Coatings Technology*, vol. 180, pp. 585-590, 2004.
- [120] H. J. Son, K. A. Jeon, C. E. Kim, J. H. Kim, K. H. Yoo and S. Y. Lee, "Synthesis of ZnO nanowires by pulsed laser deposition in furnace," *Applied Surface Science*, vol. 253, no. 19, pp. 7848-7850, 2007.
- [121] H. S. Supriyono, Y. K. Krisnandi and J. Gunluardi, "Preparation and characterization of transparent conductive SnO₂-F thin film deposited by spray

- pyrolysis: relationship between loading level and some physical properties," *Procedia Environmental Sciences*, vol. 28, pp. 242-251, 2015.
- [122] S. M. Mohammed and K. H. Amani, "Study of the optical and structural properties of PbI₂ thin films prepared by spin coating technique at room temperature," *Journal of Physics: Conference Series*, vol. 1795, p. 012019, 2021.
- [123] G. Li, Z. Jiang, W. Wang, Z. Chu, Y. Zhang and C. Wang, "Electrospun PAN/MAPbI₃ composite fibers for flexible and broadband photodetectors," *Nanomaterials*, vol. 9, pp. 50-61, 2019.
- [124] Z. R. Khan, A. S. Alshammari, M. Mohamed and M. Shkir, "Structural, vibrational and opto-nonlinear properties of spin coater derived PbI₂ films: Effect of solute concentrations," *Physica B: Physics of Condensed Matter*, vol. 654, p. 414270, 2022.
- [125] L. Gong, Z. Ye, J. Lu, L. Zhu, J. Huang, X. Gu and B. Zhao, "Highly transparent conductive and near-infrared reflective ZnO:Al thin films," *Vacuum*, vol. 84, pp. 947-952, 2010.
- [126] P. Prasan, N. Aunping, N. Chanlek, P. Kumlangwan, M. Towannang, P. Klangtakai, P. Srepusharawoot, A. Thongnum, P. Kumnorkaew, W. Jarernboon, S. Pimanpang and V. Amornkitbamrung, "Influence of SCN⁻ moiety on CH₃NH₃PbI₃ perovskite film properties and the performance of carbon-based hole-transport-layer-free perovskite solar cells," *Journal of Materials Science: Materials in Electronics*, vol. 33, pp. 1598-1603, 2022.
- [127] Y. Jiang, E. J. Juarez-Perez, Q. Ge, S. Wang, M. R. Leyden, L. K. Ono, S. R. Raga, J. Hu and Y. Qi, "Post-annealing of MAPbI₃ perovskite films with methylamine for efficient perovskite solar cells," *Materials Horizon*, vol. 3, pp. 548-555, 2016.
- [128] Z. Song, S. C. Watthage, A. B. Phillips, B. L. Tompkins, R. J. Ellingson and M. J. Heben, "Impact of processing temperature and composition on the formation of

methylammonium lead iodide perovskites," *Chemistry of Materials*, vol. 27, no. 13, pp. 4612-4619, 2015.

- [129] E. Hoke, D. Slotcavage, E. Dohner, A. Bowring, H. I. Karunadasa and M. D. McGehee, "Reversible photo-induced trap formation in mixed-halide hybrid perovskites for photovoltaics," *Chemical Science*, vol. 6, pp. 613-617, 2015.

Appendices

Appendix A: Integration Error Sample Calculations

i. Numerical Integration Error

The trapezoidal method was used to integrate the ASTM G-173 solar irradiation spectrum, i.e.,

For $f(\lambda) = \text{ASTM G173}(\lambda)$

$$\int_a^b f(\lambda) d\lambda \cong \frac{b-a}{2n} [f(\lambda_0) + 2f(\lambda_1) + 2f(\lambda_2) + \dots + 2f(\lambda_{n-1}) + f(\lambda_n)]$$

$$\text{UVB region: } \int_{260 \text{ nm}}^{315 \text{ nm}} f(\lambda) d\lambda \cong 0.68 \text{ W/m}^2$$

$$\text{UVA region: } \int_{315 \text{ nm}}^{400 \text{ nm}} f(\lambda) d\lambda \cong 45.42 \text{ W/m}^2$$

$$\text{Visible region: } \int_{400 \text{ nm}}^{750 \text{ nm}} f(\lambda) d\lambda \cong 489.88 \text{ W/m}^2$$

Using the trapezoidal method, the maximum integration error is defined as:

$$|E| \leq \frac{K(b-a)^3}{12n^2}$$

where b and a are the upper and lower bounds of the integration, n is the number of subintervals between $[a, b]$, and K is the maximum value of the second derivative of the function being integrated. Two sequences of the central difference method were used to differentiate the ASTM G-173 spectrum and the maximum function values in the UVB, UVA and visible light regions were identified. The maximum integration error was determined for each of these regions:

$$|E_{UVB}| \leq \frac{0.021578(315 - 280)^3}{12(68)^2} = 0.016673 \text{ W/m}^2$$

$$|E_{UVA}| \leq \frac{0.75666(400 - 315)^3}{12(170)^2} = 1.339919 \text{ W/m}^2$$

$$|E_{VIS}| \leq \frac{0.18884(750 - 400)^3}{12(350)^2} = 5.507833 \text{ W/m}^2$$

ii. Error on Irradiated Light that is Absorbed/Reflected and Transmitted

To determine the amount of irradiated light that is absorbed/reflected by the coating, the % absorption/reflection at each wavelength is evaluated from the transmittance spectra data (which is taken as the average across left, center and right locations on the sample):

$$A_{avg} = 100 - T_{avg}$$

$$A_{avg} = 100 - 89.98667$$

$$A_{avg} = 10.01333 \%$$

To evaluate the uncertainty (w), the A_{avg} are averaged across UVB, UVA and visible light regions, and the uncertainty is taken as the average sample standard deviation (σ) for each region:

$$(A_{avg})_i = \frac{\sum A_{avg}}{n}$$

$$(A_{avg})_{UVB} = 95.2129 \%$$

$$(A_{avg})_{UVA} = 78.6509 \%$$

$$(A_{avg})_{VIS} = 7.5312 \%$$

$$(w_{A_{avg}})_i = \frac{\sum \sigma_i}{n}$$

$$(w_{A_{avg}})_{UVB} = 0.286214 \%$$

$$(w_{A_{avg}})_{UVA} = 0.466521 \%$$

$$(w_{A_{avg}})_{VIS} = 0.885078 \%$$

The amount (W/m^2) of irradiated light that is absorbed/reflected is determined by multiplying A_{avg} by the integrated ASTM-G173 spectrum. Here, the A_{avg} used corresponds to the average absorption/reflection % across the interval $[\lambda_a, \lambda_b]$, which represents one step in the numerical integration. These steps are summed across the UVB, UVA and visible light regions to obtain the total absorption in each region:

$$(\text{amount absorbed light})_i = \sum A_{avg} \int_{\lambda_a}^{\lambda_b} (ASTM - G173) d\lambda$$

$$(\text{amount of absorbed light})_{UVB} = 0.61213 W/m^2$$

$$(\text{amount of absorbed light})_{UVA} = 33.5167 W/m^2$$

$$(\text{amount of absorbed light})_{VIS} = 37.85 W/m^2$$

The error on the amount of absorbed/reflected light is therefore given by:

$$(w_A)_i = \left[\left(\frac{\text{amount absorbed light}}{\text{amount irradiated light}} * |E_i| \right)^2 + \left(\frac{\text{amount absorbed light}}{(A_{avg})_i} * (w_{A_{avg}})_i \right)^2 \right]^{1/2}$$

$$(w_A)_{UVB} = \left[\left(\frac{0.61213 \frac{W}{m^2}}{0.68 \frac{W}{m^2}} * 0.016673 \frac{W}{m^2} \right)^2 + \left(\frac{0.61213 \frac{W}{m^2}}{95.2125 \%} * 0.286214 \% \right)^2 \right]^{1/2}$$

$$(w_A)_{UVB} = 0.01512 W/m^2$$

$$(w_A)_{UVA} = 1.00855 W/m^2$$

$$(w_A)_{VIS} = 4.46415 W/m^2$$

The amount of light that is transmitted by the coated is determined by:

$$\begin{aligned} & (\text{amount of transmitted light})_i \\ & = (\text{amount irradiated light})_i - (\text{amount absorbed light})_i \end{aligned}$$

$$(\text{amount of transmitted light})_{UVB} = 0.68 \text{ W/m}^2 - 0.61213 \text{ W/m}^2$$

$$(\text{amount of transmitted light})_{UVB} = 0.0702 \text{ W/m}^2$$

$$(\text{amount of transmitted light})_{UVA} = 11.9033 \text{ W/m}^2$$

$$(\text{amount of transmitted light})_{VIS} = 452.067 \text{ W/m}^2$$

The error on the amount of transmitted light is therefore:

$$(w_T)_i = [|E_i|^2 + (w_A)_i^2]^{1/2}$$

$$(w_T)_{UVB} = \left[\left(0.016673 \frac{\text{W}}{\text{m}^2} \right)^2 + \left(0.01512 \frac{\text{W}}{\text{m}^2} \right)^2 \right]^{1/2}$$

$$(w_T)_{UVB} = 0.02251 \text{ W/m}^2$$

$$(w_T)_{UVA} = 1.67707 \text{ W/m}^2$$

$$(w_T)_{VIS} = 7.08977 \text{ W/m}^2$$

iii. Error on the Percentage of Irradiated Light that is Absorbed/Reflected

To obtain the percentage of irradiated light that is absorbed/reflected, the amount of irradiated light that is absorbed/reflected is divided by the amount of irradiated light. Note that this is different than $(A_{avg})_i$.

$$(\% \text{ absorbed})_i = \frac{(\text{amount absorbed light})_i}{(\text{amount irradiated light})_i} \times 100\%$$

$$(\% \text{ absorbed})_{UVB} = \frac{0.61213 \text{ W/m}^2}{0.68 \text{ W/m}^2} \times 100\%$$

$$(\% \text{ absorbed})_{UVB} = 89.71 \%$$

$$(\% \text{ absorbed})_{UVA} = 73.79 \%$$

$$(\% \text{ absorbed})_{VIS} = 7.72 \%$$

The error on the percentage of absorbed/reflected light is therefore:

$$(w_P)_i = \left[\left(\frac{(\% \text{ absorbed})_i}{100 (\text{amount absorbed light})_i} (w_A)_i \right)^2 + \left(\frac{-(\% \text{ absorbed})_i}{100 (\text{amount irradiated light})_i} |E_i| \right)^2 \right]^{1/2} \times 100 \%$$

$$(w_P)_{UVB} = \left[\left(\frac{89.71 \%}{100 \times 0.61213 \text{ W/m}^2} 0.01512 \text{ W/m}^2 \right)^2 + \left(\frac{-89.71 \%}{100 \times 0.68 \text{ W/m}^2} 0.016673 \text{ W/m}^2 \right)^2 \right]^{1/2} \times 100 \%$$

$$(w_P)_{UVB} = 3.1224 \%$$

$$(w_P)_{UVA} = 3.1096 \%$$

$$(w_P)_{VIS} = 0.9155 \%$$

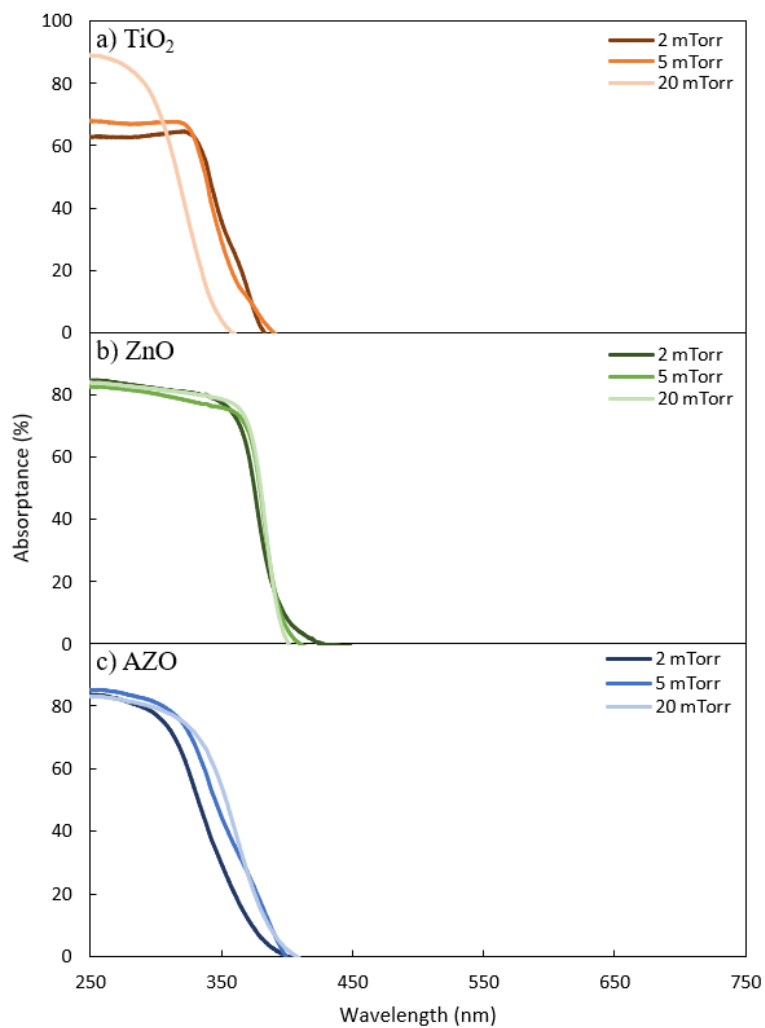
Appendix B: Supplemental Material

Figure 41: UV-Visible light absorbance spectra of a) TiO₂, b) ZnO, and c) AZO coatings deposited by PLD at oxygen partial pressures of 0, 2 and 20 mTorr.

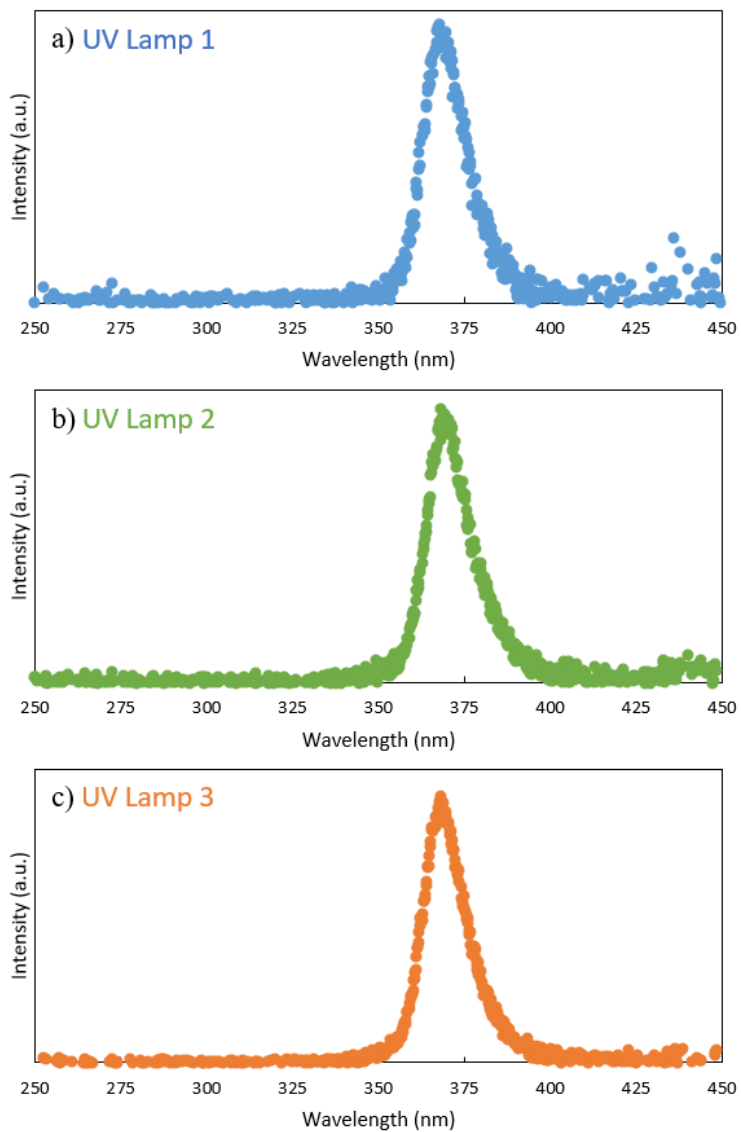


Figure 42: Emission spectra of UV lamps a) 1, b) 2, and c) 3 used for perovskite photodegradation.

Curriculum Vitae

Name: Katherine Lochhead

**Post-secondary
Education and
Degrees:** University of Ottawa
Ottawa, Ontario, Canada
2016-2020 B.A.Sc.

The University of Western Ontario
London, Ontario, Canada
2021-2023 (in progress) M.E.Sc.

**Honours and
Awards:** Natural Sciences and Engineering Research Council (NSERC)
Canada Graduate Scholarship – Master’s program
2022-2023

Publications:

Lochhead, K., Johlin, E., & Yang, D. (2022). Encapsulation of Perovskite Solar Cells with Thin Barrier Films. In (Ed.), *Thin Film Deposition - Fundamentals, Processes, and Applications*. IntechOpen. <https://doi.org/10.5772/intechopen.107189>